DAVID ANDREW BARKHUIZEN
BSc (Chemistry, Applied Maths) & BSc.Hons (Chemistry) - University of Natal

Preparation and Water-Gas Shift Performance of Zinc Oxide Supported Dispersed Gold Catalysts

A thesis submitted in the
Chemical Engineering Department
of the
University of Cape Town
in partial fulfilment of the requirements of the degree of
Master of Science in Applied Science

2007

Declaration of Free Licence

For the purposes of this declaration, *'the University'* shall hereby refer to the University of Cape Town, South Africa, and *'the thesis'* shall refer to the taught masters thesis *'Preparation and Activity of Gold Catalysts for Water-Gas Shift Conversion'* authored by David Andrew Barkhuizen.

I hereby

(a) grant *the University* free licence to reproduce *the thesis* in whole or in part, for the purpose of research;

(b) declare that:

(i) *the thesis* is my own unaided work, both in conception and execution, and that apart from the normal guidance of my supervisor, I have received no assistance apart from that stated below;

(ii) except as stated below, neither the substance nor any part of *the thesis* has been submitted in the past, or is being, or is to be submitted for a degree in *the University* or any other university;

(iii) I am now presenting *the thesis* for examination for the degree of Master of Applied Science by half dissertation.

Signed by candidate

David Andrew Barkhuizen
2007 – 01 - 26

Synopsis

Two deposition-precipitation style methods of preparing zinc oxide supported dispersed gold materials for use as water-gas shift catalysts were examined, with some of the better formulated materials being tested for catalytic activity, and compared to World Gold Council Au/TiO_2 reference material and a commercial copper-based WGS catalyst (Cu/ZnO/Al_2O_3 – C 18-7 from Süd-Chemie).

Materials Synthesis

The classical deposition-precipitation synthesis from the group of Haruta (Tsubota *et al.*, 1995) - where the support is added to a pH adjusted solution of $HAuCl_4$ and the system aged at constant pH and temperature - was examined, using ZnO as the support.

Gold uptake by the support was confirmed to decrease with ageing pH, tending to zero as the IEPS of ZnO (~ 9) is approached. Such behaviour is both qualitatively and quantitatively consistent with theory, which proposes that the magnitude and polarity of the charge on the support surface will determine the effective carrying capacity of that surface for an (an)ionic solution phase gold species.

Decreasing post-calcination (120°C) gold crystallite size with increasing ageing pH [as reported by Haruta (1997)] was also observed (figure 11.2) - but it is not clear whether this resulted from pH dependent crystallization dynamics, from crystallite size being simply determined by the amount of deposited gold (which clearly decreases with increasing pH), or from chloride induced sintering during heat treatment (with chloride uptake by the support decreasing with increasing pH [Kung *et al.*, 2003)). Nevertheless, gold deposition at pH 8 produced highly dispersed gold crystallites around 3.5 nm in diameter.

It emerged that an inherent trade-off exists with this, the classical deposition-precipitation method, in that acidic ageing pH promotes a high degree of gold uptake by the support, but produces large gold crystallites, and vice versa.

To overcome this, a modified method - where $HAuCl_4$ and the base (ammonium carbonate) were simultaneously added dropwise to a slurry of the support, maintaining a constant pH of 8 (Fu *et al.*, 2003b) - was investigated. This method was attractive because it is claimed to simultaneously achieve total gold uptake and post-calcination Au crystallite size in the range 5 – 6 nm. Since it was not clear from the published description whether a constant pH was maintained across the ageing period (practiced here as MDP1), or if the pH was rather allowed to drift (practiced here as MDP2), both alternatives were investigated.

When a constant pH was maintained across the ageing period (MDP1), gold uptake by the support was found to reach a maximum (of ~ 60 %) when operating at a pH of ~ 8. The degree of gold uptake was found to be independent of both gold loading and support surface area.

Furthermore, the degree of gold uptake achieved using this variation was increased to unity by allowing the pH to drift during the ageing period (after being initially held constant at 8 during $HAuCl_4$ addition) [= MDP2], instead of being maintained at a constant value via addition of nitric acid (as is done in MDP1). In terms of the size of the gold crystallites produced, after calcination in air at 400°C, a mean diameter of 3.8 ± 1.5 nm was observed for a sample 1.9 wt % in Au, increasing slightly with increasing gold loading [to 4.6 ± 1.7 nm by 5.1 wt % Au].

Materials Activity

Under the experimental conditions used, no activity was observed for a low (3.6 $m^2.g^{-1}$) surface area ZnO at temperatures up to 400°C, while measurable (2% conversion) activity was observed over the novel higher surface (~ 40 $m^2.g^{-1}$) area material synthesized.

In both materials promotion of WGS activity to lower temperatures as a result of the deposition (MDP2) of gold was clearly observed. However, (for Au/ZnO materials produced from the higher surface area novel ZnO) intrinsic activity (CO conversion normalised with respect to total moles of gold) was found to decrease with increasing gold content, and in fact when WGS activity was quantified in this way, at 400°C (when conversion is below ~ 30 %) the activity was found to decrease linearly with increasing gold content.

Although the mean gold crystallite size was determined to increase slightly with gold loading, leading to a slight reduction in gold dispersion, normalisation of reaction rate with respect to approximate exposed gold surface area revealed that the decrease in rate with increasing gold loading could not be explained simply in terms of decreasing dispersion.

Furthermore, Au/ZnO produced via the deposition of $Au(OH)_3$ on zinc hydroxycarbonate, followed by heat treatment of the composite to simultaneously reduce the Au(III) and decompose the zinc hydroxycarbonate to zinc oxide, produced material with a far higher rate of CO conversion per mole of gold than any of the materials produced from $Au(OH)_3/ZnO$ - this despite having a significantly greater mean gold crystallite size, as reflected in the rate of CO conversion per gold surface area.

Finally, the most active Au/ZnO material synthesized in this work [Au/ZnO from $Au(OH)_3/Zn_5(OH)_6(CO_3)_2$], the Au/TiO_2 reference from the World Gold Council and the commercial copper-based $Cu/ZnO/Al_2O_3$ WGS catalyst were compared.

On a per total catalyst mass basis, the commercial copper-based WGS catalyst was clearly the most active material, with 1 g of material achieving 50 % CO conversion at

161°C, while the same mass of the Au/TiO_2 and the novel Au/ZnO only achieved the same level of conversion at temperatures of 259°C and 397°C respectively.

However, when the data is evaluated on a per mol of group IB metal (ie Au or Cu) basis, the gold-based materials appear far more active.

Acknowledgements

Foreign Material

CO conversion data for $Cu/ZnO/Al_2O_3$ and Au/TiO_2 was collected by a collaborator, Yatish Daya, and is hereby acknowledged as such.

Support and Assistance

The author wishes to gratefully acknowledge the following support:

Academic
Prof. Jack CQ Fletcher
Mr Walter Böhringer
Mr Alexander Popp
Mr Stephen Roberts
Prof. Eric van Steen
Dr Noko Phala

Technical
Dr Mohammed Jaffer
Mr Marc Wüst
Ms Stephanie la Grange
Ms Zulfa Afrika
Ms Helen Divey
Mr Peter Dobias
Mr Granville de la Cruz
Mr David Bramble

Financial
Mintek Pty Ltd (RSA) / Project AuTek
South African National Research Foundation (NRF)
Catalysis Research Unit, Chemical Engineering Department, University of Cape Town

Table of Contents

List of Figures

List of Tables

Glossary

ATR	auto-thermal reforming
BET	Brunauer-Emmett-Teller (-surface area)
BPR	back pressure regulator
CP	coprecipitation
DP	deposition-precipitation
eqn	equation
FCC	face centred cubic
FID	flame ionisation (GC) detector
GC	gas chromatograph
fig.	figure
HFC	hydrogen fuel cell
HTS	high temperature shift
LTS	low temperature shift
MO	metal oxide (M_xO_y)
PEM	polymer/proton electrolyte membrane
PGM	platinum group metal
PrOx	preferential oxidation
PVD	physical vapour deposition
RT	room temperature, 25°C
SA	(N_2-BET) surface area
sccm	abbreviates 'standard cubic centimetres per minute', refers to the gas volume at 0°C (273K), rather than at STP (25°C).
SiC	silicone carbide (Carborundum™)
S/G	(molar) steam to dry gas ratio in combined feed
SGHSV	standard gaseous hourly space velocity (volume of feed gas at STP per volume of catalyst per time unit)
STM	scanning tunnelling microscopy
STS	scanning tunnelling spectroscopy
STP	standard temperature (25°C) and pressure (1 atm = 1.101325×10^5 Pa)
TCD	thermal conductivity (GC) detector
TEM	transmission electron micrograph(y)
TOF	turn-over frequency
UGC	urea gellation co-precipitation
WGC	World Gold Council
WGS	water-gas shift
WGSR	water-gas shift reaction
WHSV	weight hourly space velocity (mass of feed gas per mass of catalyst per time unit)
wt	weight (mass)
XAFS	x-ray absorption fine structure
XPS	x-ray photo-electron spectroscopy
XRD	x-ray diffraction (spectroscopy)

Introduction

1

Metal oxide supported dispersed gold materials show much promise with regard to catalysing a number of gas phase reactions, notably the water gas shift reaction ($CO + H_2O \leftrightarrows CO_2 + H_2$) which may well be employed to clean up CO in hydrogen fuel processors for hydrogen fuel cells. This latter goal, however, requires the development of new and better catalysts, as those materials traditionally used to catalyse the reaction in an industrial context ($Cu/ZnO/Al_2O_3$ and Fe_3O_4/Cr_2O_3) are unsuitable for a number of reasons.

The work presented in this volume can be divided into two sections: the first concerned with the preparation and physical characterisation of novel Au/ZnO materials, and the second with an evaluation of the catalytic performance of selected synthesised material and their comparison with that of benchmark materials [a current industrial $Cu/ZnO/Al_2O_3$ low-temperature shift catalyst (C18-7, Süd-Chemie) and a World Gold Council reference catalyst Au/TiO_2].

Development of Au/ZnO as a water gas shift catalyst involves assessing to some extent the variation of catalyst structure and activity with preparation conditions and methodology.

The choice of zinc oxide as an appropriate support is based upon its current use in the commercial Cu/ZnO based low temperature shift catalysts as well as the reported activity of Au/ZnO for methanol synthesis and the known similarity between commercial Cu/ZnO based WGS and MeOH catalysts.

Industrial Setting

2

2.1 Traditional WGS

The WGS reaction (eqn 2.1) is the exothermic (ΔH°_{298K} = - 41.2 kJ.mol^{-1}) complete oxidation of CO to CO_2 by water under conditions where all reactants and products are gaseous in the bulk state (i.e. above the dew-point of water) and is not associated with any appreciable overall change in volume.

$$CO + H_2O \leftrightarrows CO_2 + H_2 \qquad \text{(eqn 2.1)}$$

Although at equilibrium the forward reaction is favoured by a decrease in temperature, when the reaction is catalysed at a solid surface any decrease in temperature will typically reduce the overall reaction rate and a successful process implementation must find a profitable compromise between these two factors.

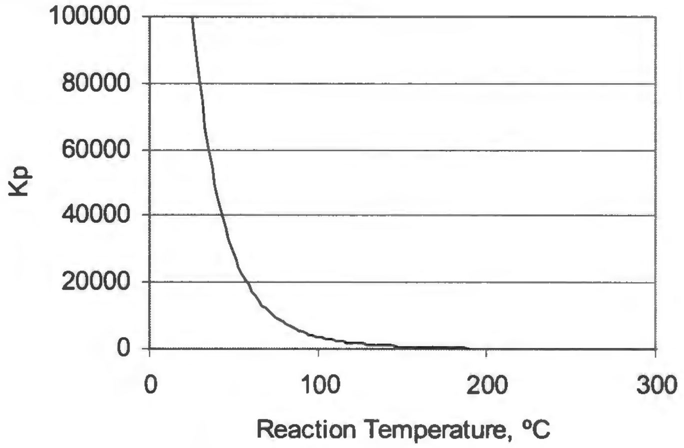

Figure 2.1: The thermodynamic equilibrium constant (Kp) for the water gas shift reaction ($CO + H_2O \leftrightarrows CO_2 + H_2$) as a function of reaction temperature.

The WGSR is traditionally used to adjust the composition of synthesis gas (H_2, CO, CO_2, N_2) produced via the steam reforming of hydrocarbons, e.g natural gas and coal. In ammonia synthesis, it is employed to circumvent catalyst poisoning by CO while in hydrogen production it is used to boost overall hydrogen yield and provide a route to CO_x removal.

Steam reforming entails the reaction of steam with the hydrocarbon, to yield CO and H_2 (eqn 2.2), and this takes place in conjunction with the water-gas shift reaction (eqn 2.3), which yields CO_2 and further H_2. Subsequent reactions (eqns 2.4, 2.6) and side-reactions (eqn 2.4) also take place.

Table 2.1: Steam reforming reactions given in the case of methane (Moulijn *et al.*, 2001)

Reaction			ΔH°_{298} (kJ.mol^{-1})	Equation
$CH_4 + H_2O$	$\leftrightarrows$	$CO + 3H_2$	206	2.2
$CO + H_2O$	$\leftrightarrows$	$CO_2 + H_2$	- 41	2.3
$CH_4 + CO_2$	$\leftrightarrows$	$2CO + 2H_2$	247	2.4
CH_4	$\leftrightarrows$	$C + 2H_2$	75	2.5
$2CO$	$\leftrightarrows$	$C + CO_2$	- 173	2.6

Although the WGS reaction (eqn 2.3) is exothermic, the primary steam reforming reaction (eqn 2.2) is highly endothermic, and thus steam reforming in an anoxic environment is overall an endothermic process, requiring the addition of heat from an outside source (so called allothermal reforming). Often in practice, rather than supplying heat from an external source, steam reforming is carried out in the presence of oxygen, where partial oxidation of the hydrocarbon (eqn 2.7), an exothermic process, can supply the requisite energy (autothermal reforming, ATR). In this case side reactions such as complete oxidation (eqn 2.8) and oxidation of CO (eqn 2.9) and H_2 (eqn 2.10) can also occur.

Table 2.2: Additional (exothermic) oxidation reactions applicable in the case of autothermal reforming (Moulijn *et al.*, 2001)

Reaction			ΔH°_{298} (kJ.mol^{-1})	Equation
$CH_4 + ½O_2$	→	$CO + 2H_2$	- 36	2.7
$CH_4 + 2O_2$	→	$CO_2 + 2H_2O$	- 803	2.8
$CO + ½O$	→	CO_2	- 284	2.9
$H_2 + ½O$	→	H_2O	- 242	2.10

Temperatures of up to 800°C and pressures of up to 35 MPa are typical of industrial natural gas reformers employing an Al_2O_3 supported metallic nickel catalyst. Notable general characteristics of the reformer product are a high level of hydrogen, and appreciable levels of carbon monoxide (CO).

Industrial implementation of the WGSR must contend with the trade-off resulting from an increase in temperature bringing both a desirable increase in reaction rate and an undesirable decrease in maximum achievable (equilibrium) conversion. This problem is generally dealt with by performing the reaction in two distinct stages, using fixed-bed adiabatic reactors with inter-bed cooling. The first, high temperature shift (HTS), stage typically operates at 320 – 400°C using a Fe_3O_4 based catalyst while the second, low temperature shift (LTS), stage operates in the 200 – 250°C range and uses a more active Cu/ZnO based material. Each stage generally achieves close to equilibrium conversion: CO levels in the exit stream typically in the range at 2 – 4 % in the HTS and < 1 % in the LTS stages, respectively (Twigg, 1989).

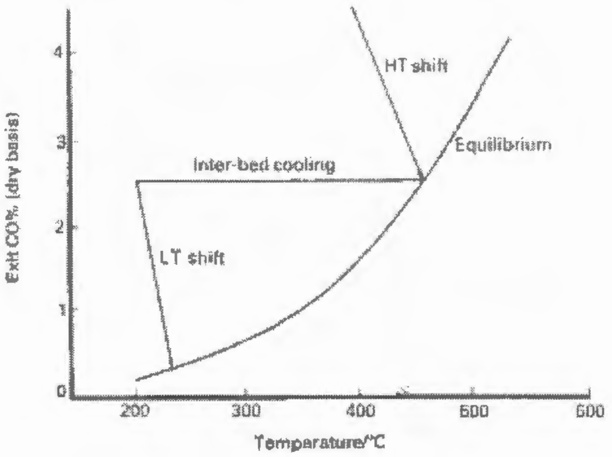

Figure 2.2: Exit CO concentrations as a function of operating temperature for the HTS/LTS implementation (Twigg, 1989)

The upper temperature limits of the respective zones are imposed by both thermodynamic conversion limitation (HTS) and catalyst deactivation due to thermally driven sintering of dispersed active metallic centres (LTS). The lower limits are determined by catalyst activity (HTS) and the dew point of water (LTS) - condensation on the catalyst surface creating intolerable mass-transport limitations.

2.2 Catalysts

2.2.1 High Temperature Catalyst – $Cu/Fe_3O_4/Cr_2O_3$

WGS in the HTS range is typically catalysed by the ternary oxide $CuO_x/Fe_3O_4/Cr_2O_3$, obtained by the *in situ* partial reduction of the as-supplied $CuO_x/\alpha\text{-}Fe_2O_3/Cr_2O_3$ catalyst precursor with hydrogen or CO prior to exposure to feed. Copper (as a group IB metal) doping promotes WGS activity and catalyst reduction at low temperatures, while chromia increases catalyst life by retarding thermally driven crystallite sintering.

The composition of a typical commercial HTS catalyst (Süd-Chemie's 'G-3C') is reported as 2% Cu, 62% Fe and 6% Cr (3% CuO, 89 % Fe_2O_3 and 8 % Cr_2O_3) by mass (Roberts, 2001).

The HTS catalyst may be prepared via co-precipitation (CP) of the mixed hydroxides from a solution of the respective sulphates using sodium carbonate. Careful calcination converts the precipitated hydroxycarbonates to oxides (α-Fe_2O_3 in the case of iron) and must avoid the unwanted over-oxidation of chrome to the (VI) oxide CrO_3. CrO_3 presents a problem during catalyst commissioning as it has a significant heat of reduction (ΔH_{rxn} = -684.7 $kJ.mol^{-1}$ for reduction by hydrogen and -808.2 $kJ.mol^{-1}$ for reduction by CO). Associated with this is the risk of hot spot formation during introductory reduction, which must thus be carefully controlled in order to avoid over reduction of Fe_3O_4 to iron metal, which catalyses methanation (i.e complete hydrogenation) and CO disproportionation.

Fe_3O_4 based catalysts can be operated in the presence of H_2S (where a certain fraction of the iron oxide will be converted to the sulphide) with some success, as conversion to the sulphide is reversible, and the converted sulphide also catalyses the WGSR (Twigg, 1989).

2.2.2 Low Temperature Catalyst - $Cu/ZnO/Al_2O_3$

WGS in the LTS region is typically accomplished over the dispersed metal catalyst $Cu/ZnO/Al_2O_3$, which in its active state consists of metallic copper clusters homogeneously distributed across a ZnO support surface. Al_2O_3 is included as a structural promoter to inhibit copper cluster sintering (a phenomenon that characteristically defines the upper bound of the LTS region) and improve the strength of the composite material (making forming possible).

The composition of a typical commercial LTS catalyst (Süd-Chemie's 'C 18-7') is reported as 34% Cu, 38% Zn and 5% Al (43% CuO, 47% ZnO and 10% Al_2O_3) by mass.

Analagous to the Fe_2O_3 derived HTS catalyst, the LTS catalyst is supplied in an oxidized form ($CuO/ZnO/Al_2O_3$) and requires an introductory reduction, generally by hydrogen diluted in a suitable inert (often natural gas).

ZnO is very susceptible to sulphide formation (ZnO beds being employed industrially specifically as sulphur traps, a commercial example being Süd-Chemie's G-72D) and, problematically, sulphide formation is associated with copper sintering. As a result, H_2S levels of < 0.1 ppm are required industrially and even then poisoning is still appreciable. Chlorine is also regarded as a catalyst poison, the formation of volatile copper chlorides increasing the rate of copper sintering. Cu is pyrophoric and care must be taken to avoid exposure of the reduced catalysts to oxygen during operation, in order to prevent sintering.

2.3 WGS in Fuel Processors for Hydrogen Fuel Cells

2.3.1 Hydrogen Fuel Cells

A fuel cell is effectively a modified voltaic cell. Two isolated redox half-reactions are coupled and use is made of the electric current resultant from the necessary external flow of electrons between the two half-cells to do work in some electromechanical device (for example an electric motor). A hydrogen fuel cell (HFC) combines the oxidation of hydrogen (eqn 2.11) with the reduction of oxygen (eqn 2.12) to generate an electric current, producing water as the sole emission (eqn 2.13).

Table 2.3: Electro-chemical reactions constituting a HFC

System	Reaction			$\Delta E°$ (V)	Equation
Anode	H_2	→	$2H^+ + 2e^-$	0	2.11
Cathode	$O_2 + 4H^+ + 4e^-$	→	$2H_2O$	1.23	2.12
Cell	$2H_2 + O_2$	→	$2H_2O$	1.23	2.13

The operation of a HFC, like any galvanic or electrolytic cell, is contingent on there being separate and distinct paths for cationic and anionic charge carriers. In the case of the HFC, the anionic charge carriers are electrons which migrate from the anode to the cathode via an external electric circuit, generating power by doing electrical work in the process. The cationic charge carriers are protons, which migrate (again from the anode to the cathode) via an electronically non-conductive electrolyte. This electrolyte is described as either a proton exchange- or as a polymer electrolyte- membrane (PEM), it being a selectively proton-permeable membrane constructed from a polymeric ion-exchange resin. The redox reactions occur heterogeneously at the interface of the typically platinum group metal based electrodes.

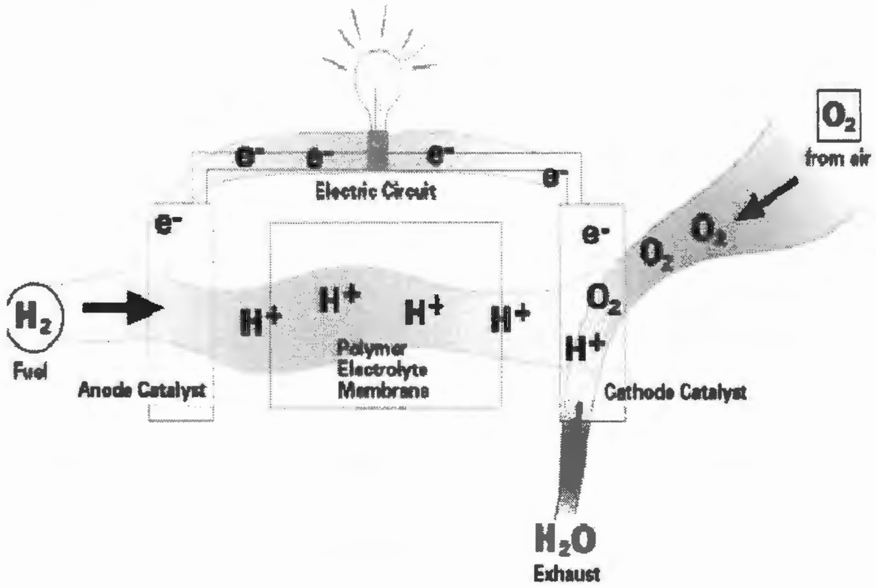

Figure 2.3: PEM hydrogen fuel cell abstract

The first HFC was demonstrated by W.R. Groves in 1839 but interest in the technology only resurged in the 1960's as a result of NASA's search for a clean and reliable source of electric power for use in their Gemini space programme. More recently, HFC technology has been proposed as a potential means of generating 'clean' power for vehicles driven by electric motors and designed to meet stringent emission criteria legislated by various progressive districts (e.g. the state of California in the USA). Several major automotive manufacturers (e.g. Ford, Daimler-Chrysler, Honda, Mitsubishi, etc.) currently run major R&D programmes in this area and prototype vehicles are in limited production. Moreover, since HFC's are a source of stable and reliable electrical energy, they have sparked particular interest in contexts where continuity of supply is critical, for example in information processing (banking, finance, telecommunications).

2.3.2 Fuel Processor Overview

Since the sourcing of gaseous hydrogen from on-board high pressure tanks is precluded by the low energy density of hydrogen gas (which makes the distribution and storage of sufficient material impractical), an alternative solution must be found. An option is on-board hydrogen production via the chemical conversion of a suitable hydrocarbon, a task accomplished in a unit separate to the fuel cell itself, and referred to as the fuel processor.

In terms of this conversion, while steam reforming is capable of producing a hydrogen rich stream, even after process optimisation the product inevitably contains significant amounts of CO. Since CO chemisorbs strongly on the platinum catalytic electrode of the fuel cell, reducing the number of sites available for redox activity, it is essential that the activity of the electrode be maximised. By the estimate of Urban *et al.* (2001) this means that the hydrogen rich stream supplied to the HFC must carry CO at a concentration lower than 10 ppm.

This target can be achieved by catalytically oxidising the CO to inert CO_2 in two subsequent stages, first with water (the WGSR, with the added dividend of increasing overall hydrogen production), then (preferentially) by oxygen (PrOx).

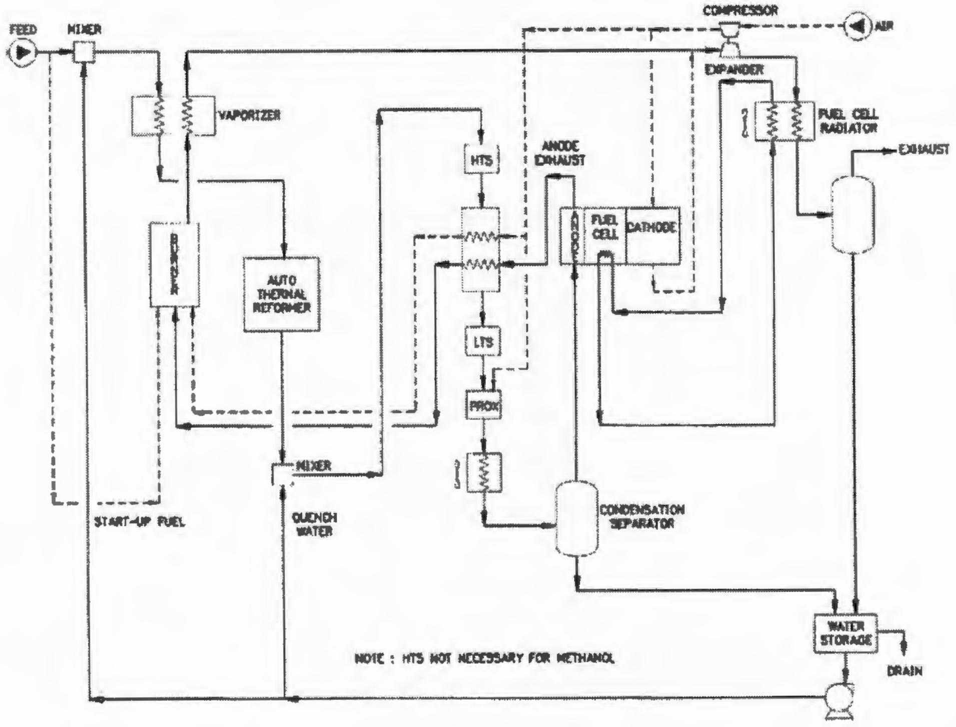

Figure 2.4: Process diagram for a typical integrated PEM-HFC fuel-processor / fuel-cell system (Moon *et al.*, 2001)

2.3.4 WGS Reactor, Catalyst and Feed Composition

The composition of the steam reformer product will depend to some extent on the exact hydrocarbon or hydrocarbon mix that is fed, in this case methanol. The HotSpot™ methanol reformer (Edwards, 1998) developed by Johnson-Matthey is considered as a model reformer. This is a prototype developed specifically for use in an on-board fuel-processor. A typical product composition is given as 5% CO, 15% CO_2, 40% H_2 and 40% N_2 (on a dry gas volume basis) and the reactor runs at a temperature of 400°C.

The performance requirements of the WGS reactor are thus dictated by the feed composition from the preceding reformer stage, and the conversion capabilities of the subsequent PrOx stage. Bearing this in mind, Ghenciu (2002) determined an exit CO concentration below 5000 ppm (0.5 %) for the WGS stage in his review of the overall system.

A number of issues prevent simply optimising the existing commercial catalysts for the HFC process conditions:

- While the carefully controlled and time consuming pre-reduction required by the commercial catalysts is not prohibitive in the case of large scale industrial reactors operating at steady state for months or more subsequent to initial catalyst commissioning, it is not appropriate for HFC applications where start up and shut down is likely to occur more frequently.

- During system start up, exposure to oxygen due to incomplete partial oxidation of the hydrocarbon feed in the steam reformer is likely to occur, resulting in the exothermic partial oxidation of the active catalyst to an inactive form, often driving crystallite sintering for additional deactivation.

- The LTS catalyst is too susceptible to sulphur poisoning to be used in the case of a mineral fossil fuel derived gasoline/petrol fraction hydrocarbon being used a feed.

- Size and mass restrictions are extreme in the case of fuel processors intended for mobile applications, and as a result a highly active shift catalyst is required to meet the stringent demands. The conventional shift catalysts are simply not active enough to function in a shift reactor of acceptable dimensions.

For these and other reasons there exists a need for new catalysts specifically optimised for HFC use.

2.3.5 Reactions Catalysed by Au/MO Type Materials

Au/MO type materials are potentially economically competitive heterogeneous catalysts for a number of different gas-phase reactions (Thompson, 1999; Haruta, 1997; Bond *et al.*, 1999):

- Selective oxidation of CO (by oxygen) in hydrogen (PrOx)
- Various selective partial oxidations (including propylene epoxidation and acrolein hydrogenation)
- Selective oxidation of CO (by oxygen) in hydrogen (PrOx)
- Hydrocarbon combustions
- WGS
- NO reduction (to either N_2 or N_2O) using hydrogen, CO or propene
- CO_x hydrogenation (methanol synthesis)

Commercial processes manufacturing vinyl acetate from ethylene and acetic acid using SiO_2 supported bimetallic Pd-Au catalyst are currently in operation, and use of Au/Al_2O_3 to reduce NO_2 to NO using H_2 has recently been introduced in the commercial production of nylon-66. Air cleaners using $Au/\alpha\text{-}Fe_2O_3$ to decompose malodorous amines in toilets are available in Japan.

Numerous applications of the unrivalled ability of Au/MO type materials to catalyse the oxidation of CO at or below ambient temperature are likely to go into economic production in the near future. Some expected implementations are in CO gas-masks and recycling rebreather systems, and in CO_2 lasers (where Au/MO surfaces regenerate CO_2 inadvertantly converted to CO via decomposition of high-energy CO_2 species produced during normal laser operation).

Heterogeneous Catalysis by Au/MO in Synthesis Gas

3

The addition of dispersed gold has been widely reported to promote WGS activity in a number of transition metal- and lanthanide metal- oxides, including TiO_2, ZnO, Al_2O_3 (Sakurai *et al.*, 1997), α-Fe_2O_3 (Andreeva, 1996a & 1996b), Co_3O_4 (Andreeva *et al.*, 1998), ZrO_2 (Tabakova *et al.*, 2000) and CeO_2 (Andreeva *et al.*, 2002a; Fu *et al.*, 2003a, 2003b).

These Au/MO type materials are in general capable of catalysing a number of chemical transformations in addition to the WGSR under the synthesis gas (H_2, CO, CO_2) feed utilised. Of the possible reactions, carbon oxide (CO, CO_2) hydrogenation to methanol (CO: eqn 3.1; CO_2 eqn 3.2) is considerable.

$$CO_2 + 3H_2 \leftrightarrows CH_3OH + H_2O \qquad \text{(eqn 3.1)}$$
$$CO + 2H_2 \leftrightarrows CH_3OH \qquad \text{(eqn 3.2)}$$

Methanol synthesis at the requisite elevated pressure (in this specific case 800 kPa and 5 MPa) from CO_x over gold supported on ZnO, TiO_2, ZrO_2, Fe_2O_3, $La(OH)_3$, NiO, Co_3O_4 and Al_2O_3 has been investigated (Sakurai *et al.*, 1993, 1995, 1996), and provides a valuable insight into the catalytic behaviour of Au/MO in synthesis gas feeds:

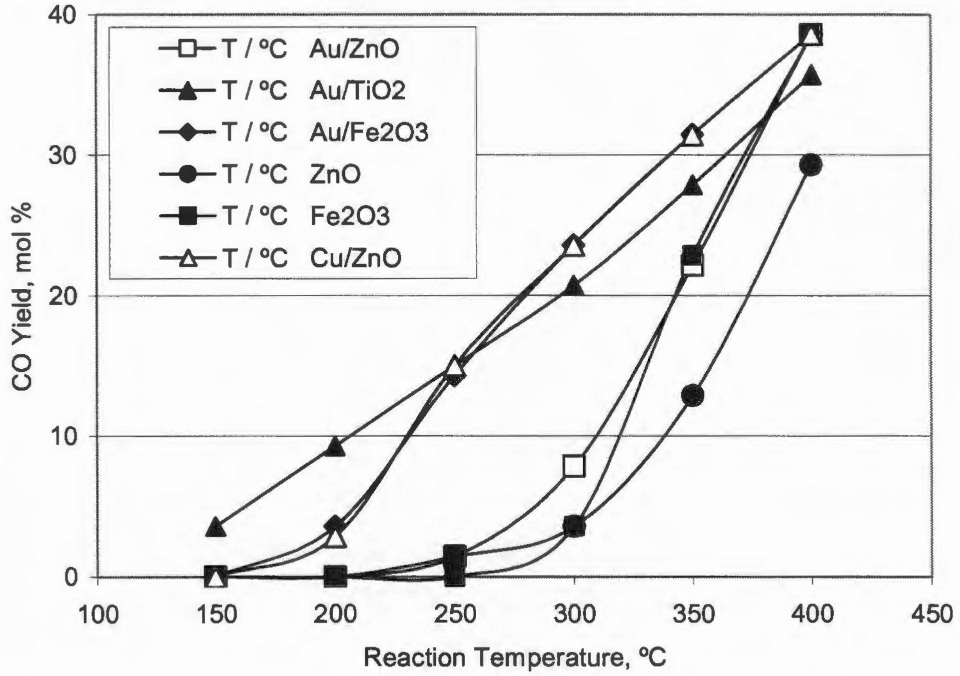

Figure 3.1: CO conversion as a function of reaction temperature for reverse WGS activity over Au/MO. Au/(support metal) = 1/19 in atomic ratio (Sakurai *et al.*, 1993)

WGS activity (figure 3.1) is observed to increase with support acidity, with Au/TiO_2 being the best of the acidic supports (and thus best overall) and Au/ZnO the worst of the basic (and thus worst of all).

On this basis (with similar gold loadings and crystallite sizes) comparative WGS activity below 300°C can be summarised as in eqn 3.3.

$$Au/TiO_2 > Au/Fe_2O_3 \cong Cu/ZnO >> Au/ZnO > ZnO > Fe_2O_3 \qquad \text{(eqn 3.3)}$$

This qualitatively agrees with the summary of Andreeva (2002b), eqn 3.4.

$$Au/Fe_2O_3 \cong Au/TiO_2 \cong Au/ZrO_2 > Au/Co_3O_4 \qquad \text{(eqn 3.4)}$$

From Sakurai *et al.* (1997) [not the data of figure 3.1] the following WGS activity comparison by turn over frequency (both per total- and per exposed surface- gold atom) for materials 5% gold by mass with mean gold crystallite size in the range 3 – 5 nm can be made (eqn 3.5).

$Au/TiO_2 > Au/Al_2O_3 > Au/Fe_2O_3 > Au/ZnO > ZnO$ (eqn 3.5)

This suggests the following series in terms of LTS activity (eqn 3.6).

$Au/Fe_2O_3 \cong Au/TiO_2 \cong Au/ZrO_2 \cong Cu/ZnO >> Au/ZnO > ZnO > Fe_2O_3$ (eqn 3.6)

Methane formation is observed over Au/TiO_2 (T > 250 °C) and Au/Fe_2O_3 (T > 300°C) with increasing pressure (from at least 800 kPa upward), but is negligible at pressures approaching ambient (Sakurai *et al.*, 1997).

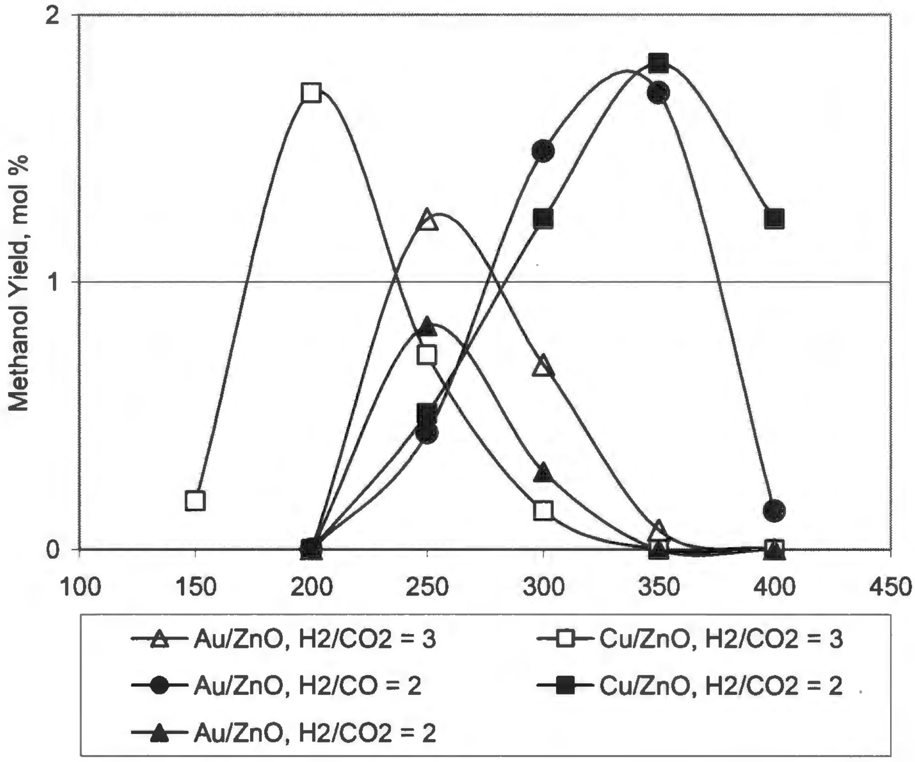

Figure 3.2: Methanol synthesis from CO_2, CO (respectively) over Au/ZnO and Cu/ZnO. Au/(support metal) = 1/19 in atomic ratio. (Sakurai *et al.*, 1993)

Key to legend: Catalyst, H_2/CO_x molar ratio in feed

Methanol formation, from either CO (eqn 3.1) or CO_2 (eqn 3.2), becomes appreciable at higher pressures (driven by reaction stoichiometry). CO_2 is hydrogenated to methanol at lower temperatures than CO, with Au/ZnO exhibiting greatest overall yield and selectivity (at 250°C for 800 kPa total pressure, H_2/CO_2 = 2 in the feed), although Au/Fe_2O_3 is reported to be more active at lower temperatures (e.g. 200°C). Methanol selectivity and yield is observed to reach a maximum for intermediate temperatures, while increasing pressure increased yield over all supports.

3.1 Underlying Reaction Mechanism & Active Sites

The fine mechanistic detail of the WGS reaction over even the traditional catalysts is still debated. The two limiting cases, associative and regenerative, were initially proposed by Armstrong and Hilditch in 1920, for a copper-chromite catalyst. It has been thought that reaction in the LTS range over $Cu/ZnO/Al_2O_3$ occurs via the associative route, whereas the regenerative mechanism is applicable in the HTS zone over $Cu/Fe_3O_4/Cr_2O_3$ (Twigg, 1989). The subject is comprehensively reviewed by Rhodes *et al.* (1995).

3.1.1 Associative Mechanism

In its most general form, the associative mechanism involves the adsorption of CO and H_2O, followed by their direct reaction to form an unspecified intermediate ([*]), which then decomposes to yield CO_2 and H_2. (eqn 3.7)

$$CO_{(g)} + H_2O_{(g)} \rightarrow CO_{(ads)} + H_2O_{(ads)} \rightarrow [*] \rightarrow CO_2 + H_2 \qquad \text{(eqn 3.7)}$$

In 1969 Yurieva considered this process as a classical Langmuir-Hinshelwood case (eqns 3.8 ... 3.12):

$$CO_{(g)} \rightarrow CO_{(ads)} \qquad \text{(eqn 3.8)}$$
$$H_2O_{(g)} \rightarrow H_2O_{(ads)} \qquad \text{(eqn 3.9)}$$
$$CO_{(ads)} + H_2O_{(ads)} \rightarrow [*]_{(ads)} \rightarrow CO_{2(ads)} + H_{2(ads)} \qquad \text{(eqn 3.10)}$$
$$CO_{2(ads)} \rightarrow CO_{2(g)} \qquad \text{(eqn 3.11)}$$
$$H_{2(ads)} \rightarrow H_{2(g)} \qquad \text{(eqn 3.12)}$$

Possible intermediates are carboxylate (formate, CO_2^-) and carbonate (CO_3^{2-}) derivatives. These species have been detected via a number of diverse analytical techniques but the question as to whether these are formed *during* the WGS reaction as intermediates, or *from* the WGS products has not been completely resolved. Nevertheless for catalysts operating under conditions capable of sustaining the WGS reaction there is convincing evidence for the presence of formate species (Rhodes *et al.*, 1995).

3.1.2 Regenerative Mechanism

The regenerative mechanism involves the successive oxidation (eqn 3.13) and reduction (eqn 3.14) of the catalyst by H_2O and CO respectively, generating H_2 and CO_2.

$$H_2O + \textit{reduced state} \rightarrow H_2 + \textit{oxidized state} \qquad \text{(eqn 3.13)}$$
$$CO + \textit{oxidized state} \rightarrow CO_2 + \textit{reduced state} \qquad \text{(eqn 3.14)}$$

Considering these redox processes as occurring successively at a single metal centre M, they can be summarised as follows:

$$H_2O + M(x) \rightarrow H_2 + O{=}M(x+2) \qquad \text{(eqn 3.15)}$$
$$CO + O{=}M(x+2) \rightarrow CO_2 + M(x) \qquad \text{(eqn 3.16)}$$

The active metal centre can thus be said to cycle through (x) and (x+2) oxidation states, classifying the regenerative case as a member of the Mars van Krevelen class.

3.2 Genesis of WGS Activity

3.2.1 Apparent Dependence on Au Crystallite Size

The classical dispersion effect observed in heterogeneous catalysis by supported small metal crystallites results from the fact that, for a fixed quantity of material, a decrease in individual crystallite size results in an increase in the ratio of total exposed surface area to total occupied volume. In other words, decreasing the average crystallite size makes a greater fraction of the total material present available for catalytic action but does not affect the intrinsic reactivity of the active surface sites - as typically quantified by a turn over frequency (TOF) or rate of reactant conversion per active site.

However, in the case of metal oxide supported gold, when Cha *et al.* (1970) assessed the ability of Au/MgO to catalyse CO oxidation, the increase in activity that was observed with decreasing crystallite size appeared to exceed that which would have been expected purely on the basis of a classical dispersion effect. Furthermore, this deviation was reported to become appreciable only when the gold crystallite size decreased below 10 nm, a value first confirmed for oxidation of both CO and H_2 over gold supported on α-Fe_2O_3, Co_3O_4 and NiO (Haruta *et al.*, 1989). Later this value was further refined to 4 nm (specifically for CO oxidation) (Haruta *et al.*, 1993).

This trend has subsequently been thoroughly examined across a number of heterogeneous reactions catalysed by metal oxide supported gold, and can be summarized by saying that when gold is deposited on select metal oxides in the form of crystallites with diameters smaller than ~ 5 nm, it exhibits high activities and/or selectivities for a number of gas phase reactions. These include, but are not necessarily limited to, the combustion of CO and saturated hydrocarbons, the oxidation-decomposition of amines and halogenated organic compounds, the partial oxidation of hydrocarbons, the hydrogenation of carbon oxides, unsaturated carbonyl compounds, alkynes and alkadienes, and the reduction of nitrogen oxides. (Haruta, 1997)

3.2.2 Further Investigation of the Active Gold Site

Unfortunately, while it is abundantly clear that a high degree of dispersion is an essential requirement for activity in Au/MO type catalyst formulations, the actual active site has yet to be irrefutably established. Nonetheless, proposals can be informatively divided into 3 categories: cubooctahedral (or icosahedral) crystallites (often truncated by intersection with the surface plane of the support); very small polyatomic gold clusters (composed of some 10's of Au atoms); and atomically dispersed ionic gold.

TEM examination of calcined Au/MO materials inevitably reveals cubooctahedral gold structures attached to the support surface. These structures are typically either (effectively) complete cubooctahedra, bonded to the support surface at their basal face, or symmetrical, angular, disc-like structures a few atomic layers deep.

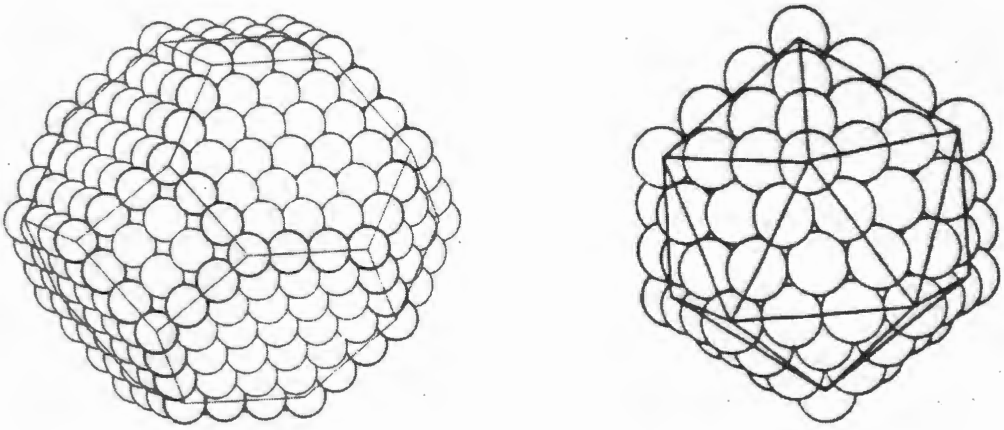

Figure 3.3: FCC cuboctahedron (left), FCC icosahedron (right), (Che *et al.*, 1989)

The cubooctahedron (a regular solid with 8 hexagonal faces and 6 square ones, for a total of 14) is predicted to be the minimum energy structure for FCC metal crystals of ~ 10 nm in size, but for significantly smaller particles a regular icosohedron (with 12 equilateral triangular faces) may be more favourable (Che *et al.*, 1989).

Claus *et al.* (2004) recently considered the ability to strongly influence the product selectivity in the hydrogenation of acrolein ($H_2C=CH-CH=O$, propenal, an α,β-unsaturated aldehyde) over Au/ZnO, by selectively decorating the exposed faces of the gold cubooctahedra with indium, to stem from an intrinsic difference in reactivity between gold atoms at edge/corner and face sites. (Selective hydrogenation of the double bond in propenal is difficult as the activation energy barrier to hydrogenation of the aldehyde oxygen to the alcohol is expected to be lower.)

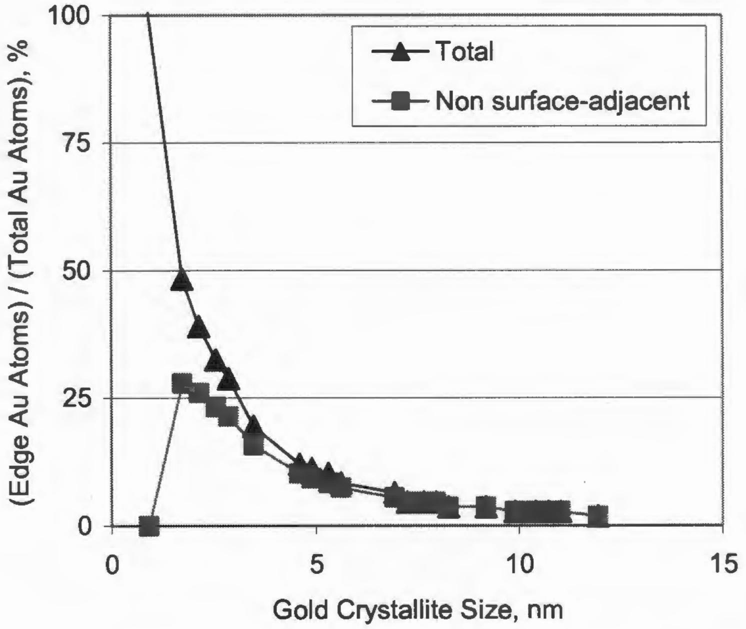

Figure 3.4: Step density as a function of FCC crystallite diameter: all step atoms vs. step atoms not-adjacent to support (Mavrikakis *et al.*, 2000)

Indeed, Mavrikakis *et al.* (2000) calculated CO and O_2 adsorption energy to be lower at stepped edges than on flat (111) terraces, in the case of unsupported slabs. They then extended this result, considering small, supported (Wülff type) FCC crystallites up to 6 atomic layers deep and showed simply that the fraction of free (defined as not being in direct contact with the support) edge atoms relative to the total number of atoms in the crystallite reaches a maximum for crystallites approximately 2 nm in diameter and 2 layers deep (figure 3.4).

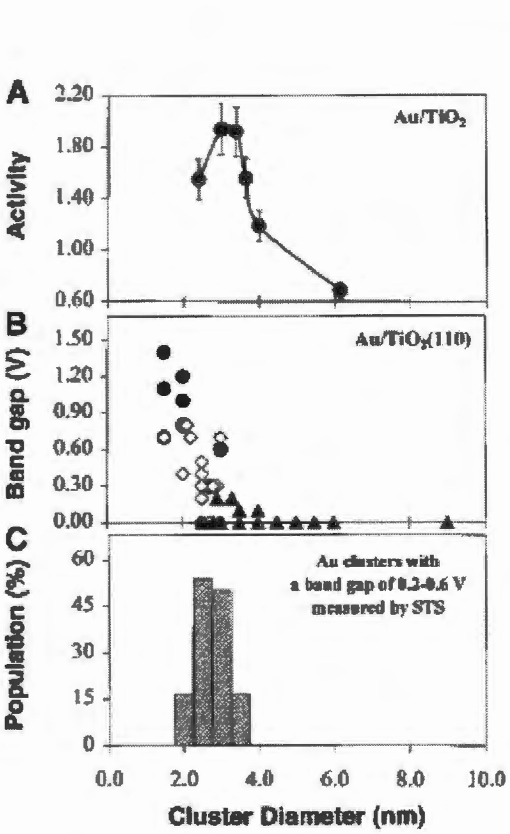

Figure 3.5

(top) CO oxidation activity at 350 K as a function of average Au crystallite diameter, assuming total Au dispersion

(middle) band gap of Au crystallite versus crystallite diameter as measured via scanning tunnelling spectroscopy for: 2-dimensional crystallites [solid circles], 3-d crystallites 2 atomic layers deep [empty squares], 3-d crystallites 3 atomic layers or more deep [solid triangles]

(bottom) population distribution for Au crystallites with a measured band gap of 0.2 – 0.6 V (Valden et al., 1998)

These findings are consistent with those of Valden *et al.* (1998), who prepared Au/TiO_2 via vapour deposition (300 K) and heat treatment (850K, 2 mins) of Au on TiO_2 single crystal and observed a strong crystallite size dependency for CO oxidation, with crystallites ~ 3.5 nm in diameter exhibiting maximum activity (figure 3.5). This is close agreement with an earlier report of a optimal size at 2 – 3 nm by Bamwenda *et al.* (1997) for CO oxidation over Au/TiO_2 prepared via deposition precipitation. Valden *et al.* (1998) correlate the maximum in WGS activity as a function of Au crystallite size to the phase transition from metallic to non-metallic (as reflected by the band gap energy) that they observe in 2 and 3 layer Au crystallites around this size.

The suggestion by Mavrikakis *et al.* (2000) that any quantum level condition is likely to be dependent on the least dimension of the structure, which is generally the cluster height rather than the diameter at base, does not seem to have received much attention in the general literature. (A height of approximately 1 nm is given for a 2 layer structure 3.5 nm in diameter at base, which would consist of about 300 Au atoms)

While all coordinatively unsaturated step/edge atoms may be responsible for activity, the contact structure of gold crystallites which yields the longest distance of perimeter interface appears to be important for the genesis of high activity at low temperatures (Haruta, 1997). An elegant investigation by Tsubota *et al.* (1998) considers a physical mixture of titania and nanometre dimensioned (5 nm) gold calcined at various temperatures in the range 473 K – 873 K, and reveals that although the uncalcined physical mixture is active, CO oxidation activity increases by over an order of magnitude with increasing calcination temperature. This is attributed to the increased gold-support interface achieved as the gold crystallites melt and increase their degree of contact with the support.

3.2.3 Support Associated Cationic Gold

Recent work by Fu *et al.* (2003a, 2003b), examining the WGS activity of gold promoted ceria, suggests that cationic gold incorporated into the ceria lattice may be responsible for the promotion of WGS activity in that material. They showed that the WGS activity of the material, which consists of nanometre scale (< 10 nm) gold crystallites supported on only slightly larger (also < 10 nm) lanthanum doped ceria crystallites (i.e. $Ce(La_y)O_x$), was unaffected by the leaching of the metallic gold component through exposure to aqueous sodium cyanide solution. The vast majority of the initially deposited gold may thus be irrelevant. XPS analysis of the catalyst indicated the preservation of gold in both +1 and +3 oxidation states with leaching, compared with the total removal of metallic gold.

Fu *et al.* (2003a) suggest that substitution of gold into the oxide lattice via diffusion at crystal defect sites is responsible for the formation of the activity enhancing species. This process is thought to occur during heat treatment of the deposited gold. Leaching of uncalcined materials produces an inactive catalyst, while high temperature (800°C) annealing of the support prior to gold loading (which is assumed to dramatically reduce the number density of defect surface sites as activation energy barriers to restructuring are overcome at higher temperatures) results in complete gold leaching and produces a totally inactive material. This seems to indicate that crystal defect surface sites are both essential to the incorporation of gold into the oxide lattice and intimately involved with the genesis of the *inherent* WGS activity of ceria.

Incorporation of cationic gold into the support lattice as a result of thermal treatment has also been observed via Au Mössbauer spectroscopy in the case of Au/Fe_2O_3 (Sze *et al.*, 1998).

TPR analysis reveals that this gold doping of the support lattice shifts reduction events associated with the transitions $CeO_2 \rightarrow Ce_2O_3$ (Fu *et al.*, 2003b) and $\alpha\text{-}Fe_2O_3 \rightarrow Fe_3O_4$ (Munteanu *et al.*, 1997) in either the surface, the bulk, or both, to lower temperatures.

Actually, doping of CeO_2 with Cu, Ni, (Li *et al.*, 2000) or Pt also promotes both these reduction events and WGS activity to lower temperatures. Pt/CeO_2 is reported to be the most active of all these promoters on both a mass and molar concentration basis (Jacobs *et al.*, 2004).

Au/MO Materials Synthesis

4

The catalytically active composite material designated Au/MO is prepared in a number of stages, moving from formation of the support metal oxide, to loading of gold in an oxidised state and finally reduction of this oxidised species to the metal (refer figure 4.1), to give the metal oxide supported dispersed metal composite.

In our case, a zinc oxide support is initially precipitated as the hydroxycarbonate from a solution of the soluble nitrate salt via addition of sodium carbonate base, then heat treated to force transformation to the oxide.

Basification of an aqueous solution of the gold salt $HAuCl_4$ using NaOH in the presence of the preformed support achieves precipitation of a gold(III) species loosely described as $Au(OH)_3$ on the solid support surface (a process referred to as deposition-precipitation, DP). When $(NH_4)_2CO_3$ is employed in the place of NaOH as a precipitating agent, the possibility that ion-exchange of a cationic gold species with surface hydroxyl protons occurs instead of- or in addition to- the precipitation of $Au(OH)_3$ exists.

Heat treatment of the composite material ($Au(OH)_3$/MO) results in decomposition, sintering and aggregation of gold species on the support surface to form discrete nanometre (and sub nano-metre) scale structures strongly bonded to the support. In some cases gold may migrate into at least the surface adjacent region of the support lattice.

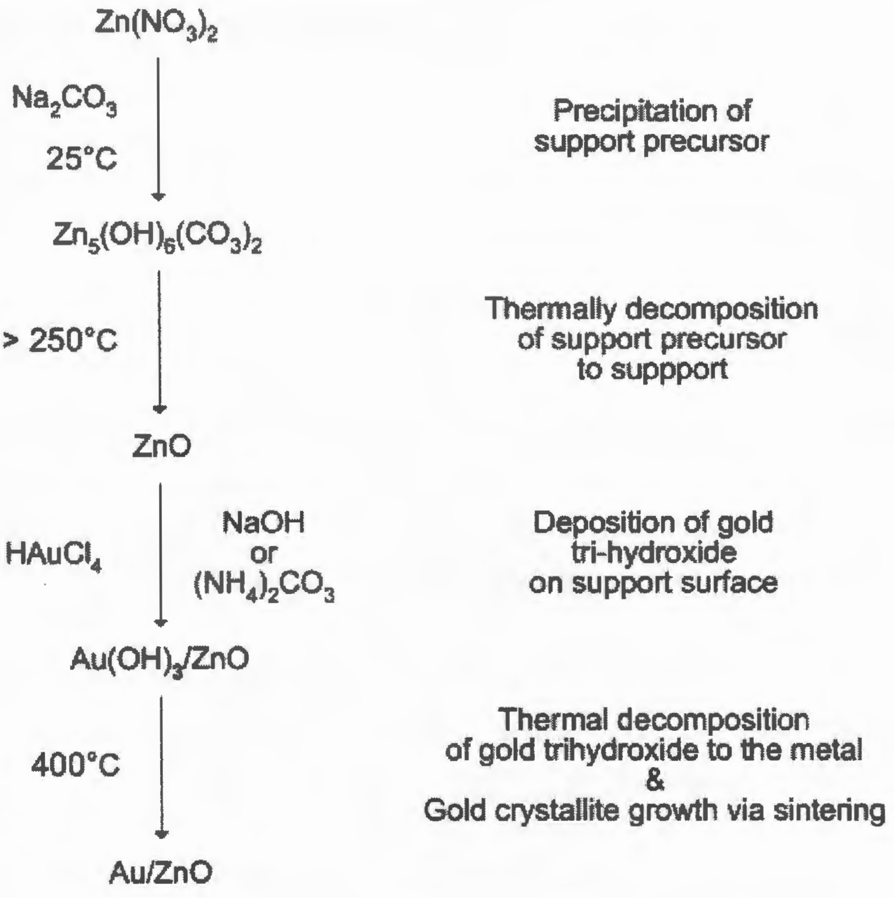

Figure 4.1: Overview of Au/MO synthesis in the case of Au/ZnO

4.1 ZnO Support

Zinc is precipitated in the form of the approximately stoichiometric hydroxycarbonate hydrozincite ($Zn_5(OH)_6(CO_3)_2$) from an aqueous solution of the nitrate (i.e. from zinc nitrate, $ZnNO_3$) via basification with Na_2CO_3. Extended heat treatment in oxygen (calcination) around 250°C converts it to the oxide (ZnO).

4.1.1 Precipitation of $Zn_5(OH)_6(CO_3)_2$

This is accomplished by adding an aqueous solution of zinc nitrate drop-wise to a solution of concentrated sodium carbonate. In this environment (high pH and CO_3^{2-} concentration) zinc is simultaneously precipitated as the mixed hydroxide (eqn 4.3) carbonate (eqn 4.1).

$Zn^{2+}.2NO_3^- + 2Na^+.CO_3^{2-} \rightarrow Zn^{2+}.CO_3^{2-} + 2Na^+.NO_3^-$ (eqn 4.1)

$2Na^+.CO_3^{2-} + H_2O \rightarrow Na^+.HCO_3^- + Na^+.OH^-$ (eqn 4.2)
$2Na^+.OH^- + Zn^{2+}.2NO_3^- \rightarrow Zn(OH)_2 + 2Na^+.NO_3^-$ (eqn 4.3)

The choice of Na_2CO_3 as precipitant is motivated by the comparative study by Wang *et al.* (2003) where the trend with respect to ZnO crystallite size (after calcination in air at 240°C for 4 hours) was determined to be $Na_2CO_3 < (NH_4)_2CO_3 < NaOH < NH_4OH$, the inverse of the trend with respect to N_2 BET surface area.

4.1.2 Thermal Decomposition of $Zn_5(OH)_6(CO_3)_2$ to ZnO

Complete decomposition (as confirmed by XRD analysis) of $Zn_5(OH)_6(CO_3)_2$ to ZnO (eqns 4.4 & 4.5) is reported to be achieved by heating to a temperature of at least 240°C in oxygen (Wang *et al.*, 2003) and corresponds to a mass loss of 26%.

$Zn(CO_3) \rightarrow ZnO + CO_2$ (eqn 4.4)
$Zn(OH)_2 \rightarrow ZnO + H_2O$ (eqn 4.5)

Further heating is expected to reduce only the total external surface area through crystallite sintering, leading to agglomeration (e.g. figure 4.2).

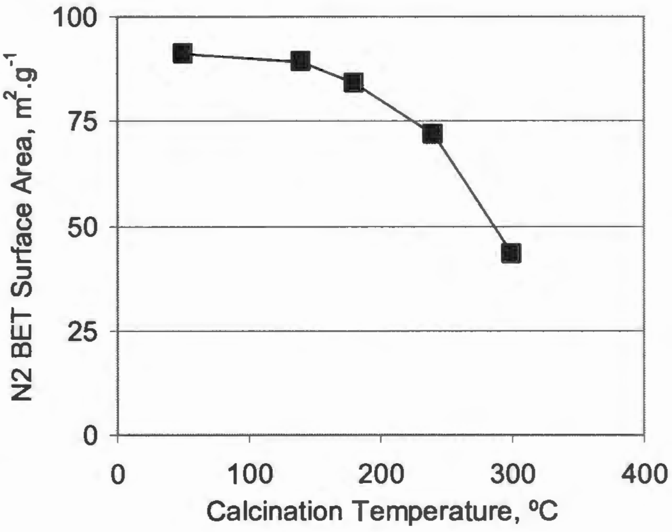

Figure 4.2: N_2 BET surface area as a function of calcination temperature (20% O_2 in Ar, 4 hours) for Au/ZnO prepared via Na_2CO_3 (Wang *et al.*, 2003)

4.2 Gold Loading

$Au(OH)_3$ is deposited on the surface of the support (yielding $Au(OH)_3/MO$), followed by calcination of the composite material in air to yield the catalytic material designated Au/MO.

4.2.1 Deposition-Precipitation of $Au(OH)_3$ on the Support Surface

$Au(OH)_3$ is deposited on the pre-formed metal oxide support surface through the basification of a suspension of the support in an aqueous solution of hydrogen tetrachloroaurate trihydrate (nominally $HAuCl_4$, but actually $[H_3O]^+[AuCl_4]^-.3H_2O$ (Cotton *et al.*, 1980)).

4.2.1.1 Gold Speciation in the Solution Phase

Any attempt to develop a rigorous understanding of the precipitation process is complicated from the outset by the fact that the equilibrium speciation of gold is strongly dependant on pH, oxidation potential and relative chloride concentration. For example, in aqueous solution yellow, square planar Au(III) $[AuCl_4]^-$ is in an appreciably temperature dependant equilibrium with colourless, linear Au(I) $[AuCl_2]^-$ (Pan *et al.*, 1991; Murphy *et al.*, 1998; Gammons *et al.*, 1997).

The dominant gold species in acidic, relatively concentrated, room temperature solutions obtained by dissolution of the hydrogen, sodium or potassium salt of the tetrachloroaurate ion (formed in aqueous solution by dissolution of $HAuCl_4$, $NaAuCl_4$, $KAuCl_4$) is $[AuCl_4]^-$, with a progressive increase in pH successively hydrolysing the metal centre (i.e. with hydroxide ligands successively substituting for chloride ones). In other words, when the dominant gold species at equilibrium is described by the formula $[AuCl_x(OH)_{4-x}]^-$ where x = 1..4, then x decreases with increasing pH (Peck *et al.*, 1991; Rich *et al.*, 1954; Bekker *et al.*, 1972).

The introduction of the $2NH_4^+.CO_3^{2-}$ ion-pair (or ion-triplet), as occurs when $(NH_4)_2CO_3$ is used as a precipitant, into chloride rich aqueous solution of Au^{3+} brings added complication, considering ammine (NH_3) complexes of Au^{3+} are known (e.g. $[Au(NH_3)_4]^{3+}$, (Skibsted *et al.*, 1974)).

4.2.1.2 MO Support Surface - The Electric Double Layer

Metal oxide surfaces are typically hydroxylated to various extents, that is to say they bear terminal hydroxyl groups. When immersed in aqueous solution these surface hydroxyls can be either protonated (eqn 4.8) or deprotonated (eqn 4.9) - the surface can thus be described as amphoteric. Protonation produces a positively charged surface ($S\text{-}OH_2^+$), while deprotonation produces one that is negatively charged ($S\text{-}O^-$).

$$S\text{-}OH + H^+ \leftrightarrows S\text{-}OH_2^+ \qquad \text{(eqn 4.8)}$$
$$S\text{-}OH + OH^- \leftrightarrows S\text{-}O^- + H_2O \qquad \text{(eqn 4.9)}$$

Overall charge neutrality is achieved through the existence of a close-lying layer of oppositely charged, labile solvent ions - OH^- in the case of (positive) protonated surfaces and H_3O^+ in the case of (negative) deprotonated surfaces. The system is referred to collectively as the electrical double layer and the electric potential at the boundary between the two layers relative to the solution bulk is known as the zeta- (ζ) or electrokinetic- potential (Atkins, 1998).

The position of the protonation/deprotonation equilibrium, and thus the sign and magnitude of the zeta potential, is understandably affected by solution pH with acidic solutions encouraging protonation, whereas alkaline solutions promote deprotonation. As a result of this pH dependence, for a given solid surface there exists a solution pH at which the rates of the protonation and deprotonation processes are equal and, at this point (zero zeta potential), the electrical double layer breaks down and the surface is electrically neutral. This pH is referred to as the isoelectric point of the solid (IEPS) or zero point of charge (ZPC). Approximate IEPS for Selected MO's (Parks, 1965) are given below.

Table 4.1: IEP's of relevant metal oxides

MO	IEP	
γ-Al_2O_3	8	
CeO_2	7	
TiO_2	6	Anatase
	5	Rutile
ZnO	9	

4.2.1.3 Ion-Exchange

On the basis of coulombic attraction, below its IEPS the surface of a metal oxide in aqueous solution will adsorb anions from solution (anion-exchange, eqn 4.10), and above its IEPS cations (cation-exchange, eqn 4.11).

$$S\text{-}OH_2^+ + A^- \leftrightarrows S\text{-}OH_2^+A^- \qquad \text{(eqn 4.10)}$$
$$S\text{-}O^- + C^+ \leftrightarrows S\text{-}O^-C^+ \qquad \text{(eqn 4.11)}$$

The equilibrium ion-exchange capacity of the surface increases as the solution pH moves further away from the IEPS. (Che *et al.*, 1989)

4.2.1.4 Ensuring Precipitation on the Support Surface

Although both nucleation and particle growth can occur both at the surface of the insoluble support and in the solution bulk, control of the gold concentration around 1×10^{-3} $M.dm^{-3}$, pH of 6 to 10, and temperature of the aqueous $HAuCl_4$ solution between 50°C to 90°C enables selective deposition of $Au(OH)_3$ on the surfaces of the support metal oxides, and minimizes precipitation in the liquid phase (Haruta, 2004). Presumably this is possible at least in part because certain (defect) surface features are natural locations for the adsorption of metal atoms during cluster growth. The calculations of Phala *et al.* (2004) support this view in the case of gold supported on zinc oxide, where adsorption of gas-phase $Au(OH)_3$ onto so called vacant zinc interstitial surface sites of the support was determined to be exothermic, thus energetically favourable.

4.2.1.5 Characterisation of the Precipitated Species

It is long established that, in the absence of a support, basification of an initially acidic solution of $AuCl_4^-$ with an alkali metal hydroxide produces hydrous gold(III) hydroxide, $Au(OH)_3$ (Roseveare *et al.*, 1927). However, the precipitated material is typically non-stoichiometric and of low crystallinity (Muller *et al.*, 1969). When basification is effected in the presence of a solid metal oxide such that nucleation and particle growth on the support surface are possible, surface and oxidation state characterisation using XPS, EXAFS and Mössbauer indicates that gold with a signature corresponding to $Au(OH)_3$ can be deposited as an evenly dispersed layer on the surface of the support (e.g. Hodge *et al.*, 2002; Park *et al.*, 1999).

4.2.2 Calcination of $Au(OH)_3$/MO

4.2.2.1 Thermal Transformation of the Precipitated Gold Species

According to numerous XPS, EXAFS and Mössbauer oxidation state characterisation studies (e.g. Hodge *et al.*, 2002; Park *et al.*, 1999), heat treatment (in either oxygen or hydrogen) of gold initially precipitated on the support surface in the (III) oxidation state as the trihydroxide $Au(OH)_3$ results in the transformation of the majority of the material first through dehydration, to the trioxide (Au_2O_3), then via auto-reduction to the metal (eqn 4.12).

$$Au_2O_3 \quad \leftrightarrows \quad 2Au + 3/2O_2 \qquad \text{(eqn 4.12)}$$

In the bulk state, while decomposition of the trioxide to the metal is spontaneous at room temperature ($\Delta G_{rxn} = -79.97\ kJ.mol^{-1}$, (Buehrer *et al.*, 1927)), the process appears to be kinetically rate limited under ambient conditions. Muller *et al.* (1969) report that, for a sample (of the unsupported bulk oxide) stored in dry air at ambient temperature, decomposition (as monitored by XRD analysis) was undetectable after 2 weeks, but 80% complete after 18 months. The rate of decomposition was reported to increase with temperature but to decrease with increasing oxygen partial pressure. The reported findings agree qualitatively with the Merck Index (1996) entry, which describes Au_2O_3

decomposition (presumably in air at atmospheric pressure) as beginning at 110°C and being complete at 200°C.

In the case of supported materials, while in qualitative agreement with bulk material studies, quantitative variation with the substrate is inevitable. For example, Tsai *et al.* (2003) observed the decomposition half-life for a 4 nm deep layer of Au_3O_3 supported on metallic gold substrate (prepared via exposure of gold ribbon to oxygen plasma) to be 22 hours at 22°C.

4.2.2.2 Sintering & Gold Crystallite Formation

While deposition precipitation appears to produce an even layer of $Au(OH)_3$ on the surface of the support, heat treatment in oxygen ($Au/\alpha\text{-}Fe_2O_3$ [CP, air @ 400°C (Hodge *et al.*, 2002)] or hydrogen (Au/ZnO [IMP, H_2 @ 300°C (Mohr *et al.*, 2003)]) at ambient pressure typically results in sintering to form either complete or truncated cubooctahedral crystallites, the thermodynamically favoured structure for the small (gold) face centred cubic crystallites (see §2.2.2.2). The truncated crystallites are typically a few atomic layers in height and hexagonal when viewed from above. The intuitive expectation that nucleation will occur preferentially at defective surface sites has been observed in practice by at least Valden *et al.* (1998), when the sintering gold species was found to preferentially nucleate on the step edges of the TiO_2 (110)-(131) substrate after vapour-phase monolayer deposition. The formation of so called 'multiply twinned particles' via the symmetrical aggregation of individual cubooctahedral crystallites is also frequently observed (e.g. Claus *et al.*, 2004).

The thermodynamics and kinetics of gold sintering are reviewed in detail elsewhere (Campbell, 1997). However, empirical observation (e.g. Oh *et al.*, 2002) suggests that the presence of (residual) chloride on the support surface during thermal treatment encourages sintering, possibly through the formation of more mobile gold-chloride complexes, a well-established phenomenon in the case of copper (Twigg, 1989).

4.2.2.3 Control of Post-Calcination Gold Crystallite Size

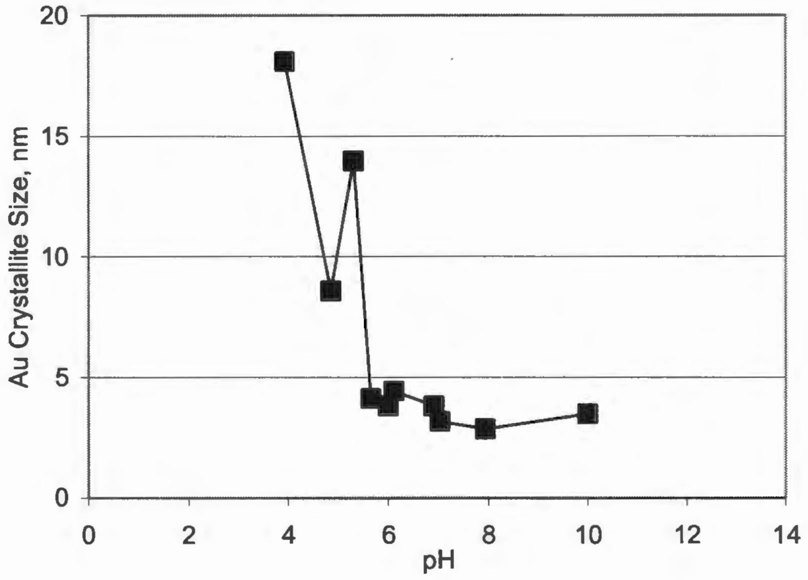

Figure 4.3: Post calcination gold crystallite size as a function of DP pH, for Au/TiO_2 (Haruta, 1997)

Valden *et al.* (1998) are clearly of the opinion that the initial Au support surface coverage determines the post-calcination Au crystallite size, at least when gold is deposited by PVD and subsequently annealed (calcined) at elevated temperature. On the basis of the surface potential argument already made, if the total amount of gold precipitated on the surface is assumed to be a decreasing function of pH (which it has unanimously been reported to be, e.g. Wolf *et al.* (2002) for Au/TiO_2; figure 4.4), then the application of Valden's result produces the reduction in post-calcination gold crystallite diameter with increasing ageing pH observed by Haruta (1997; figure 4.3).

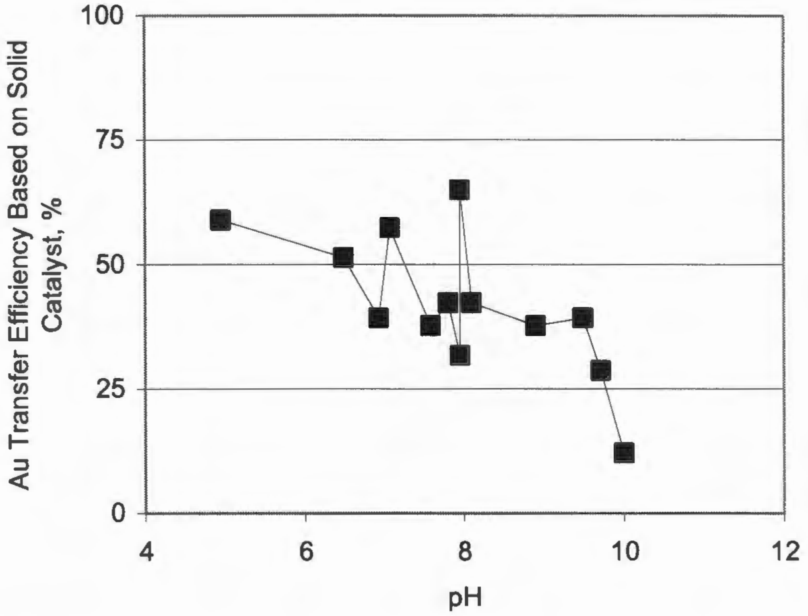

Figure 4.4: Au transfer efficiency based on the Au content of the solid catalyst as a function of ageing pH for Au/TiO$_2$ catalyst prepared via standard DP. (Wolf *et al.*, 2002)

4.2.3 Comparison with Ion-Exchange Preparation of Cu/MO and PGM/MO

It seems distinctly plausible that the preparation method of Fu *et al.* (2003b), which employs $(NH_4)_2CO_3$ ostensibly as a precipitating agent, and operates at basic pH, may be better classified as an ion-exchange when one considers analogous work – with Cu/SiO$_2$ (Kohler *et al.*, 1987a; Kohler *et al.*, 1987b) and Pd/SiO$_2$ (Bonivardi *et al.*, 1990).

The combination of the strong adsorption of metal ammine ($M(NH_3)_x^{y+}$) complexes on metal oxide support surfaces (reported as early as 1930 by Smith *et al.* for platinum- and palladium- ammine complexes on silica) combined with the cation-exchange phenomenon has been exploited in the literature to prepare metal oxide supported dispersed metal materials (e.g. Cu/SiO$_2$: Kohler *et al.*, 1987a; Kohler *et al.*, 1987b; Pd/SiO$_2$: Bonivardi *et al.*, 1990);

The metal-ammine complex is typically formed *in situ* via dissolution of a suitable metal complex (e.g. metal nitrate) in dilute (basic) ammonia solution. Introduction of the support as the solid metal oxide followed by appropriate pH adjustment results in the exchange of the cationic metal-ammine complex for surface hydroxyl protons.

In the case of Cu/SiO_2 prepared in this manner, it is reported (Kohler *et al.*, 1987a; 1987b) that copper is present in two forms after washing: atomically dispersed ion-exchanged Cu^{2+} species attached to 2 neighbouring silanol groups, and aggregated $Cu(OH)_2$ crystallites resulting from the precipitation of residual copper trapped in interstitial pore volumes. Calcination in air at 500°C converts the copper hydroxide to 'flat disc' or hemispherical oxide crystallites, but leaves the atomically dispersed silanol-bonded Cu^{2+} species unaffected. Subsequent reduction in H_2 at 400°C preserves the atomic level dispersion of the silanol bonded copper, but reduces the oxidation state to +1; the CuO crystallites are completely reduced to the metal.

4.2.4 Comparison of Preparation Techniques (DP, CP, Imp)

In light of the many inter-related factors affecting the overall activity of supported gold catalysts, it comes as no surprise that the activity of the final catalyst is highly (if indirectly) dependent on the preparation method.

Metal oxide supported precious metal catalysts are easily prepared via impregnation of the pre-formed support with an appropriate metal chloride salt in the case of the platinum group metals. However, the lower melting point of gold (Au 1064°C, Pd 1554°C, Pt 1769°C) and the high volatility of its chlorides promote agglomeration during calcination/reduction, making it more difficult to prepare small gold crystallites. Nevertheless, recent reports indicate that, with the appropriate control, impregnation can be employed to produce the requisitely small crystallites (e.g. Pawelec *et al.* (2005) report an Au crystallite size of less than 4 nm for γ-Al_2O_3 support).

Simultaneous coprecipitation of gold and support is inefficient in that the major fraction of the total gold is inactive, or at least associated with inactive bulk support rather than with the reactively accessible region immediately adjacent to the surface. However, recently Deng *et al.* (2005) have shown that low concentration $Au/Ce(La)O_2$ (<1% Au by mass) prepared via co-precipitation is at least as active as the corresponding material produced via sodium cyanide leaching of a parent material produced via DP, and more active than materials with higher gold contents.

This suggests that if the intention is to use gold to modify the support properties (i.e support doping) then simultaneous co-precipitation of the corresponding mixed metal (mixed) hydroxide is effective. However, when strongly support bonded nanometre-sized gold crystallites are desired, DP is more appropriate and offers a higher degree of control. DP 'is preferred to CP on the grounds that it [generally] gives a narrower particle size distribution' (Bond *et al.*, 1999).

More exotic methods of gold loading (e.g. vapour-phase deposition, grafting of organo-metallic gold compounds) do exist, but will not be further addressed here.

Research Objectives

3

The study is focussed on achieving two general and interrelated objectives. The first objective is the development and partial optimisation of a deposition-precipitation methodology for the synthesis of a zinc oxide supported dispersed gold catalyst with appreciable water gas shift performance, while the second is the determination of any significant relationships between the materials structure and the resulting catalytic activity.

To the end of achieving the first objective, two synthesis methods published in the literature are examined in turn. The first synthesis method is recommended by the group of Haruta (Tsubota *et al.*, 1995), and may be regarded as the classical deposition-precipitation method. In essence it consists of adding the insoluble support to a solution of hydrogen tetrachloroaurate salt subsequent to the setting of an appropriate solution pH and temperature, which are then maintained across an 'ageing' period. The second synthesis method, from the group of Flytzani-Stephanopoulos (Fu *et al.*, 2003b), recommends simultaneous differential addition of un-modified hydrogen tetrachloroaurate solution and base (specifically ammonium carbonate – to maintain constant pH) to a slurry of the support.

From a process point of view, there are two main considerations: the relative fraction of gold in solution taken up by the support – in other words the efficiency of transfer of gold from solution to support or the efficiency of gold deposition achieved; and the degree of support dissolution that occurs during the ageing period. These two characteristics are quantified, and an attempt is made close the gold mass balance across the process.

From a structure/activity perspective, it is important that the syntheses yield as large a fraction of small (<~ 5 nm) gold crystallites as possible – and the propensity of the syntheses to achieve this objective is quantified by measuring a sample of the gold crystallite population via transmission electron microscopy.

To the end of achieving the second objective, the relative activity of materials produced by the two methods must be compared, after first confirming that the addition of gold to the support does indeed promote its ability to catalyse the water-gas shift reaction.

Finally, the relationship between gold loading and catalytic activity is cursorily examined.

Experimental
Au/MO Materials Synthesis

6

In all cases 'water' refers to de-ionised water.

6.1 ZnO Support Synthesis

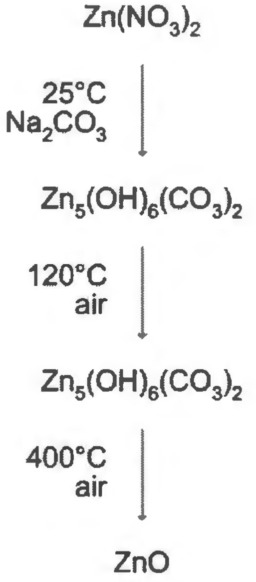

Figure 6.1: Synthesis of $Zn_5(OH)_6(CO_3)_2$ and ZnO

Two types of zinc oxide are used in this work, viz a commercial low surface area (3.6 $m^2.g^{-1}$) pre-formed material (> 99% purity, UnivAR, SAARChem, product 758-21-20, batch 35969) and a novel higher surface area (typically 30 $m^2.g^{-1}$) material synthesized via zinc hydroxycarbonate intermediate from zinc nitrate.

6.1.1 $Zn_5(OH)_6(CO_3)_2$ from $Zn(NO_3)_2$

Zinc nitrate hexahydrate ($ZnNO_3.6H_2O$, M = 297.5 $g.mol^{-1}$, 92 g = 310 mmol) is dissolved in water (100 ml) and added drop-wise to a solution of sodium carbonate (Na_2CO_3, 106 $g.mol^{-1}$, 98 g = 930 mmol; 400 ml water), stirring continuously. The slurry is stirred for a further 3 h and filtered. The filtered solid is washed 3 times by stirring in 200 ml water for 10 min followed by drying overnight at 120°C in static air. Finally, the dried solid is ground using a mortar and pestle until the entire mass can pass through a 500 μm sieve.

6.1.2 ZnO from $Zn_5(OH)_6(CO_3)_2$

Calcination of $Zn_5(OH)_6(CO_3)_2$ according to the procedure of §6.1.3 results in thermal decomposition to the ZnO.

6.1.3 Support Calcination

Precipitated support precursors are calcined in batches of up to 10 g. A fluidized bed reactor is used; synthetic air (21% O_2, 79% N_2) is supplied at a flow rate of 35 sccm. The temperature programme consists of an initial ramp at 1°$C.min^{-1}$ from ambient to the final temperature of 400°C, which is then maintained for 12 h prior to cooling to ambient temperature over a period of 1 h (at a rate of ~ 6°$C.min^{-1}$).

6.2 Gold

$HAuCl_4$ solution is obtained by dissolution of hydrogen tetrachloroaurate(III) trihydrate ($HAuCl_4.3H_2O$, M = 393.83 $g.mol^{-1}$, CAS# 16961-25-4) obtained from Aldrich Chemical Company in water.

6.2.1 Deposition-Precipitation of $Au(OH)_3$

Three variations are practiced; the first (standard DP) is canonical (Tsubota *et al.*, 1995), while the second (MDP-1) and third (MDP-2) are based on a related method reported by Fu *et al.* (2003b).

6.2.1.1 Standard DP (DP)

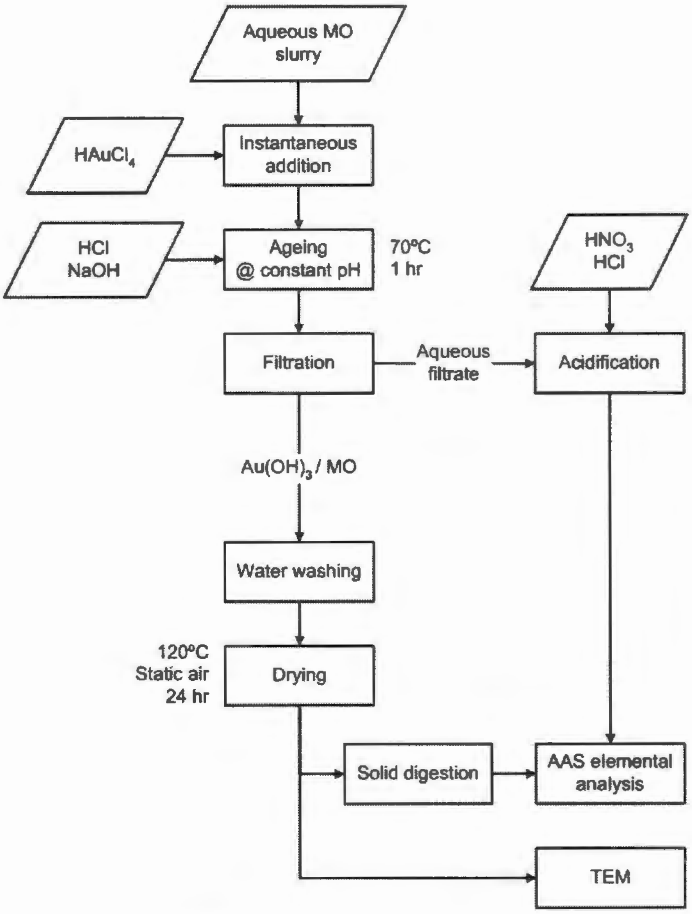

Figure 6.2: Overview of DP

450 ml water is added to 2 g of dry ZnO taken directly from the oven at 120°C, and the vigorously stirred slurry heated to 70°C. The appropriate volume of concentrated (0.032 mol.dm^{-3}) $HAuCl_4$ solution is added in a single action and the solution pH immediately adjusted to the desired set value via addition of concentrated sodium hydroxide solution (NaOH, 1.0 mol.dm^{-3}). The system is aged for 1 h, maintaining a constant pH value via drop-wise addition of either further NaOH solution, or concentrated HNO_3, as appropriate.

Filtration of the aged slurry using a buchner funnel separates the loaded support from the filtrate, while the filter paper is set aside for AAS elemental analysis. The loaded support is washed 3 times by stirring for 10 mins in 200 ml water and the water washes combined with the initial filtrate. The combined filtrates are acidified via addition of 10 ml

HNO_3 and 10 ml HCl in order to prevent inadvertent precipitation of gold during the interim between DP and filtrate analysis. The total volume of the combined filtrates is recorded. The loaded support and filter paper from the initial filtering are dried at 120°C in static air for 18 h.

6.2.1.2 Modified DP (MDP)

Slurry Formation

The appropriate mass of dry ZnO support is taken from the oven at 120°C and immediately suspended in 25 ml boiling water. A volume of room temperature water is then added such that the final volume of the system after addition of $HAuCl_4$ solution (ignoring the volume attributed to added HCl and $(NH_4)_2CO_3$) is 100 ml. For example, if 12 ml $HAuCl_4$ solution is to be added, then [100 – (25 + 12) =] 63 ml room temperature water would be added at this point. The slurry is stirred vigorously to ensure an even suspension.

Gold Deposition

Modified DP 1 (MDP-1)

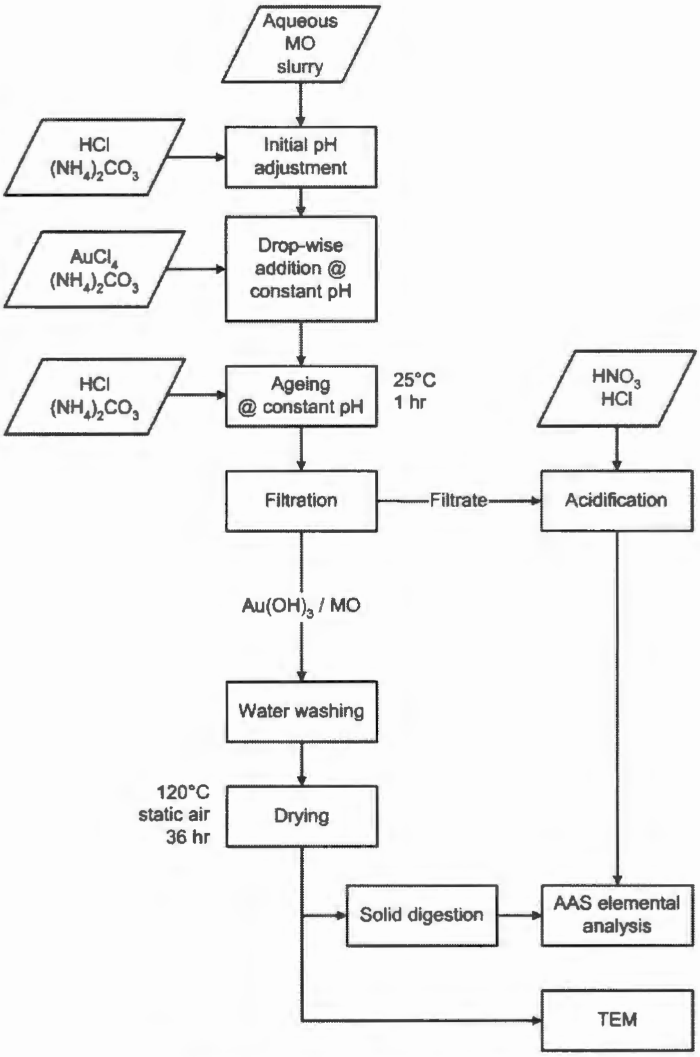

Figure 6.3: Overview of MDP-1

After an aqueous slurry of the support has been formed as detailed above (refer § Modified DP §§ Slurry Formation), the pH is adjusted to the appropriate value via addition of either 4 mol.dm^{-3} HCl solution (obtained by diluting concentrated HCl (12 mol.dm^{-3}) 1:2 with water) or concentrated ammonium carbonate solution ($(NH_4)_2CO_3$, M = 190.4 g.mol^{-1}; 190 g = 1 mol dissolved in 800 ml water). The appropriate volume of concentrated $HAuCl_4$ solution is then added drop-wise, typically over a 10 min period, maintaining a constant pH via simultaneous drop-wise addition of either HCl or

$(NH_4)_2CO_3$. On completion of $HAuCl_4$ addition, the system is aged for 1 h, maintaining constant pH via the addition of further HCl or $(NH_4)_2CO_3$ if necessary.

After ageing, the slurry is filtered using a buchner funnel. The loaded support is washed 3 times by stirring in 100 ml of water for 10 min at room temperature. The first wash is combined with the initial filtrate, acidified with 10 ml HCl and 10 ml HNO_3, and the volume recorded. A sample is set aside for elemental analysis via AAS. The 2nd and 3rd washes are discarded, and the loaded support is dried at 120°C in static air for 12 hours.

Modified DP 2 (MDP-2)

MDP-2 is identical to MDP-1, except that the pH is allowed to drift during the ageing period, after the drop-wise addition of Au solution at constant pH is complete.

6.2.2 Calcination of $Au(OH)_3$/Support

When loaded supports are calcined, this is done according to the procedure detailed in §6.1.3.

6.3 Data Work-Up

6.3.1 Deposition-Precipitation Process & Au Content of Au/ZnO

6.3.1.1 Au Content of Au/MO

The Au content of the Au/ZnO material after drying at 120°C for 12 hours in static air is determined via AAS analysis. A sample of measured mass is appropriately digested (§7.1), diluted to a known volume, and analysed via AAS.

$$Au\ Content\ of\ Au/ZnO,\ wt\ \% = \frac{Total\ Mass\ of\ Au\ Detected\ in\ AAS\ Sample}{Total\ Mass\ of\ Solid\ Catalyst\ Digested\ for\ AAS\ Sample} \times 100\%$$

Thus

$$Au\ Content\ of\ Au/ZnO,\ wt\ \% = \frac{c_{sample} \times v_{sample} \times M_{Au}}{m_{Au/ZnO,digested}} \times 100\%$$

$c_{Au,sample}$	measured concentration of Au in diluted sample, mol.dm^{-3}
v_{sample}	total volume of diluted sample, dm^{3}
M_{Au}	atomic mass of element Au, 196.97 g.mol^{-1}
$m_{Au/ZnO,digested}$	measured mass of Au/ZnO catalyst material digested, g

6.3.1.2 Analysis of Liquid Filtrate

The initial liquid filtrate and, in some cases, the combined initial filtrate and wash water (in either case referred to as *the filtrate*), is analysed for Au and Zn content via AAS.

$c_{Me,filtrate}$	measured concentration of Me in the filtrate, mol.dm^{-3}
$v_{filtrate}$	volume of (combined) filtrate, dm^{3}

6.3.1.3 Unloaded Au in Filtrate

Here the total amount of unloaded gold that still remains in solution at the end of the ageing period (in other words the gold that has not precipitated out in some form onto the surface of the support) is calculated from the recorded volume of, and the measured concentration of Au in, the filtrate and presented as a fraction of the total amount of gold introduced in the sample preparation procedure.

$n_{Au,introduced}$	amount of gold introduced in the form of $HAuCl_4$, mol

$$Unloaded\ Au\ in\ Filtrate,\ \% = \frac{Amount\ of\ Au\ Detected\ in\ Filtrate}{Amount\ of\ Au\ Introduced} \times 100\%$$

$$Unloaded\ Au\ in\ Filtrate,\% = \frac{c_{Au,filtrate} \times v_{filtrate}}{n_{Au,\text{int}roduced}} \times 100\%$$

6.3.1.4 Extent of Support Dissolution

The degree of ZnO support dissolution is calculated directly from the Zn concentration of the filtrate.

$$Extent\ of\ Support\ Dissolution,\% = \frac{Total\ Mass\ of\ ZnO\ Dissolved\ in\ Filtrate}{Total\ Mass\ of\ ZnO\ Introduced} \times 100\%$$

$$Extent\ of\ Support\ Dissolution,\% = \frac{c_{Zn,filtrate} \times v_{filtrate} \times M_{ZnO}}{m_{ZnO,\text{int}roduced}} \times 100\%$$

M_{ZnO}	formula mass of ZnO
$m_{ZnO,Introduded}$	total mass of ZnO introduced

6.3.1.5 Au Mass Balance

The Au mass-balance across the DP process is determined by comparing the total amount of gold introduced to the sum of that detected in the waste filtrate and that calculated to be successfully deposited on the support by the end of the ageing period. A term corresponding to the difference is included to balance.

$$Au\ Introduced = Au\ in\ Liquid\ Filtrate + Au\ in\ Solid\ Catalyst + Au\ Difference$$

Au in Filtrate is effectively *Unloaded Au in Filtrate* expressed as a total mass of gold, instead of as a fraction of the total introduced.

The calculation of *Au in Catalyst* assumes the total mass of undissolved ZnO support as having been successfully loaded with gold at the value quantified by the *Au Content of Au/MO*.

$$Total\ Mass\ of\ Undissolved\ ZnO = (100\% - Extent\ of\ Support\ Dissolution) \times m_{ZnO,\text{int}roduced}$$

This approach uses the value of the Zn concentration in the filtrate as determined via AAS to back-calculate the mass of undissolved support actually available as a substrate for gold deposition (as opposed to using the actual mass of loaded support recovered) since, in practice, it proved difficult to retain all the solid material across the numerous filtering and washing stages of the synthesis, such that the amount of loaded catalyst actually recovered is considered to be an underestimate.

Since $Au\ Content\ of\ Au/ZnO, wt\ \% = \frac{m_{Au}}{m_{Au} + m_{ZnO}} \times 100\%$,

If $C_{Au,solid} = \frac{Au\ Content\ of\ Au/ZnO}{100\%}$,

then solving for m_{Au} gives $m_{Au} = \frac{C_{Au,solid}}{1 - C_{Au,solid}} \times m_{ZnO}$.

It is now possible to calculate the mass of gold required to load the entire undissolved mass of ZnO at the measured value by setting m_{ZnO} = *Total Mass of Undissolved ZnO.*

$$Au\ in\ Solid\ Catalyst = \frac{C_{Au,solid}}{1 - C_{Au,solid}} \times Total\ Mass\ of\ Undissolved\ ZnO$$

6.3.2 Au Crystallite Size Analysis

Au crystallite size distributions are typically determined by measuring at least 100 crystallites using appropriate software, importing the resulting measurement file into Microsoft Excel, and using the ‘Histogram’ function of the ’Data Analysis Tool-Pack’ to generate a frequency distribution.

Experimental
Materials Characterisation

7

7.1 Elemental (Au, Zn) Composition of Solids and Liquids

The elemental content of solid materials and acidified liquid filtrate samples from DP is determined using atomic absorption spectroscopy (AAS).

Digestion of solid Au/MO samples is performed as follows:

5 ml conc. HCl is added to ~ 0.1 g of dry Au/MO solid in a conical flask, agitating until the MO support has completely dissolved. 5 ml conc. HNO_3 is then added and the flask agitated until dissolution of the gold particles is complete (1-2 mins). This is followed by the addition of 35 ml of water, gently heating with agitation of the flask until vapours are observed. The contents are filtered and transferred to a 50 ml volumetric flask, before diluting to volume.

Acidified filtrate/wash samples are submitted for analysis without further preparation.

Spectral lines at 242.8 nm (Au) and 213.9 nm (Zn) are used for AAS analysis.

7.2 XRD Phase Analysis

XRD patterns were recorded using a Phillips PW3830 x-ray powder diffractometer, operating at (40 kV, 25 mA) using Ni filtered Cu $K\text{-}\alpha_1$ radiation (v = 1.54056 Å) and a scanning rate of $0.2\ ^{\circ}{}_{2\theta}.\text{min}^{-1}$.

Reference patterns are obtained from the software database supplied with the Phillips instrument.

7.3 Thermo-Gravimetric Analysis (TGA)

Thermo-gravimetric data was obtained using a Stanton Redcroft STA-780 Thermal Analyser. Samples of 50 mg are heated at a constant rate of 1°C.min^{-1} in an atmosphere of N_2 flowing at 30 ml.min^{-1}. Instrumental integrity is checked by calibration against $CuSO_4.6H_2O$ dehydration standard.

7.4 N_2 BET Surface Area Determination

N_2 BET surface areas are determined using a Micromeritics Tristar instrument. 2-Stage degassing of the samples is performed in Helium at 90°C for 60 minutes and 300°C for 300 minutes.

7.5 TEM Morphology Analysis

The dry solid sample is suspended in methanol and placed in an ultrasonic bath to ensure complete dispersion. A drop of the suspension is then transferred to a carbon coated copper grid disc and the methanol allowed to evaporate, leaving the solid sample evenly distributed on the disc.

The specific TEM instrument used is a LEO912 operated in Koehler mode at 120 kV. Images are captured with a digital camera, and a reference scale object digitally included in the image.

Digital images are manipulated (typically adjusting only brightness and contrast) using version 1.2.5 of the open-source product GIMP (Wilber and Sons, http://www.gimp.org/).

Measurements are made using version 1.32j of the public domain product ImageJ (Wayne Rasband, National Institutes of Health, USA, http://rsb.info.nih/ij/).

Experimental
WGS Activity Testing

8

8.1 Experimental Apparatus

Catalytic activity measurements are carried out using an isothermal fixed-bed continuous flow reactor apparatus (figure 8.1).

The packed bed reactor is vertically oriented and operated in down-flow mode. Silicon carbide (SiC) is used as a bulk inert packing to promote plug flow and to dilute the catalyst powder sample.

Water is removed from the hot product stream via condensation, with heat being exchanged in two consecutive cooling coils - the first using ambient air and the second circulating water at 2ºC. The condensed product water is collected in a catch pot also held at 2ºC and periodically drained under the action of a 100 kPa pressure-differential.

Reactor pressure is regulated by a diaphragm back pressure regulator situated subsequent to the water knock out section.

A sampling section allows selective GC analysis of either the de-watered product stream or the pre-mixed reference gas (for GC calibration).

8.1.1 Feed Supply

The feed blend is produced using thermal mass flow controllers (Brooks), which are protected from possible contamination by liquid sample build up (as a result of down-stream blockage) by the large (1000 ml) pre reactor guard catch pot.

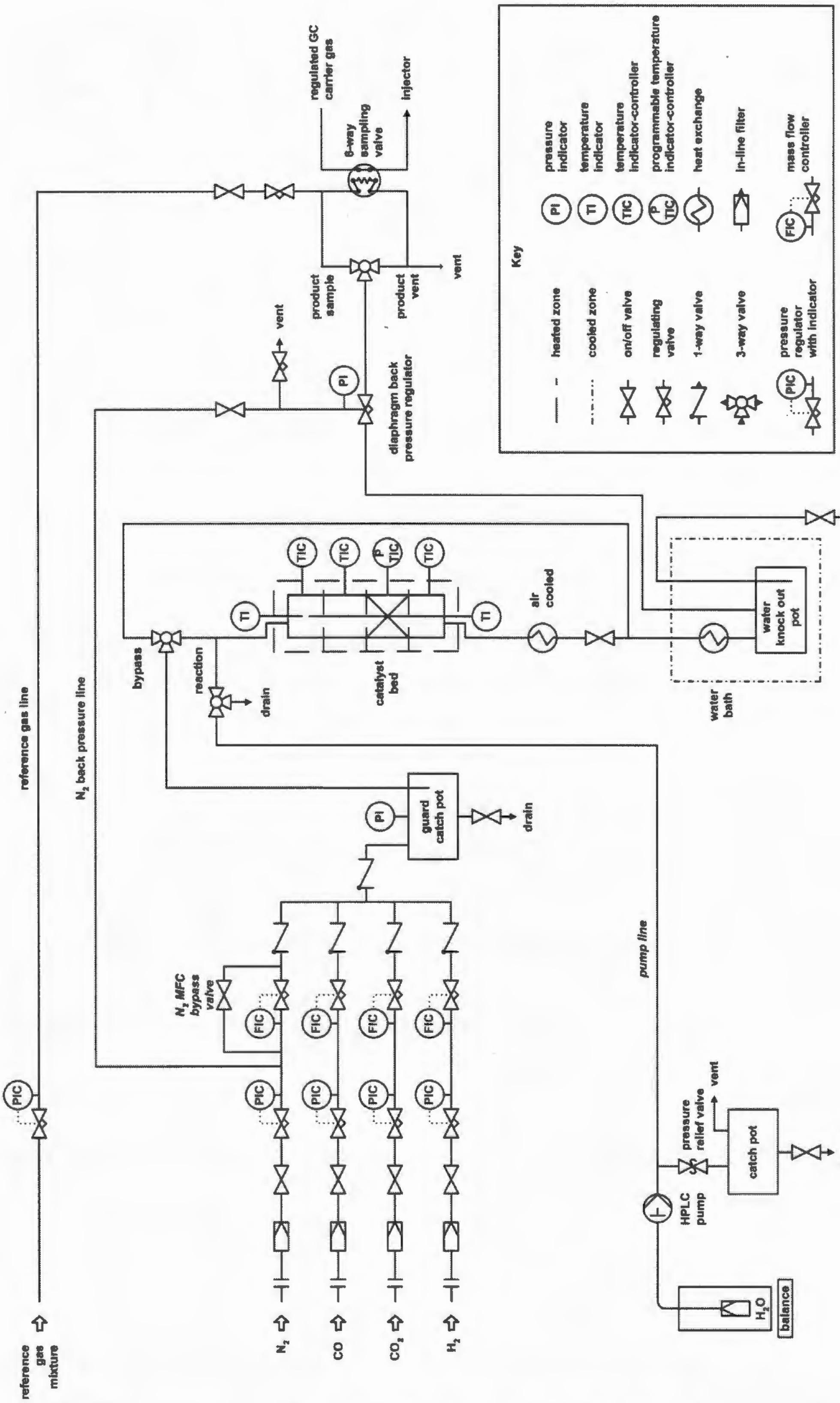

Figure 8.1: Reactor apparatus flow-sheet

De-ionised liquid water at ambient temperature is fed through a filter, from a feed-vessel resting on an electronic balance, by an electronic HPLC pump (SpectraChrom P200 isocratic pump) onto the top of the inert reactor packing where gravity and the dry gas flow draw it down the bed, to be differentially vaporized by the imposed gradual temperature ramp to reaction temperature. The waterfeed vessel is situated on a balance such that monitoring of the vessel mass allows for accurate determination of the water feed rate.

8.1.2 Packed-Bed Reactor

The reactor body comprises a stainless steel tube (internal diameter of 16 mm) with an axial thermowell that houses a free moving thermocouple used to measure the temperature profile of the catalyst bed.

8.1.3 Temperature Control

The reactor is heated using 4 PID controlled heated zones, with the heating zone enclosing the catalyst bed being programmable. The first 2 heated zones serve as feed preheaters, followed by a single reaction zone and, subsequently, a final reactor trim zone.

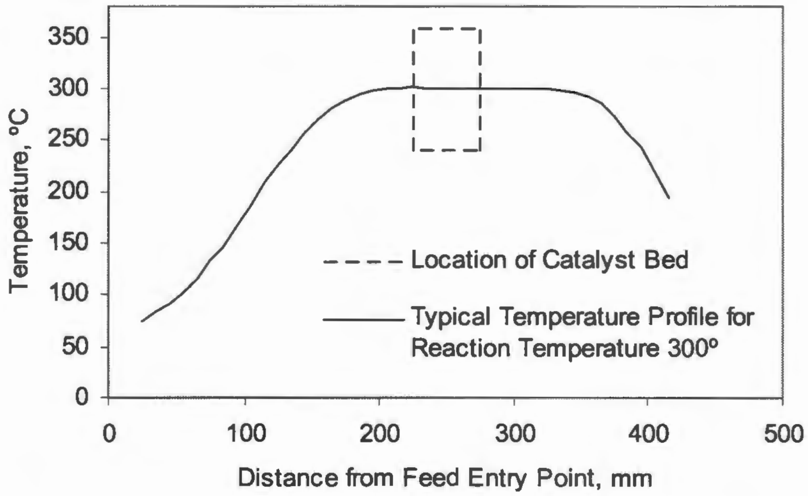

Figure 8.2: A typical reactor temperature profile, this particular one is for a reaction temperature of 300°C. Dotted lines indicate the location of the actual catalyst bed.

8.1.4 Diaphragm Back Pressure Regulator (BPR)

Reaction pressure is set and controlled by the use of a gas dome-loaded diaphragm back pressure regulator situated down stream of the reactor and product water knock-out vessel.

8.1.5 GC Sampling System

The composition of the de-watered product is analysed using gas chromatography (Varian 3400 series GC and Delta 5.0 software from DataWorX for chromatograph integration) and quantified by comparison with a pre-mixed reference gas of known composition (45% H_2, 30% N_2, 5% CO, 15% CO_2, 5% CH_4).

Table 8.1: GC reference (calibration) gas composition

Component	mol. %
H_2	45
N_2	30
CO	5
CO_2	15
CH_4	5

Separation of the component gases is achieved isothermally (at 50°C) using an arrangement of two columns in series, with a bypass facility for the second as shown in figure 8.3. The gaseous sample is first introduced via a 6-way gas sample valve into a 'HayeSep' polymer coated capillary column that separates CO_2 from the other gases (H_2, N_2 and CO), which simultaneously elute first. The H_2, N_2, CO gas mixture is separated by the second molecular sieve ('MolSieve') column, which is switched to bypass just prior to CO_2 eluting off the first column, as CO_2 would adsorb irreversibly on the molecular sieve at the operating temperature of 50°C.

Component detection is firstly via a thermal conductivity detector (TCD) where H_2, N_2 and CO concentrations can be non-destructively quantified (the thermal conductivity of CO_2 being too similar to that of the argon carrier gas to render detection feasible under the operating conditions).

Finally, CO and CO_2 in the stream emerging from the TCD are converted to combustible methane in a 'methaniser' unit, and quantified in the flame ionization detector (FID).

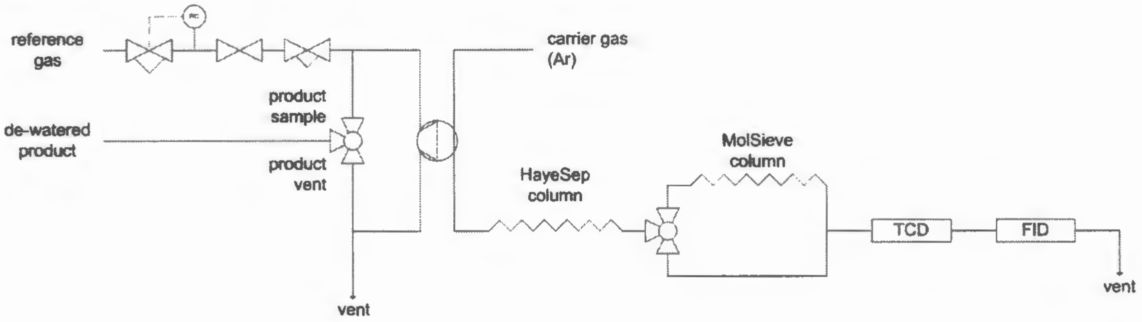

Figure 8.3: Experimental sampling section and abbreviated GC flow-sheet

8.1.5.1 Column Detail

Table 8.2: GC column detail

Reference label		HayeSep	MolSieve
Proprietary Name		HayeSep-N	generic molecular sieve 13X
Manufacturer		VICI	unknown / generic
Capillary or Packed		packed	packed
Coating		divinylbenzene/ ethyleneglycol-dimethylacrylate	no coating (zeolite pore system action)
Diameter (mm)	Outer	3.2	3.2
	Inner	2.2	2.2
Length (m)		2	1.1
Conditioning			Ar, 350°C, 3 hours

8.1.5.2 Methaniser Detail

This in-line unit uses co-fed hydrogen to hydrogenate carbon oxides to methane over a metallic Ni catalyst at 400 °C.

$$CO_2 + 2H_2 \leftrightarrows CH_4 + O_2$$
$$2CO + 4H_2 \leftrightarrows 2CH_4 + O_2$$

The active methanation catalyst is metallic nickel supported on silica pellets (calcined 'diatomaceous earth' / kieselguhr, a high surface area mineral silica, sold by Varian under the proprietary name Chromosorb G. The as supplied catalyst consists of nickel as the nitrate, and is reduced to the metal using hydrogen prior to first use.

8.2 Operating Conditions

8.2.1 Catalyst

1 g of fine (sub 500 µm size fraction) Au/MO catalyst powder is used, and diluted in 10 cm^3 slightly coarser (750 – 500 µm size fraction) inert SiC. The packed bulk density of the sub 500 nm size fraction of ZnO powder was determined to be 0.9 $g.cm^{-3}$.

8.2.2 Reaction Temperature

The reaction temperature is taken to be the average of the temperatures at the beginning, middle and end of the 'isothermal' catalyst bed zone. Typically, these values differed by less than 2°C.

8.2.3 Dry Gas Feed – Composition and Feed Rate

Dry gas is supplied to the reactor at a flow rate of 75 sccm.

Table 8.3: Composition of dry feed gas

	Composition (mol %)	Flow rate (sccm)
CO	5.0	3.8
CO_2	14	11.0
H_2	42	30.9
N_2	39	29.8

This (dry) composition approximately matches that of the model methanol reformer mentioned in §2.3.4 (excluding the water content), while the wet feed flow rate (at a SGHSV of ~ 8000 hr^{-1}) corresponds to typical industrial (dry gas) space velocities.

8.2.4 Liquid Water Feed Flow Rate

Liquid water is introduced to the reactor at a rate of 0.061 $ml.min^{-1}$, which is equimolar with the total dry gas flow. This steam to dry gas ratio of 1 is typical of industrial conditions. At lower steam to dry gas ratios, carbon is typically laid down on the catalyst surface, while operation at higher ratios limits the minimum operating temperature due to higher dew-point temperature of the feed mixture.

8.2.5 GC Operating Temperature

GC operation is isothermal at 50 °C.

8.3 Operating Procedures

8.3.1 Catalyst Loading Procedure (sub 500 µm size fraction)

The lower exit line of the reactor body is plugged with silane treated glass wool and the reactor packed with ascending layers of pure SiC, SiC (10 cm^3) homogeneously mixed with solid catalyst (1 g, sub 500 µm size fraction) and further layer of pure SiC. The inert, SiC, in all three layers is a fine (750 – 500 µm mesh fraction) granulate.

8.3.2 Catalyst Pretreatment

8.3.2.1 Standard Catalyst Pretreatment (excluding commercial LTS catalyst)

The ambient pressure system is purged with N_2 at 200 sccm for 15 min, followed by increasing the temperature from ambient to 400°C at a rate of $4°C.min^{-1}$.

8.3.2.2 Reduction of Commercial LTS Catalyst

The respective MFCs are set for a flow of 2% H_2 in N_2, at a total flow-rate of 216 sccm, and the system left for 1 hour to stabilise. The catalyst bed is subsequently ramped from ambient temperature to 200°C at a rate of $1°C.min^{-1}$ and held there for 16 hours. Finally, the feed is switched to 100% H_2 for 2 hours.

8.3.3 Start-Up Procedure

After having followed either the standard catalyst pretreatment (in the case of any of the gold containing catalysts; in which case the reaction zone temperature would be 400°C) or the recommended reduction for the commercial $Cu/ZnO/Al_2O_3$ catalyst (in which case the reaction zone temperature would be 200°C), the ambient pressure reactor is isolated and bypassed by ensuring that the on/off valve on the water inlet line is closed, toggling the 3-way valve on the gas inlet to bypass and switching the on-off valve on the reactor exit to closed.

The gas feed is set for the standard feed conditions of 5% CO, 14 % CO_2, 42 % H_2 and 39 % N_2, and the system left for 18 hours (overnight) to stabilise.

The reference pressure on the back-pressure regulator is set and the reactor pressure allowed to equilibrate – the completion of this process being confirmed when the full flow of gas is registered at a flow indicator connected to the vent (typically after about 30 mins).

With the 3-way valve on the *pump line* adjacent to the reactor set to drain and the on-off valve on the *drain line* open, the HPLC pump's action is primed for 1 minute and switched to the desired (pre-set) flow rate (of 0.06 $ml.min^{-1}$). The 3-way valve on the *pump line* is set to the reactor and a water flow introduced into the otherwise isolated reactor.

After introducing the water flow into the reactor, the on-off valve on the reactor exit is opened and the 3-way valve on the gas inlet switched from bypass to the reactor, bringing the reactor and catalyst fully on-stream.

8.3.4 GC Sampling of De-watered Product

The GC-FID analysis is calibrated by sampling the reference gas prior to the start of each run. A typical (temperature, conversion) data point is obtained from two sets of readings an hour apart, each set of readings being composed of 5 consecutive dry product gas analyses. After the second set has been taken, the water in the knock-out pot is drained.

The on-off valve on the *reference gas line* is checked to be closed, and the 3-way valve adjacent to the 6-way sampling valve set to *product sample*.

The default position for the 6-way GC sample valve, which is mounted on- and controlled by- the GC, is with the sample loop in-line with the product vent line. To sample the plug of de-watered product gas occupying the sample loop, a GC programmed pneumatic relay switches the sample loop in-line with the GC column for 30 seconds, before returning it to the default (initial) position in-line with the product vent line.

When the automated sampling sequence is engaged and the sample loop switched in-line with the GC carrier gas, both columns are in-line, with the molsieve being bypassed only from 2:00 min onwards, as by this time H_2, N_2, and CO have completely eluted from the second column. The second column is switched out to prevent the strong adsorption of CO_2 onto the second column (molecular sieve), which would otherwise have to be baked out after each run.

8.3.5 Shut-down Procedure

The catalyst is allowed to settle at 300°C for 24 hrs under standard wet feed conditions, and the system pressure reduced to ambient by depressurizing the dome loaded back pressure regulator, followed by a switch to 100 % N_2 dry gas feed at the standard flow rate for 2 hours prior to terminating the water feed. After a further 1 hour all heating to the reaction zone is discontinued and the catalyst is allowed to slowly return to ambient temperature under flowing dry N_2, at which time the reactor is disconnected form the system and the catalyst separated from the inert packing by sieving.

8.4 Data Treatment

8.4.1 (GC) Quantification of Gaseous Components

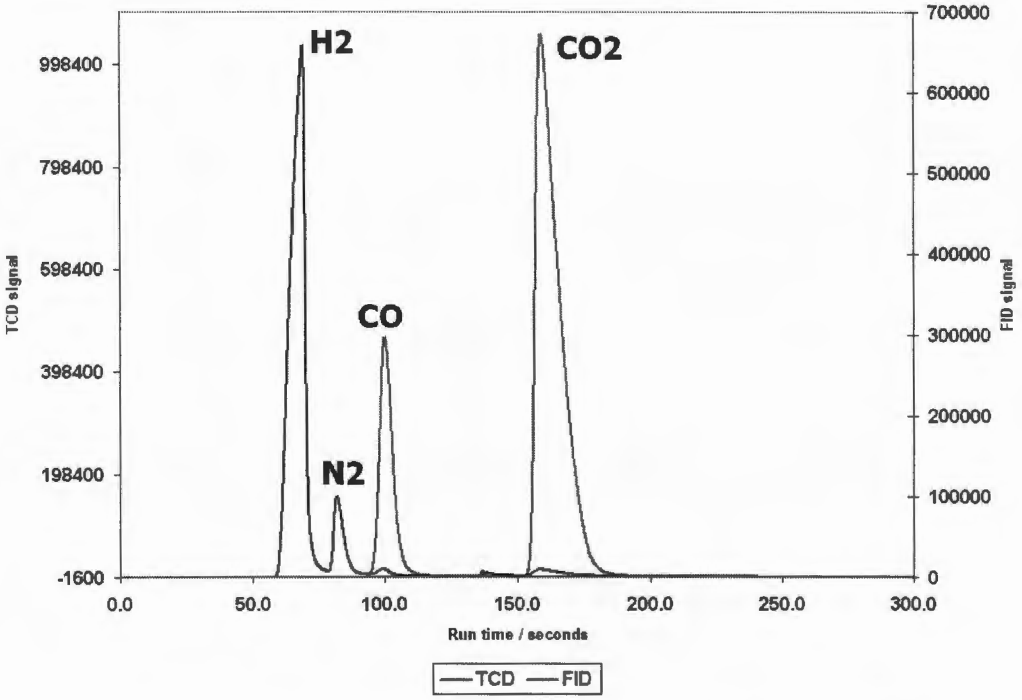

Figure 8.4: Typical chromatogram for a (H_2, N_2, CO, CO_2) gas mixture
TCD (H_2, N_2, CO, CO_2) and FID (CO, CO_2) responses superimposed

8.4.1.1 Linearity of Detector Response

The linearity of detector (FID, TCD) response with analyte concentration was rigorously examined. Below is given a typical assessment, where the 4 components in a CO, CO_2, H_2, N_2 mixture were systematically varied across concentration ranges of interest, the peak area of components recorded and plotted against their respective concentrations.

Table 8.4: Data points for linearity of GC detector response assessment

Component	Mole fraction (%)						
CO	1.7	4	6	9	11	13	15
CO_2	17	15	13	10	8	6	3.72
H_2	25	31	36	42	47	52	57
N_2	56	50	45	40	34	29	25
Total flow rate (sccm)	108	110	112	114	116	118	120

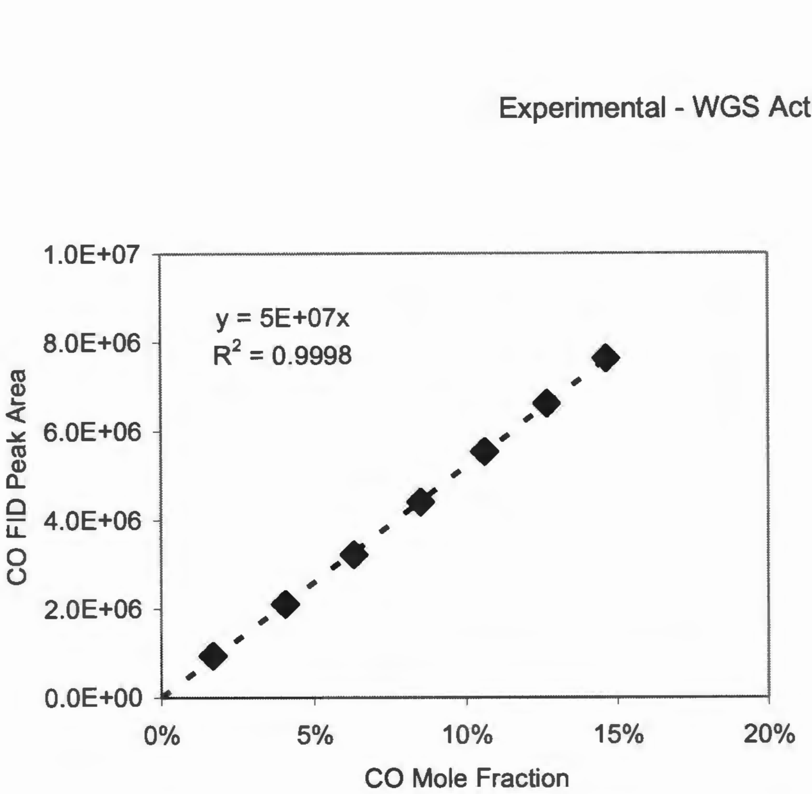

Figure 8.5: FID CO peak area response to concentration

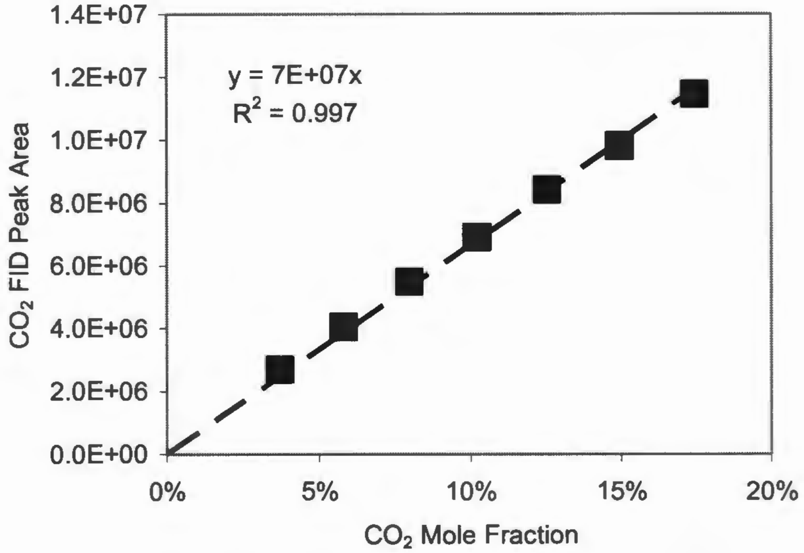

Figure 8.6: FID CO_2 peak area response to concentration

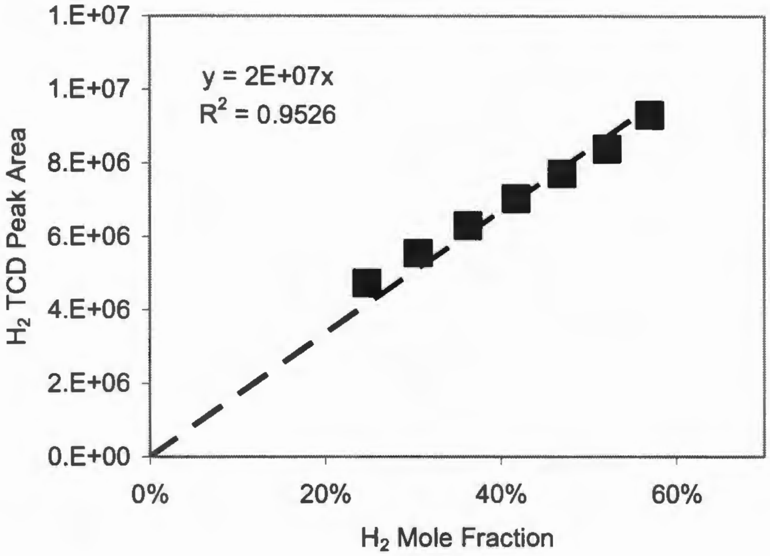

Figure 8.7: TCD H_2 peak area response to concentration

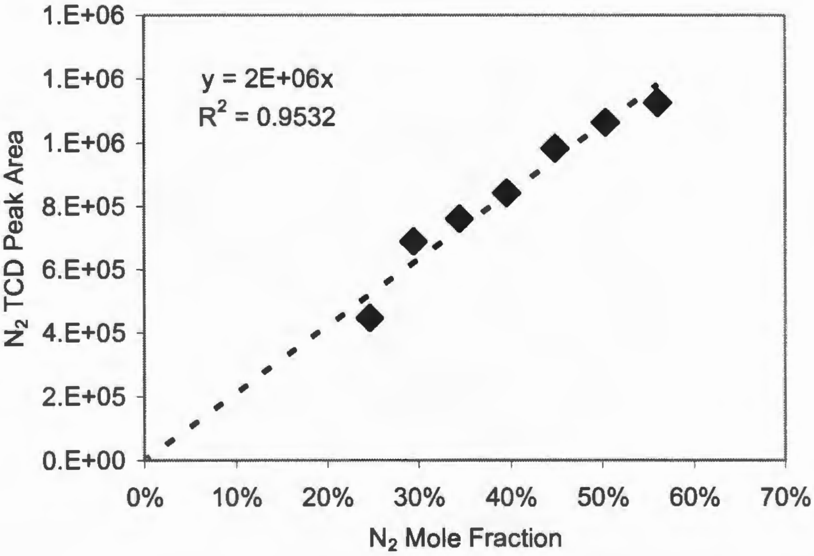

Figure 8.8: TCD N_2 peak area response to concentration

8.4.1.2 Product Composition via Comparison with Calibration Mixture

The concentration of any particular gaseous component is determined by comparison of the peak area registered at the detector (FID) to that of a reference gas of known composition (45% H_2, 30% N_2, 5% CO, 5% CH_4, 15% CO_2) sampled at the same pressure. In other words a 1-point calibration is performed and the linearity of response assumed based on the aforementioned linear calibration charts compiled in the range of concentrations of interest. It must be noted that while a peak corresponding to methane was clearly observable in the FID response when a sample of the pre-mixed reference was injected, no such peak was ever detected in the reaction product of any catalyst tested.

The mole fraction ($x_{i,prouduct}$) of a particular component i in the product can then be trivially calculated from its FID peak area $A_{i,product}$ and that of the reference gas $A_{i,reference}$ of known composition $x_{i,reference}$, a as follows.

$$x_{i,product} = A_{i,product} \times \frac{x_{i,reference}}{A_{i,reference}}$$

Finally, a closed mass balance is assumed, and the individual value then normalized in conjunction with the other components - in order to compensate for small variations in sample size and pressure drop.

8.4.2 Calculation of CO Conversion

CO conversion is calculated from the concentration of CO in the de-watered exit stream (as measured via GC), together with known respective concentrations of CO and CO_2 in the feed, and assuming complete reactive selectivity towards WGS products, as follows

$$X_{CO} = \frac{F_{CO,feed} - F_{CO,product}}{F_{CO,feed}} \times 100\%$$

$F_{COx,stream}$	molar flow rate of CO_x in the dry basis *stream*, mol.s^{-1}
$x_{COx,stream}$	mole fraction of CO_x in the dry basis *stream*

and putting in terms of known or solvable quantities

$$X_{CO} = \frac{x_{CO,feed}.F_{dry,feed} - x_{CO,product}\,.\,F_{dry,product}}{x_{CO,feed}.F_{dry,feed}} \times 100\%$$

where, to correct for water consumed and consequent H_2 produced during the reaction

$$F_{dry,product} = F_{dry,feed} + F_{dry,feed}.x_{CO,feed}.X_{CO}$$

and finally

$$X_{CO} = \frac{1 - \dfrac{x_{CO,product}}{x_{CO,feed}}}{1 + x_{CO,product}}$$

such that conversion is determined directly from the *CO* in the respective feed and product streams, values directly obtained via GC analysis of the dried exit stream during sampling.

8.4.3 Calculation of the Molar Rate of CO Conversion

This is defined as the number of mols of CO converted per second per mol gold.

$$k = \frac{F_{dry,feed}.x_{CO,feed}.X_{CO}}{n_{Au,Au/MO}}$$

$n_{Au,Au/MO}$ number of moles of gold in sample tested, mol

Parameters and constants used in the calculation of reaction rate are presented in table 8.5.

Table 8.5: Parameters & constants used in the calculation of reaction rates

Total vol. flow rate of dry gas @ STP	75	ml
Mole fraction of CO in dry feed gas	5	%
Molar volume of CO @ STP	22.4	$dm^3.mol^{-1}$
Molar flow rate of CO	2.79E-6	$mol.s^{-1}$
Total mass of catalyst	1	g

8.4.4 Calculation of Rate of CO Conversion per m^2 Au Surface Area

The rate of CO conversion per unit gold surface area is calculated by regarding the gold crystallites as regular hemispheres with a diameter corresponding to the average gold crystallite size of the actual population measured by TEM.

Rate of CO conversion per unit of exposed Au surface area
= (Molar rate of CO conversion) / (Total exposed SA of Au in catalyst bed)

Total exposed SA of Au in catalyst bed
= $\sum SA_{Au,exposed}$
= (Total no. Au crystallites in catalyst bed) * (Exposed SA area of single Au crystallite)

Total no. of (hemispherical) Au crystallites in catalyst bed
= $\#_{hemi}$
= (Total mass of Au in catalyst bed) / (Mass of individual hemispherical Au crystallite)

Total mass of Au in catalyst bed
= $\sum m_{Au}$
= (Total mass of catalyst in bed) * (% Mass loading of catalyst)
= $\sum m_{catalyst} * c_{Au}$

Mass of individual hemispherical Au crystallite
= m_{hemi}
= (Volume of individual gold hemisphere) * (Density of gold)

Volume of individual gold hemisphere
= V_{hemi}
= ½ * (Volume of sphere)
= $½ * 4/3.\pi.r_{hemi}^3$
= $2/3.\pi.r_{hemi}^3$

Density of gold
= ρ_{Au}

$= 19.32\ g.cm^{-3}$

$= 1.932 \times 10^{7}\ g.m^{-3}$

$\therefore\ m_{hemi}$

$= \rho_{Au} * 2/3.\pi.r_{hemi}^{3}$

$\therefore\ \#_{hemi}$

$= (\sum m_{catalyst} * c_{Au}) / (\rho_{Au} * 2/3.\pi.r_{hemi}^{3})$

Exposed SA area of single hemispherical Au crystallite

$= A_{hemi}$

$= (½ * \text{SA of sphere})$

$= ½ * 4.\pi.r_{hemi}^{2}$

$= 2.\pi.r_{hemi}^{2}$

$\sum SA_{Au,exposed}$

$= [(\sum m_{catalyst} * c_{Au}) / (\rho_{Au} * 2/3.\pi.r_{hemi}^{3})] * 2.\pi.r_{hemi}^{2}$

$= 3.\sum m_{catalyst}.c_{Au}.\rho_{Au}^{-1}.r_{hemi}^{-1}$

Rate of CO conversion per unit of exposed Au surface area

$= (\text{Molar rate of CO conversion}) * 1/3.\rho_{Au}.r_{hemi}.\ \sum m_{catalyst}^{-1}.c_{Au}^{-1}$

$r_{hemi} = 1/2d_{hemi}$

$\therefore$ Rate of CO conversion per unit of exposed Au surface area

$= (\text{Molar rate of CO conversion}) * 1/6.\rho_{Au}.d_{hemi}.\sum m_{catalyst}^{-1}.c_{Au}^{-1}$

Preliminary Findings

9

9.1 Materials Synthesis

9.1.1 ZnO Support Synthesis

Drop-wise addition of $Zn(NO_3)_2$ solution to a saturated solution of Na_2CO_3 successfully precipitates a white solution which - after washing, drying at 120°C in static air overnight, and crushing to a powder - exhibits an XRD pattern (figure 9.1) corresponding to crystalline $Zn_5(OH)_6(CO_3)_2$.

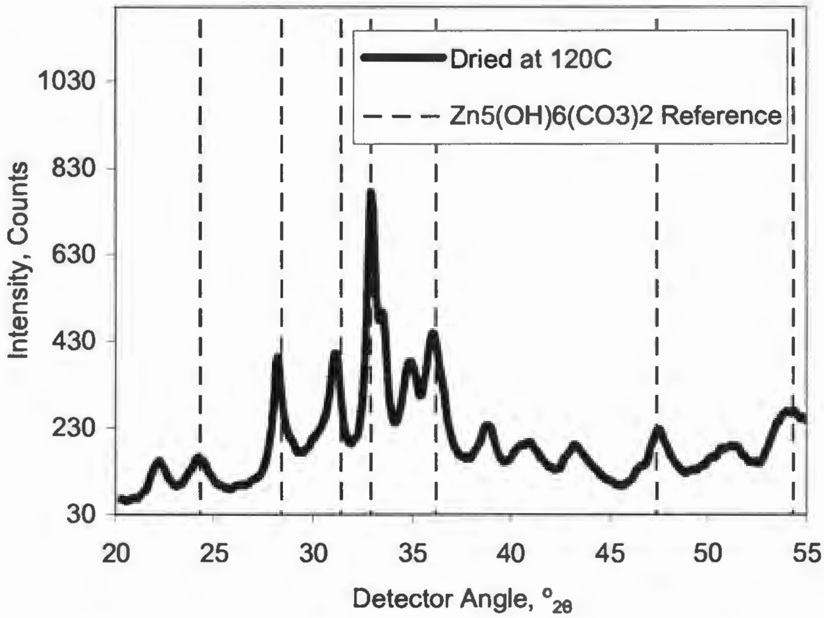

Figure 9.1: XRD pattern of synthesised $Zn_5(OH)_6(CO_3)_2$ after washing and drying at 120°C. (Dashed lines indicate the location of the seven most intense peaks in the reference spectrum for $Zn_5(OH)_6(CO_3)_2$ in the range)

Fluidised bed calcination of $Zn_5(CO_3)_2(OH)_6$ in air for 12 hours at 400°C produces a material with an XRD pattern matching ZnO (figure 9.2), and a BET surface area around 30 $m^2.g^{-1}$.

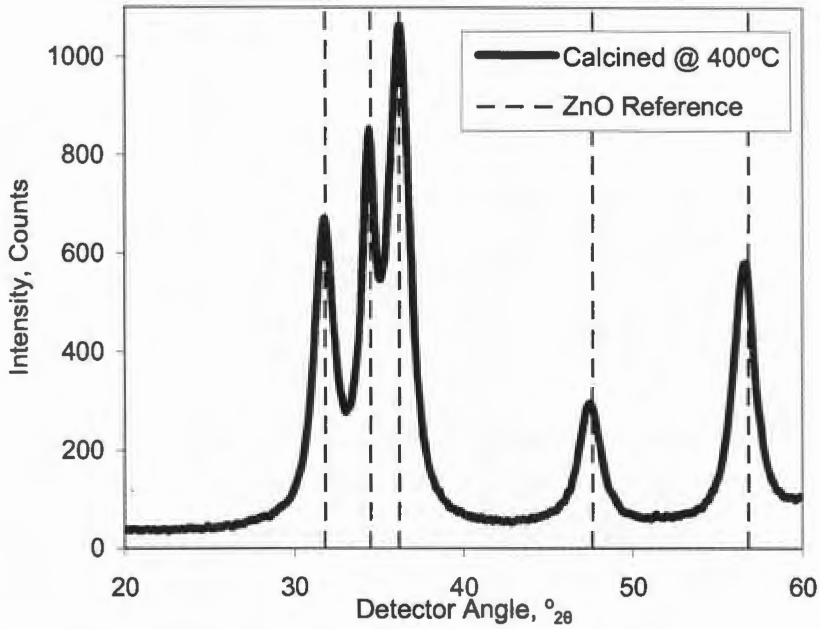

Figure 9.2: XRD pattern for synthesised ZnO material after calcinations in air at 400°C.

Dashed lines indicate the location of the five most intense peaks in the ZnO reference spectrum in the detector angle range measured.

In order to further investigate the nature of this thermal decomposition, thermo-gravimetric analysis of a sample of $Zn_5(OH)_6(CO_3)_2$ was performed. This entailed applying a constant heating rate to small sample situated on a gravimetric balance in flowing air.

Sample decomposition becomes appreciable at temperatures above ~ 200°C, with the maximum rate of decomposition being observed at a temperature of ~ 245°C (figure 9.3). This value corresponds closely to the report by Wang *et al.* (2003) that heating to a temperature of 240°C was required to produce a material that was identical to ZnO on an XRD pattern comparison basis.

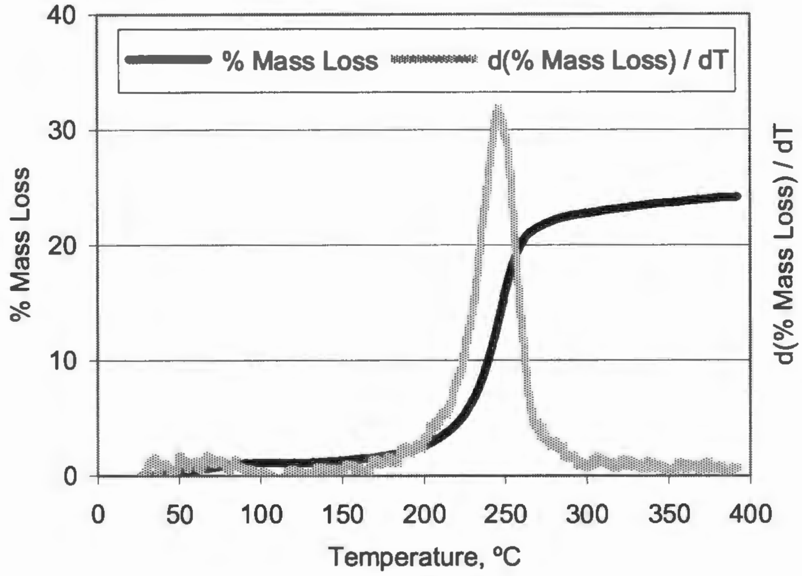

Figure 9.3: TGA of synthesised $Zn_5(OH)_6(CO_3)_2$

9.1.2 XRD Analysis of Gold Transformation During Calcination

MDP1 was used to synthesize ~ 5 wt % Au/ZnO, with the wet material being dried first at room temperature (using anhydrous silica gel and a sealed desiccator), then at 120°C in static air overnight (~ 16 hours). XRD patterns of the material after the each of the 2 successive drying stages were recorded, and are presented in figure 9.4.

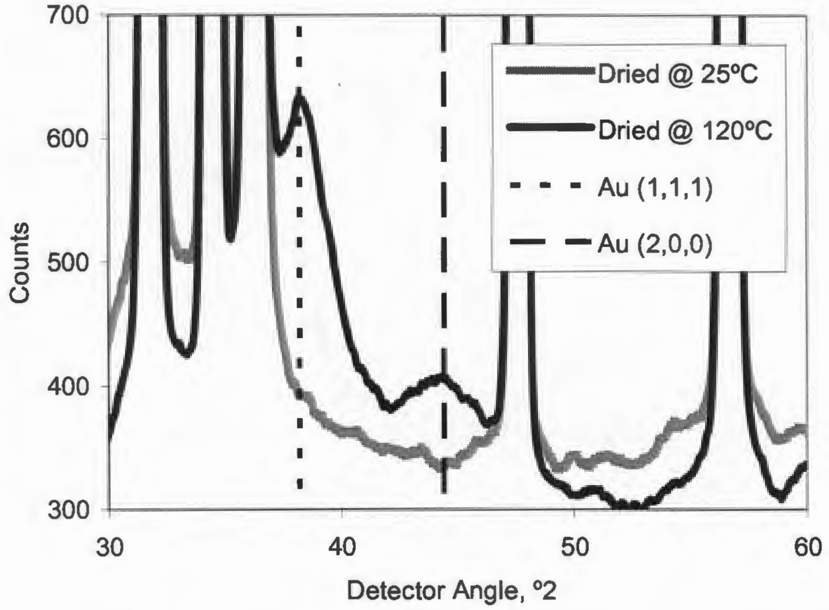

Figure 9.4: XRD pattern for material prepared using MDP1 -
after precipitation and drying at ambient T (25°C, $Au(OH)_3/ZnO$; grey line),
and after drying at elevated temperature (120°C, Au/MO; solid line)

Peaks corresponding to metallic gold are clearly evident in the pattern of the material dried at 120°C, but are wholly absent in the pattern of the material dried at ambient temperature. Two possible explanations exist for this observed difference: either metallic gold is already present after drying at ambient temperature, but the gold crystallites are so small as to be undetectable, or gold is present in an oxidised state in the sample dried at ambient temperature, and is reduced during the drying at elevated temperature.

9.1.3 Gold Crystallite Morphology

Approximately three types of gold crystallite morphologies were repeatedly observed in Au/ZnO samples examined using TEM: flat-top angled slabs, angular polyhedrons and rounded hemispherical particles.

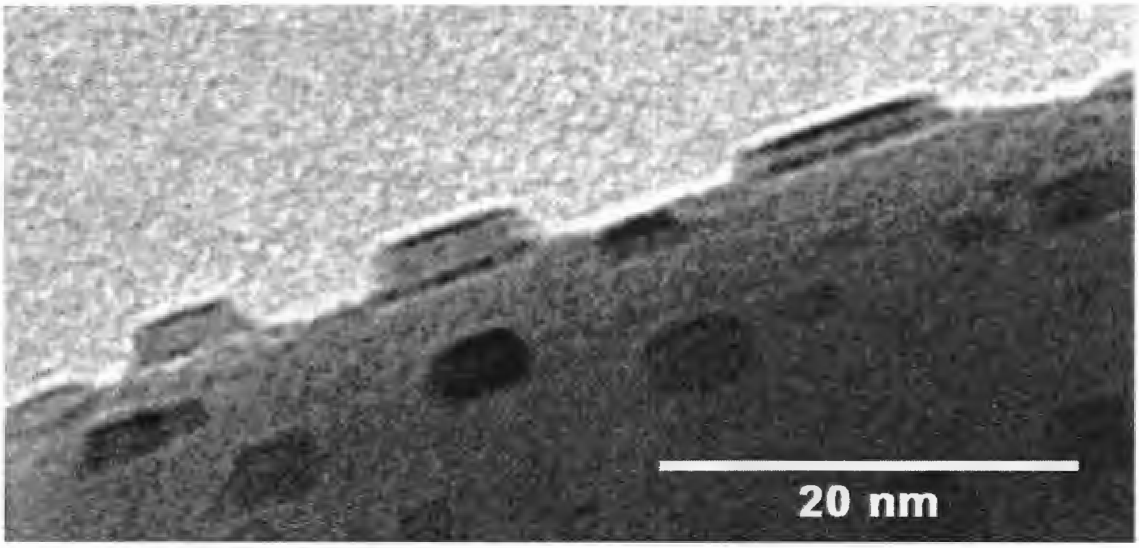

Figure 9.5: Flat-topped angular slabs

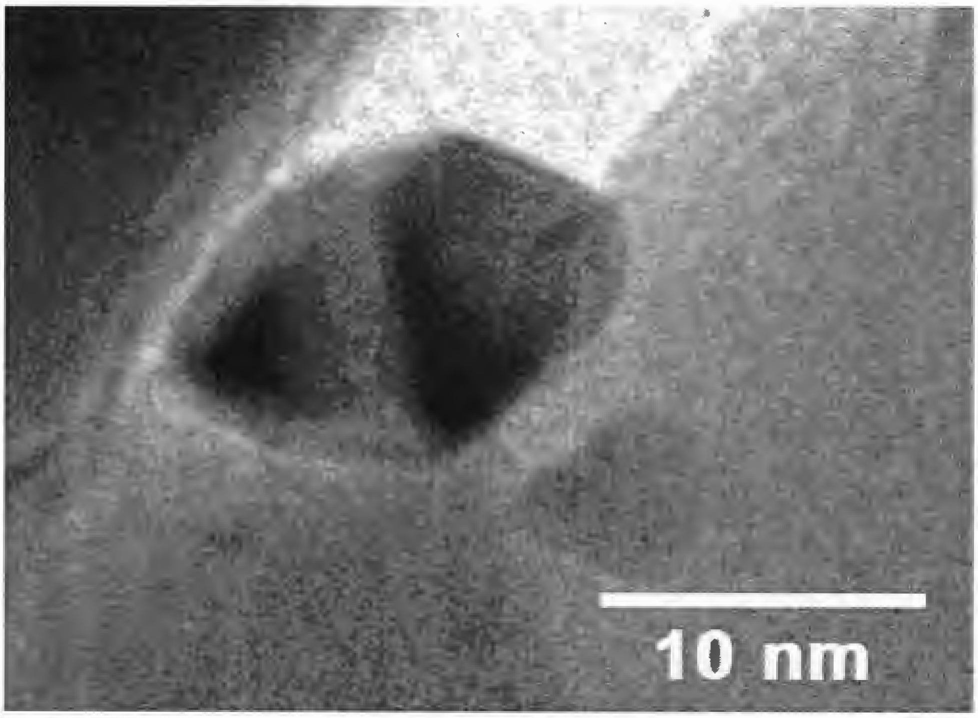

Figure 9.6: Angular polyhedron

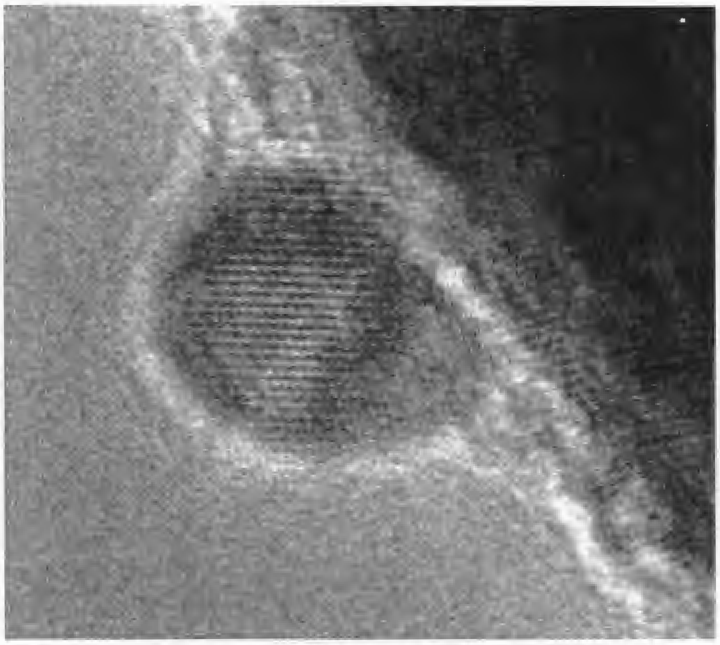

Figure 9.7: Angular polyhedron

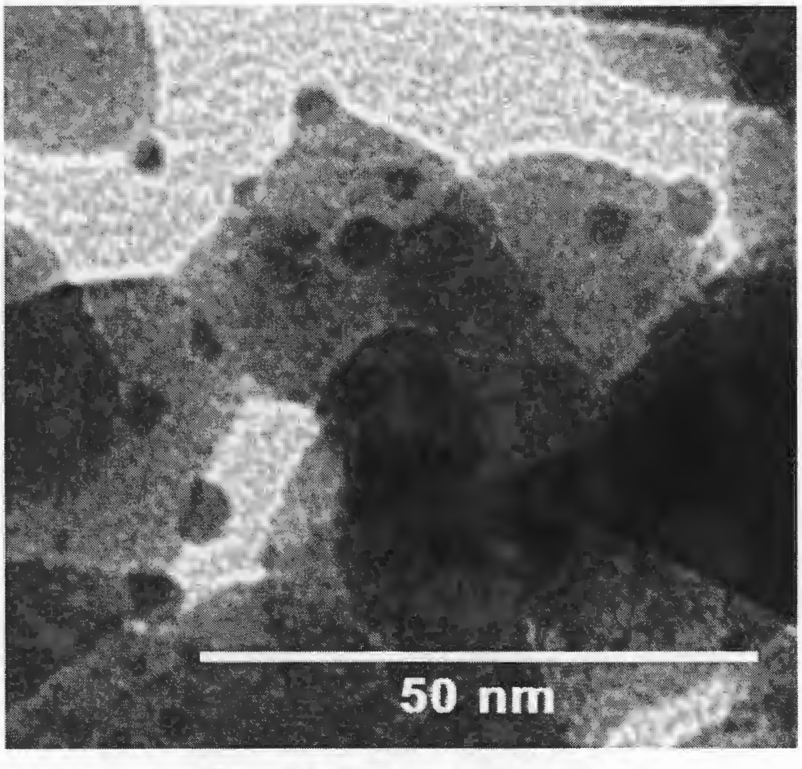

Figure 9.8: Rounded hemispheres

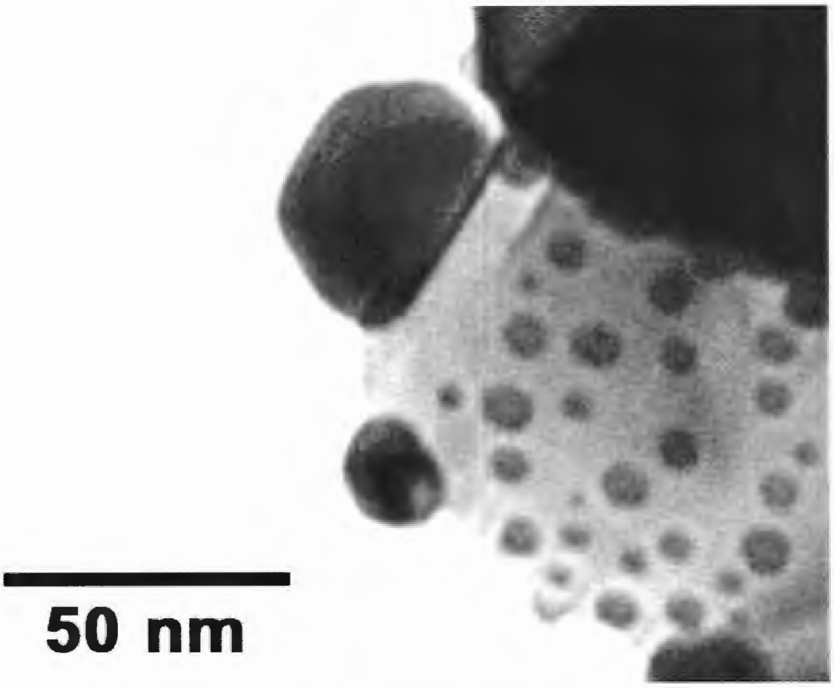

Figure 9.9: Rounded hemispheres

The polyhedral morphology is consistent with the literature, e.g. Mohr *et al.* (2003) report well-faceted (cubo-octahedral) polyehedral gold crystallites for Au/ZnO (prepared via impregnation of ZnO with $HAuCl_4$ followed by drying in static air at 110°C for 12 h and reduction in flowing hydrogen at 300°C for 2 h). There is evidence that the specific support determines the gold crystallite morphology, e.g. Claus *et al.* (2004) report more rounded, less clearly faceted gold crystallites for Au/TiO_2, Au/ZrO_2 and Au/SiO_2. Okazawa *et al.* (2006) report slab-like gold crystallites at low gold coverages and rounded hemispherical ones at higher coverages on stoichiometric TiO_2.

No clear correlation between gold crystallite morphology and preparation method could be discerned.

9.2 Materials Activity

9.2.1 T @ X_{CO} = 20 % Materials Activity Ranking

Table 9.1: Summarised WGS activity data - T @ X_{CO} = 20% basis

Rank	MO	Description	Synth. Method	IB Me	Au (wt %)	BET SA ($m^2.g^{-1}$)	d_{Au} (nm)	$T_{X=20\%}$ (°C)
1	ZnO/Al_2O_3	Süd-Chemie	Other Coprecip.	Cu	33.6	-	-	142
2	TiO_2	WGC Ref.	Other DP	Au	1.5	52	3.8	218
3	ZnO	ex hydrozincite	MDP2	Au	1.7	33	6	324
4	ZnO	Synthetic	MDP2	Au	4.1	30	4.4	375
5	ZnO	Synthetic	MDP2	Au	5.7	33	4.6	399
6	ZnO	Synthetic	MDP2	Au	1.9	30	3.7	414
7	ZnO	SAARChem	MDP2	Au	1.3	3.6	-	< 433
8	ZnO	Synthetic	n/a	-	0	44.3	n/a	>
9	ZnO	SAARChem	n/a	-	0	3.6	n/a	>

Results & Discussion

10

Attention is now drawn now to some trends in the data generated, which is presented in complete form (without additional commentary) in appendices 13 (gold deposition process data), 14 (gold crystallite size data) and 15 (tabulated WGS activity data).

10.1 Materials Synthesis

The chosen starting point to achieving the overall objective of developing a potentially commercially viable wet-chemistry synthesis of catalytically active Au/ZnO is the canonical DP method of Tsubota et al. (1995).

10.1.1 Canonical Deposition-Precipitation Method of Tsubota *et al.* (1995) - DP

This synthesis process corresponds to the following series of events: formation of a slurry of the support at 70°C; addition of concentrated $HAuCl_4$ solution; immediate pH adjustment with Na_2CO_3 to the appropriate value; maintenance of constant pH and temperature across a 1 hour ageing period; separation of solid from solution by filtration, repeated washing with deionised water; drying of the filter cake in static air at 120°C.

From theory, the efficiency of gold transfer from solution to support should be determined primarily by the electrostatic potential of the support surface, as this potential should determine the carrying capacity. On this basis (§4.2.1), gold uptake by the support should decrease as the ageing pH approaches the IEPS of the support (~ 9 in the case of ZnO [Parks, 1965]), above which it should load no anionic species.

Indeed, this behaviour is clearly observed, the gold content of (and by inference the degree of gold uptake by) the support decreasing with increasing ageing pH (figure

10.1), and tending to 0 as the ageing pH approaches 9, suggesting that the scenario outlined in §2.3.2.1 may be a fundamentally accurate description of the DP process.

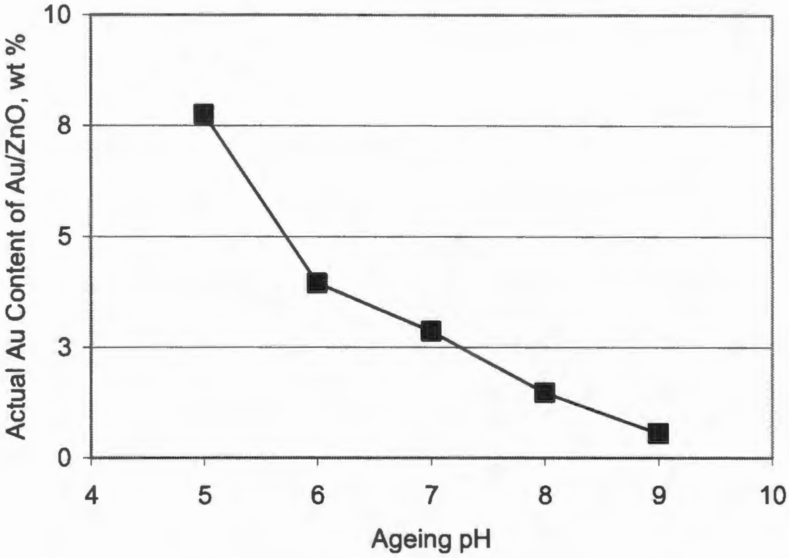

Figure 10.1: Au Content of Au/ZnO
(DP, ZnO BET SA = 3.6 $m^2.g^{-1}$, pH Series)

The next consideration is the extent to which the ageing pH influences the gold crystallite size. Haruta (1997) reports that [for Au/MO materials produced by DP] 'above pH 6 ... the mean particle diameters of Au in the calcined catalysts become smaller than 4 nm' (refer figure 10.2) - a specific note on the generally reported trend of post-calcination Au crystallite size decreasing with increasing ageing pH.

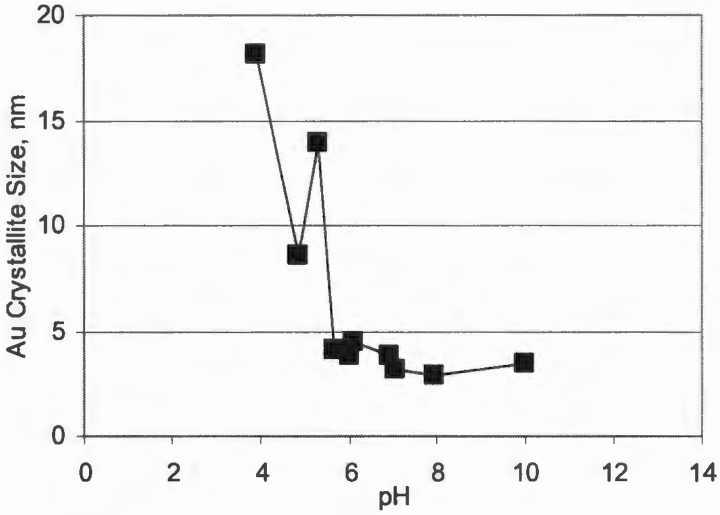

Figure 10.2: Post-calcination gold crystallite size for Au/TiO_2 as a function of DP pH
[100% loading efficiency would produce a 13 wt % material]
(Haruta, 1997)

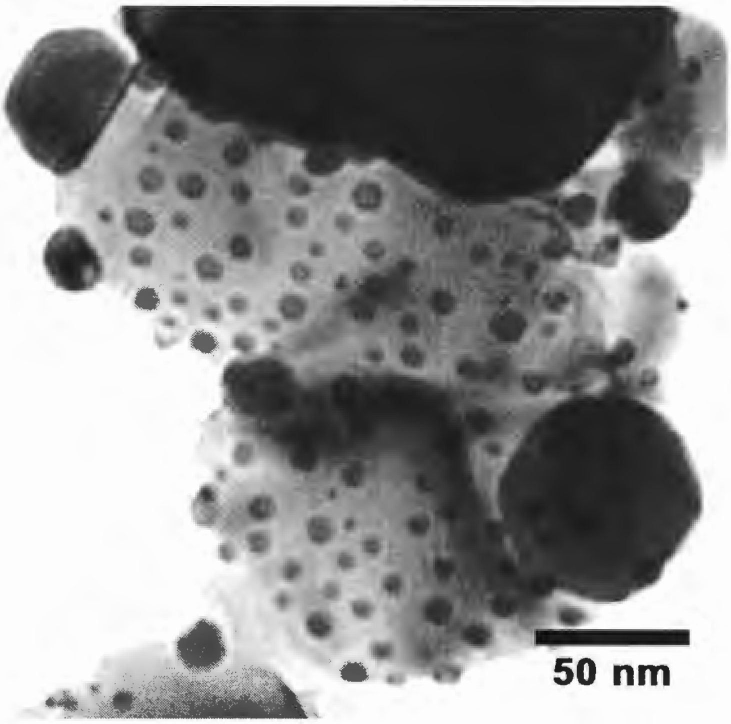

Figure 10.3: Sample TEM image of Au/ZnO (ZnO SA = 3.6 $m^2.g^{-1}$)
DP, pH 5, 7.8 wt % Au, d = 8.0 ± 4.0 nm

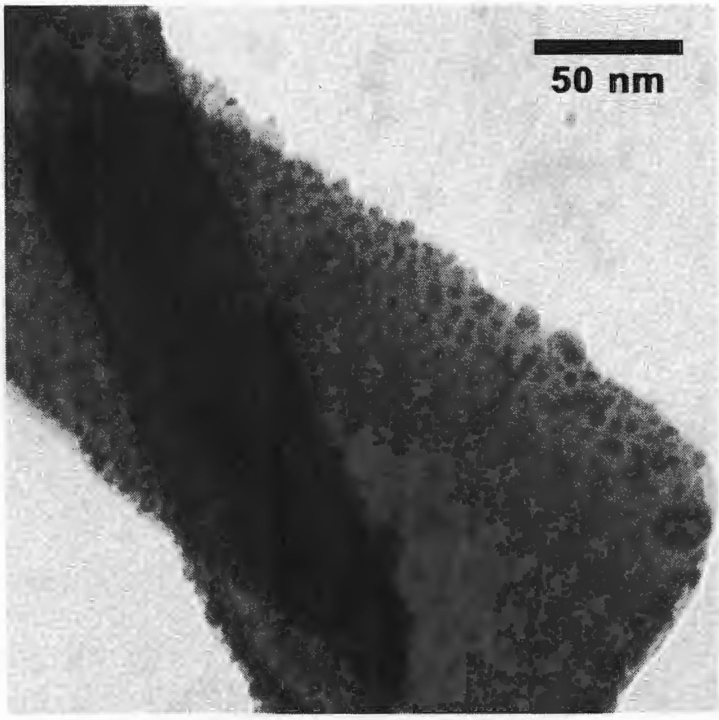

Figure 10.4: Sample TEM image of Au/ZnO (ZnO SA = 3.6 $m^2.g^{-1}$)
DP, pH 7, 2.9 wt % Au, d = 6.9 ± 3.2 nm

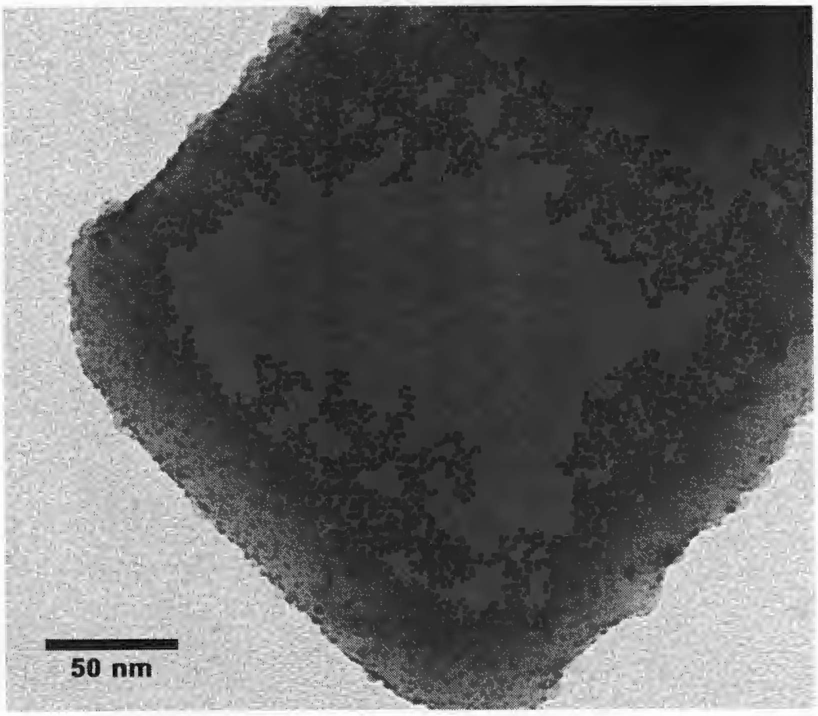

Figure 10.5: Sample TEM image of Au/ZnO (ZnO SA = 3.6 $m^2.g^{-1}$)
DP, pH 8, 1.5 wt % Au, d = 3.4 ± 0.7 nm

TEM examination of the material after DP of gold at 70°C and drying in static air at 120°C (figures 10.3 [pH 5], 10.4 [pH 7], 10.5 [pH 8] – data summarised in table 10.1) reveals qualitative agreement with this trend, average Au crystallite size decreasing with increasing ageing pH (figure 10.6).

Table 10.1: Au crystallite size data for Au/ZnO materials prepared with DP on 3.6 $m^2.g^{-1}$ ZnO

Method	ZnO SA $m^2.g^{-1}$	Source	Type of Series	pH	[Au] *wt %*	d_{avg} *nm*	σ *nm*	n	No of Images
DP	3.6	Commercial	pH	5	7.8	8.0	4.0	310	3
				7	2.9	6.9	3.2	189	3
				8	1.5	3.4	0.7	86	3

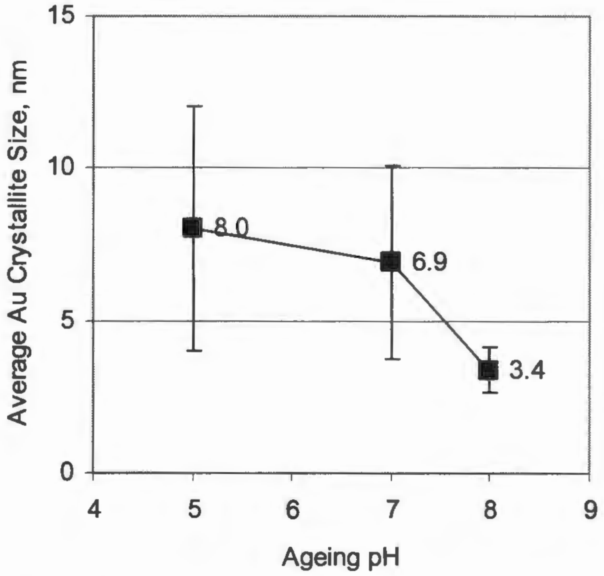

Figure 10.6: Average Au crystallite size as a function of ageing pH
(DP, ZnO SA = 3.6 $m^2.g^{-1}$, pH series)

Unfortunately the data generated does not clarify whether the post-calcination Au crystallite size is directly determined by pH dependant crystallisation dynamics, or by the relative amount of gold on the support surface (figure 10.7) prior to calcination (as suggested by Valden *et al.* (1998); which would imply only an indirect dependence of gold crystallite on ageing pH).

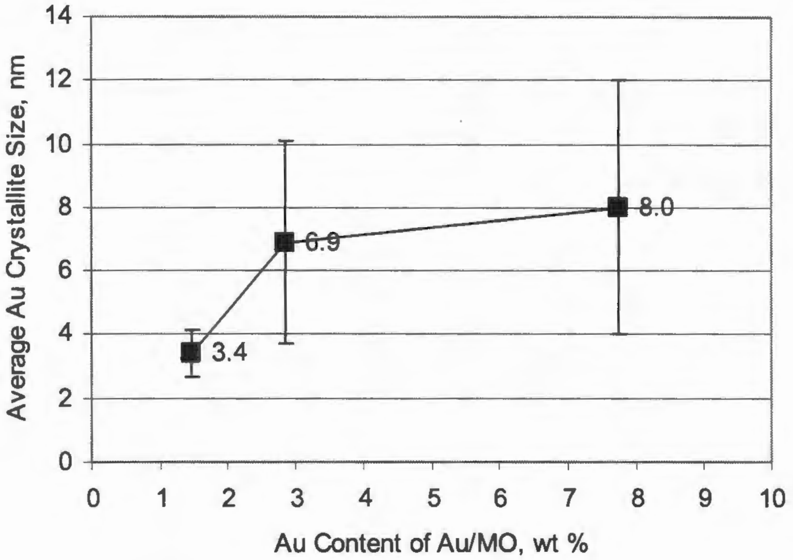

Figure 10.7: Average Au crystallite size as a function of Au content of Au/ZnO (DP, ZnO SA = 3.6 $m^2.g^{-1}$, pH series)

Kung *et al.* (2003) suggest a possible explanation for the apparent pH dependence of post-calcination Au crystallite size. They demonstrate chloride uptake by γ-Al_2O_3 to be pH dependent (figure 10.8) - decreasing with increasing pH, and tending to zero as the IEPS (pH 8 for γ-Al_2O_3 [Parks, 1965]) is approached. Since support associated chloride is known to promote sintering during heat treatment in Au/MO materials (Oh *et al.*, 2002), an indirect pH dependence is possible. [Promotion of sintering of supported copper crystallites by chloride being well known in the case of the commercial Cu/ZnO/Al_2O_3 LTS catalyst (Twigg, 1989) – also a ZnO supported dispersed group IB metal material.]

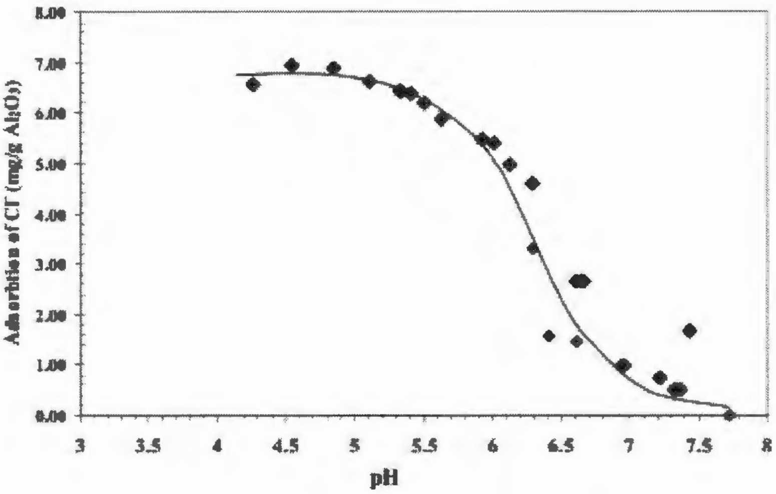

Figure 10.8: Chloride uptake for Au/Al_2O_3 produced by DP as a function of ageing pH (Kung *et al.*, 2003)

While promotion of sintering during heat treatment by residual chlorine may be invoked to explain the increase in average gold crystallite size with decreasing ageing pH, resort to this phenomenon may, to a certain degree, be unnecessary. A very real possibility is that the relative amount of support surface area available for gold deposition may also be a significant factor limiting the formation and stabilisation of small gold crystallites.

Consideration of a TEM image of the sample prepared at pH 8 (figure 10.5), which is loaded with gold at 1.5 wt %, reveals that even at this relatively low gold loading the support surface is effectively covered with gold - although the average gold crystallite is still small at 3.4 nm, and the population narrowly dispersed (σ = 0.7 nm). By 2.9 wt % gold loading - an approximate doubling - the average gold crystallite size has increased to 6.9 nm while the population distribution has broadened (σ = 3.2 nm), both significantly, and this can quite plausibly be linked to simple overloading of the support surface – a supposition intuitively supported by examination of a TEM image of the sample (figure 10.4 being an example). Images (figure 10.3) of the Au/ZnO material with the highest gold loading (7.8 wt % Au, prepared at pH 5) in the series suggest that significant sintering has taken place, with both the largest gold crystallites (d_{Au} = 8.0 nm; also with the broadest distribution [σ = 4.0 nm]) and numerous areas of unloaded support surface being evident.

The decrease in surface coverage with simultaneous increase in average gold crystallite size is consistent with the idea of residual chlorine in samples prepared at more acidic pH promoting sintering. Finally, while the number average gold crystallite size is observed to increase only slightly (from 7 to 8 nm) going from 2.9 wt % Au (pH 7) to 7.8 wt % Au (pH 5), the presence of very large gold crystallites (e.g the gold crystallite in the upper left of figure 10.3, approximately 40 nm in diameter at base) is evident in the sample at 7.8 wt % Au, and these crystallites, while not contributing significantly to the number average (which is compiled only for sub 20 nm gold crystallites), do in fact account for a major fraction of the total gold.

Consequently, it becomes evident that when considering the synthesis of supported small gold crystallites, the carrying capacity of the support must be considered. This can be gauged by considering the mass (or better still number of moles) of gold present per support surface area (figure 10.9 – materials prepared via DP on low SA ZnO).

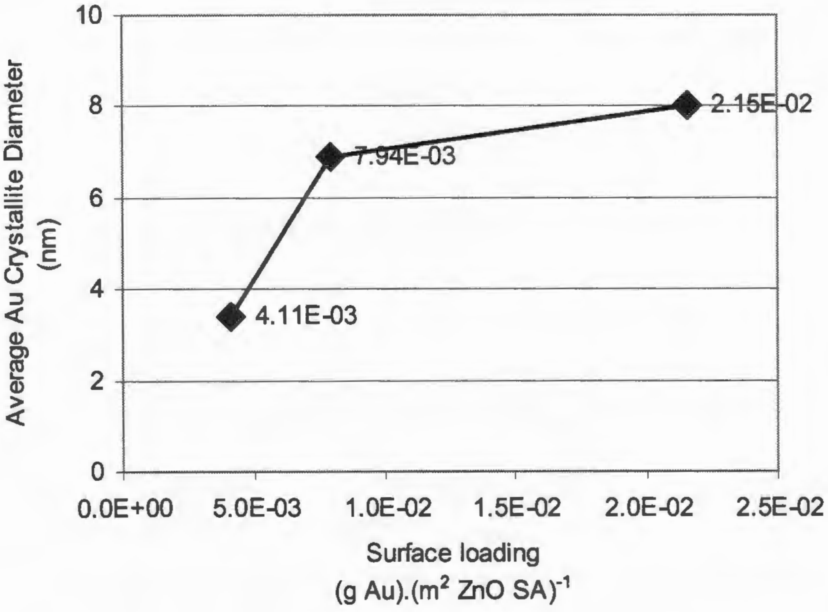

Figure 10.9: d_{Au} as a function of (g Au).(m^2 ZnO SA)$^{-1}$
for Au/ZnO materials prepared on 3.6 $m^2.g^{-1}$ ZnO using DP

Thus, since surface coverage is approximately total for the material loaded with gold at 1.5 wt %, it seems that a reasonable first approximation of the upper limit is around 4 x 10^{-3} (g Au).(m^2 support surface area)$^{-1}$ for small (< 5 nm) gold particles to be maintained.

To summarise the observed features of the canonical DP synthesis: an inherent trade-off exists in that operation at acidic pH maximises gold uptake, but appears to produce large gold crystallites, while operation at basic pH produces requisitely small gold crystallites, but results in poor gold uptake. Furthermore, operation at pH below ~ 6 is unpractical because ZnO support dissolution (figure 10.10) becomes extreme.

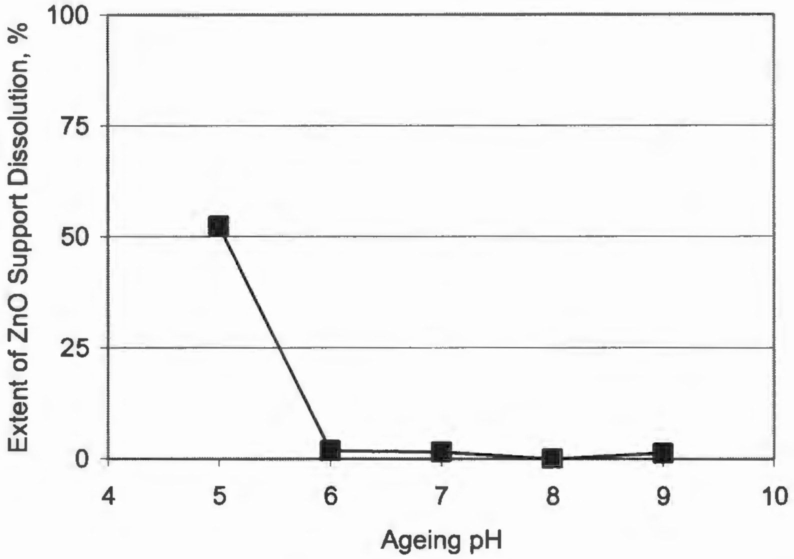

Figure 10.10: Extent of support dissolution
(DP, SAARChem ZnO, pH series)

10.1.2 Modified method of *Fu et al.* (2003b)

To overcome the aforementioned trade-off between degree of gold uptake and Au crystallite size inherent in the DP synthesis, a modified method suggested by the group of Flytzani-Stephanopoulos (for the synthesis of Au/CeO_2) is investigated:

"DP took place by adding the desired amount of $HAuCl_4$ dropwise into aqueous slurry of the prepared ceria. The pH of the aqueous slurry had already been adjusted to the value of 8 using $(NH_4)_2CO_3$. The resulting precipitate was aged at room temperature (RT) for 1 hour. It should be noted that unlike a previously reported DP method [DP, Tsubota *et al.* (1995)] which uses NaOH as the base and excess (about five times) $HAuCl_4$, the present method can deposit the desired gold loading on ceria using the exact amount of $HAuCl_4$ solution." (Fu *et al.*, 2003b)

This method is attractive because it is reported to simultaneously achieve the goals of total gold uptake and post-calcination Au crystallite size of 5 – 6 nm (Fu *et al.*, 2003b). Since it is not clear from the published description whether a constant pH is maintained across the ageing period (practiced here as MDP1), or if the pH is rather allowed to drift (practiced here as MDP2), both alternatives are considered.

10.1.2.1 Constant pH Ageing – MDP1

Considering first the constant pH version (MDP1), the order of events corresponds to: formation of an aqueous slurry of the support (ZnO); addition of $(NH_4)_2CO_3$ or HNO_3 until the appropriate pH value is reached; drop-wise addition of $HAuCl_4$ with simultaneous addition of $(NH_4)_2CO_3$ to maintain constant pH; ageing for 1 hour while maintaining constant pH via addition of further $(NH_4)_2CO_3$ or HNO_3 as necessary; finishing with filtration, washing and drying.

In order to ascertain whether the pH value of 8 suggested for CeO_2 is also optimal for (initially the low surface area) ZnO, the MDP1 method is executed for pH in the range 6 to 9. From figure 10.11, it is clearly evident that maximum (but not yet complete) gold uptake is achieved for pH around 8. That execution of MDP1 at pH 9 (the approximate IEPS of ZnO), while not optimal, still corresponds to uptake of ~ 35% of total gold in solution (as opposed to ~ 10% with DP), while execution at the more acidic pH of 6 results in negligible gold uptake, suggests a far weaker dependence on the IEPS of the support with MDP1 as compared to DP – a potentially useful characteristic.

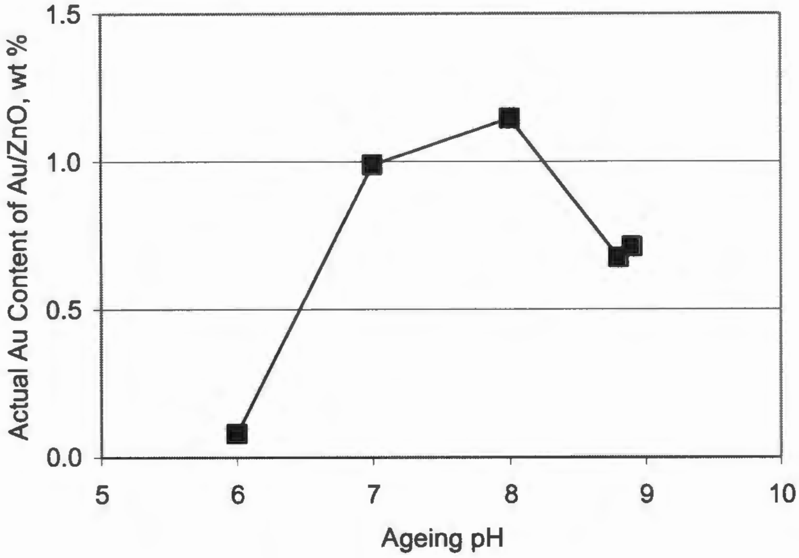

Figure 10.11: MDP1 - Au Content of Au/ZnO as a function of ageing pH
(ZnO SA = 3.6 $m^2.g^{-1}$)

A further advantage of MDP1 over DP is that the pH zone of maximum gold uptake is only slightly basic, limiting support dissolution during loading and ageing (figure 10.12), a substantial improvement over the DP situation.

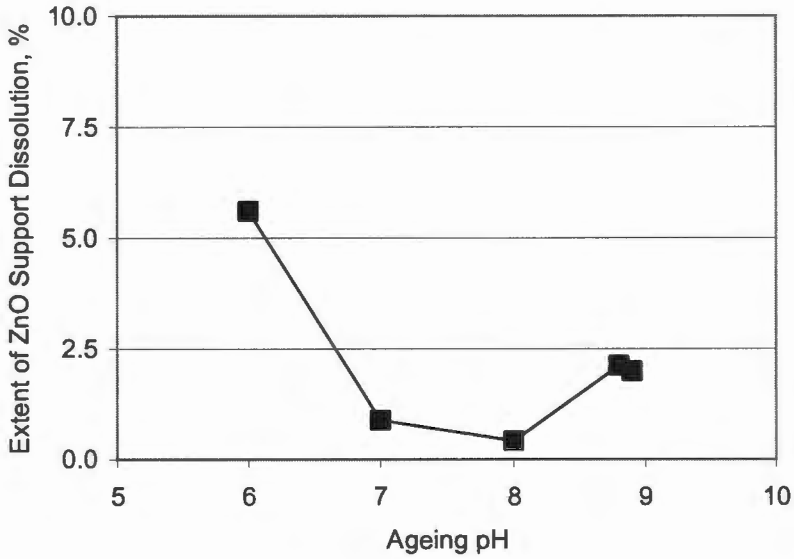

Figure 10.12: MDP1 - Extent of Support Dissolution
(SAARChem ZnO, 3.6 $m^2.g^{-1}$)

TEM examination of the material prepared at pH 8 (1.2 wt % Au) reveals that the average Au crystallite size is 4.8 ± 1.6 nm – only slightly larger and more broadly distributed than the sample prepared at pH 8 (with an analagous gold loading of 1.5 wt % Au) using canonical DP (where the average Au crystallite size was determined to be 3.4 ± 0.7 nm).

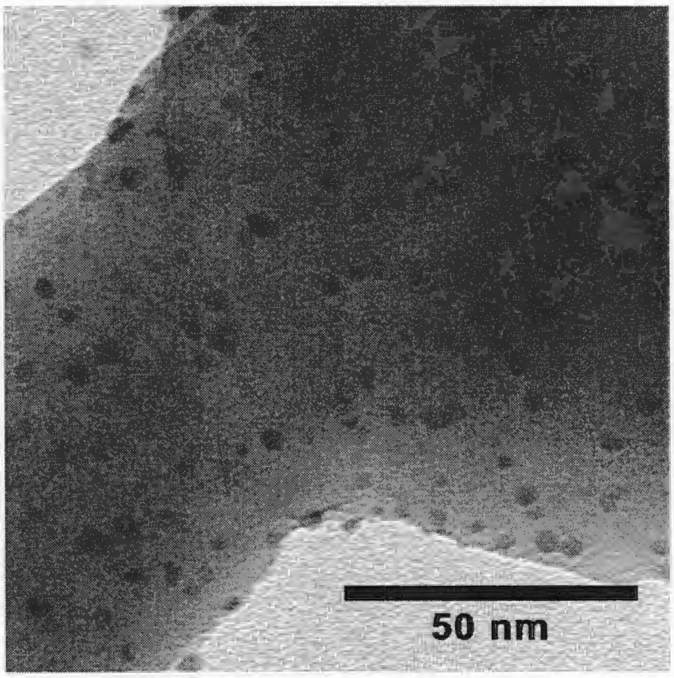

Figure 10.13: Sample TEM image of Au/ZnO material produced at pH 8 using MDP1 and low SA ZnO
(pH series, 1.2 wt % Au, d_{Au} = 4.8 ± 1.6 nm)

Switching to the higher surface area of the novel ZnO support does not appear to influence the degree of gold uptake in MDP1 - with the roughly 10-fold increase in surface area (from 3.6 $m^2.g^{-1}$ [fig. 10.14] to 30 $m^2.g^{-1}$ [fig. 10.15]) effecting approximately 60 % gold uptake regardless of support surface area or loading level.

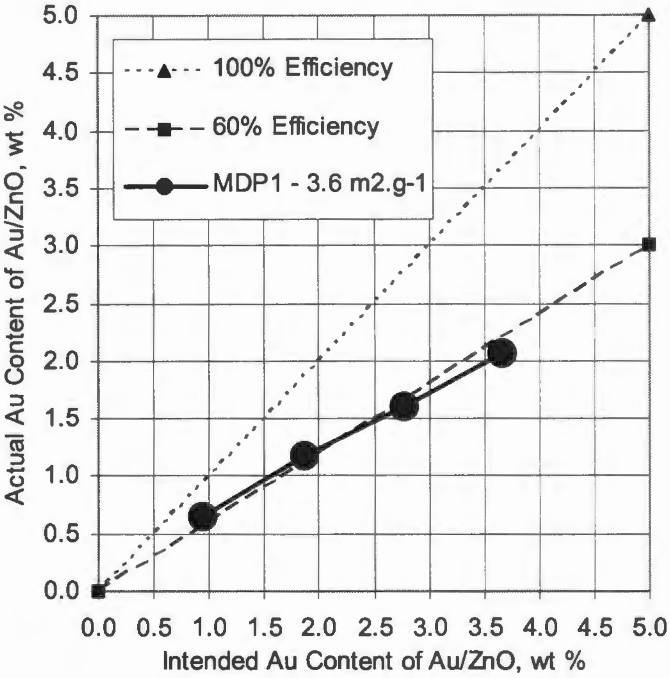

Figure 10.14: MDP1 - Gold uptake by 3.6 $m^2.g^{-1}$ ZnO (Loading series)

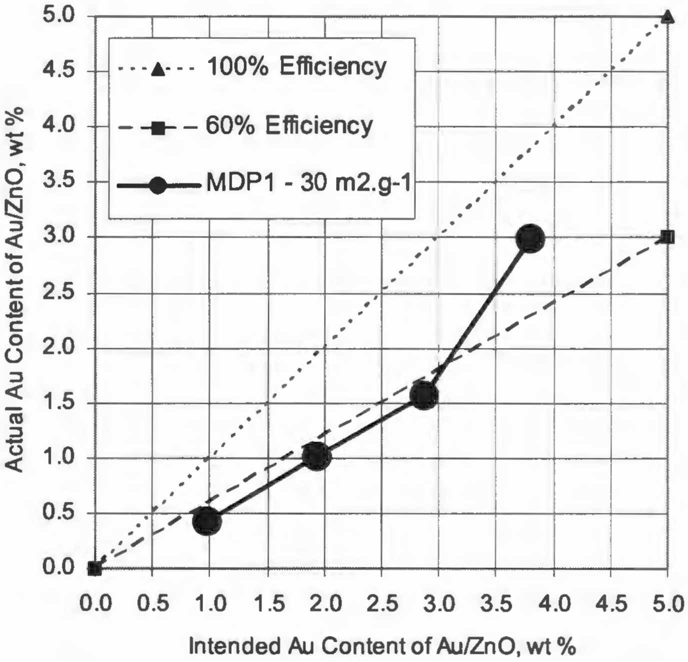

Figure 10.15: MDP1 - Gold uptake by 30 $m^2.g^{-1}$ ZnO (Loading series)

10.1.2.2 Uncontrolled Ageing pH – MDP2

Having assessed the variation of the modified DP method of Fu *et al.* (2006) where the pH is held constant across the ageing period (MDP1), and found it to reproducibly achieve a gold uptake of around 60%, and also gold crystallites around 5 – 6 nm in average size for supports with surface area in the range 4 – 30 $m^2.g^{-1}$, the behaviour of the system when the solution pH across the ageing period is allowed to drift in an uncontrolled fashion rather than being held constant is now assessed. This is done in the hope of improving the degree of gold uptake while retaining the relatively favourable size distribution. Since maximum gold uptake is observed around pH 8 using MDP1, this value is selected for use in the second variation.

The order of events is now: formation of an aqueous slurry of the (ZnO, 30 $m^2.g^{-1}$) support; addition of $(NH_4)_2CO_3$ or HNO_3 until a pH value of 8 is reached; drop-wise addition of $HAuCl_4$ with simultaneous addition of $(NH_4)_2CO_3$ to maintain constant pH; ageing for 1 hour without further intervention with respect to solution pH; followed by filtration, washing and drying. [MDP2]

This variation of the MDP process now clearly achieves the goal of total gold uptake by the support (figure 10.16).

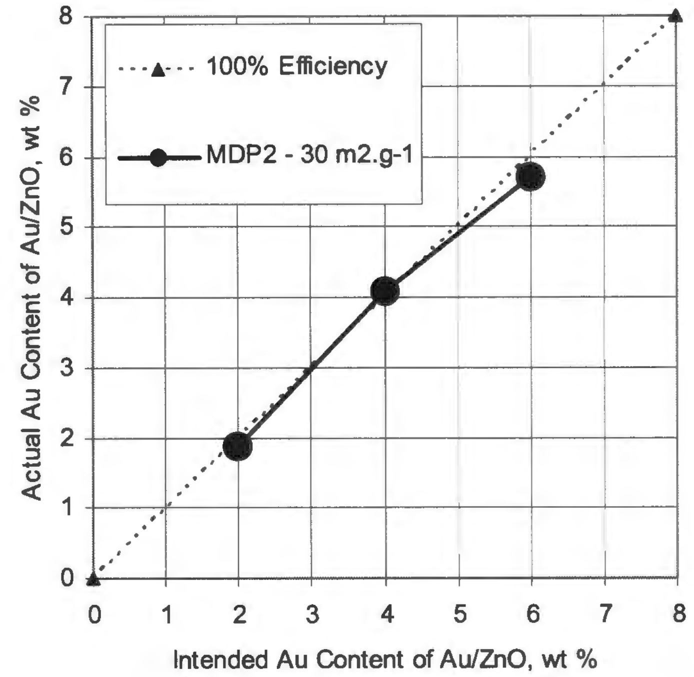

Figure 10.16: MDP2 - Gold uptake by 30 $m^2.g^{-1}$ ZnO
(Loading Series)

Furthermore, the MDP2 variation appears to produce good average Au crystallite sizes with relatively narrow population distributions (3.8 ± 1.5 nm @ 1.9 wt % Au; 4.4 ± 1.7 nm @ 4.1 wt % Au; 4.6 ± 1.7 nm @ 5.7 wt % Au - [table 10.2].

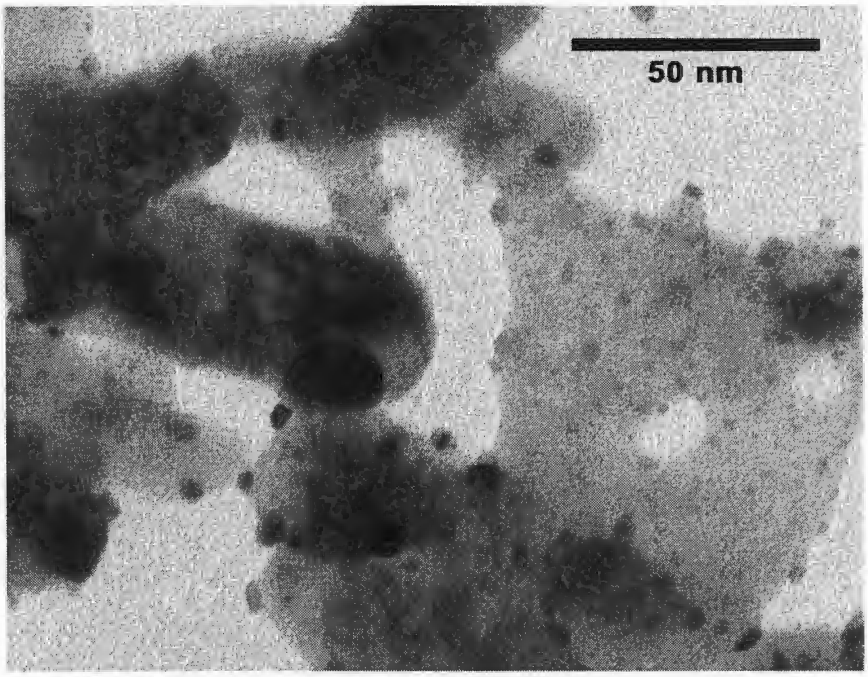

Figure 10.17: Sample TEM image of Au/ZnO (ZnO SA ~ 30 $m^2.g^{-1}$)
MDP2, pH 8, 1.9 wt % Au, d = 3.8 ± 1.5 nm

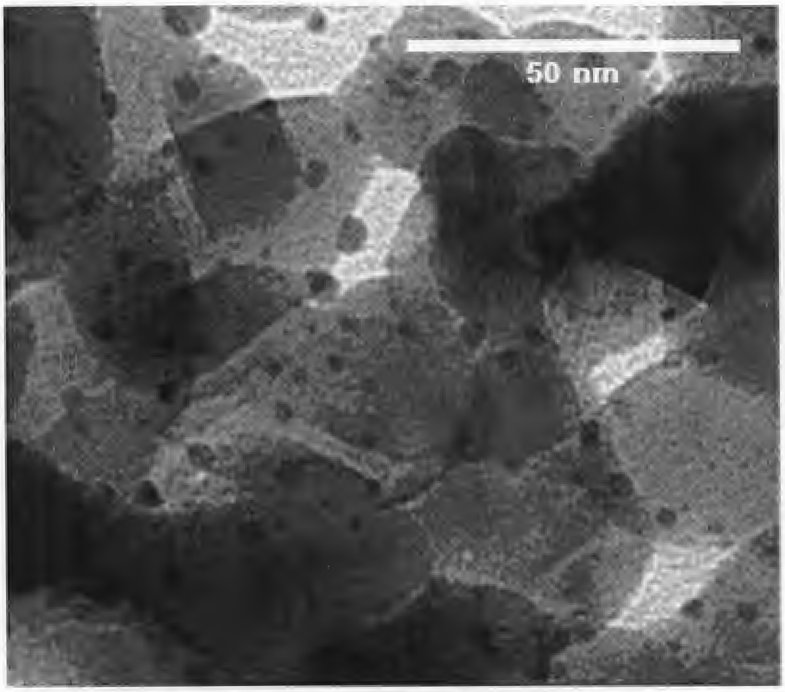

Figure 10.18: Sample TEM image of Au/ZnO (ZnO SA ~ 30 $m^2.g^{-1}$)
MDP2, pH 8, 4.1 wt % Au, d = 4.4 ± 1.7 nm

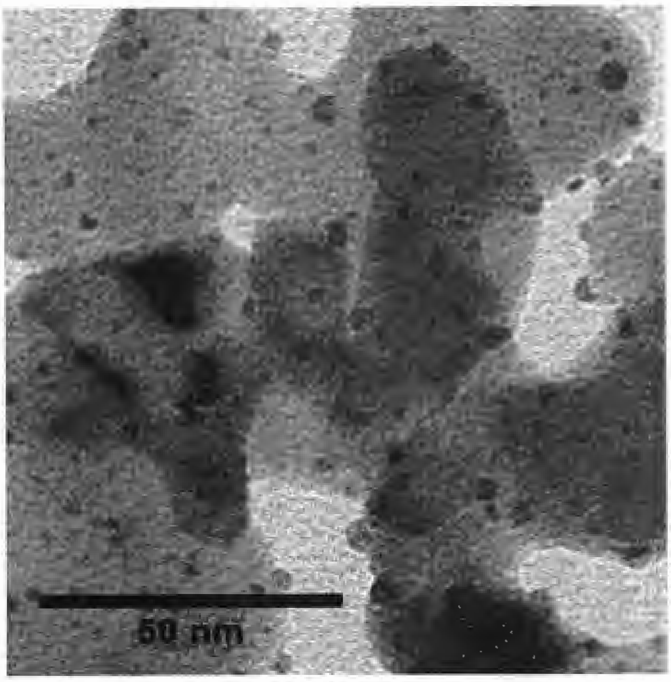

Figure 10.19: Sample TEM image of Au/ZnO (ZnO SA ~ 30 $m^2.g^{-1}$)
MDP2, pH 8, 5.1 wt % Au, d = 4.6 ± 1.7 nm

Table 10.2: Au crystallite size data for Au/ZnO materials prepared with MDP2 on 30 $m^2.g^{-1}$ ZnO

Method	ZnO SA $m^2.g^{-1}$	Source	Type of Series	pH	[Au] *wt %*	d_{avg} *Nm*	σ *nm*	n	No of Images
MDP2	30	Synthetic	Loading	8	1.9	3.8	1.5	352	4
				8	4.1	4.4	1.7	483	3
				8	5.1	4.6	1.7	430	4

Analagous to MDP1 (and DP), average Au crystallite size again appears to increase slightly with increasing gold loading (figure 10.20).

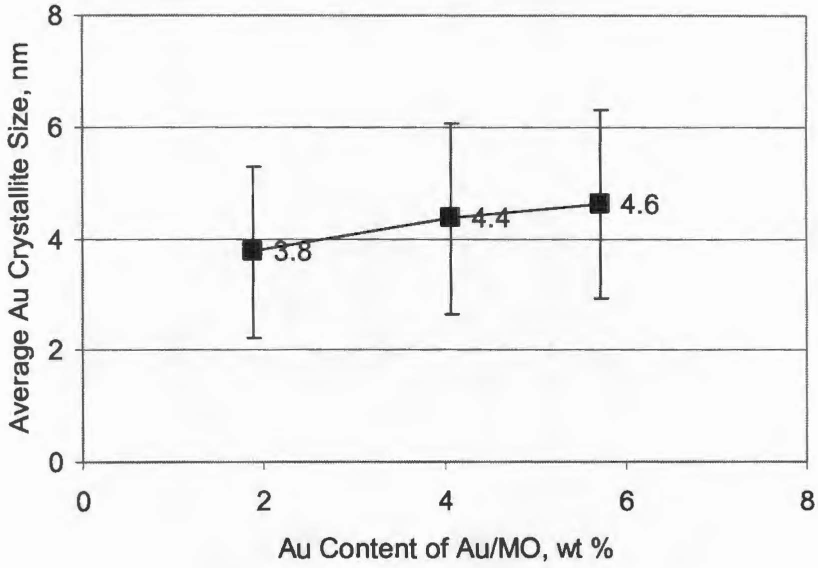

Figure 10.20: Average Au Crystallite Size as a Function of Au Content of Au/ZnO (MDP2, ZnO SA = 30 $m^2.g^{-1}$, loading Series)

10.2 Materials Activity

10.2.1 Novel Materials

Having successfully developed a method (MDP2) of synthesising a relatively narrowly distributed population of requisitely small (~ 5 nm) gold crystallites supported on a metal oxide - with almost complete uptake of the solution-phase precursor gold complex [and a second method (DP) of synthesizing even smaller and more narrowly distributed, but less efficiently loaded dispersed gold materials] - the activity (with respect to catalysing the water-gas shift reaction) of materials prepared by the MDP2 method is considered.

Considering first the activity of the unpromoted ZnO supports: while the lower surface-area (3.6 $m^2.g^{-1}$) ZnO displayed no measurable CO conversion at 400°C or below, the novel higher surface area (44 $m^2.g^{-1}$) material achieved measurable conversion by 350°C - 2% under the specific conditions, or 1.5 x 10^{-9} (mol CO).$m^{-2}.s^{-1}$ – with the rate increasing to 7.3 x 10^{-9} (mol CO).$m^{-2}.s^{-1}$ (or 12 % CO conversion) by 400°C.

The incorporation of gold, corresponding (but not necessarily limited) to small (~ 5 nm) metallic particles strongly bonded to the metal oxide support surface (observable via transmission-electron microscopy) clearly results in the formation of a composite material over which the WGS reaction occurs at a faster rate than the unpromoted support alone.

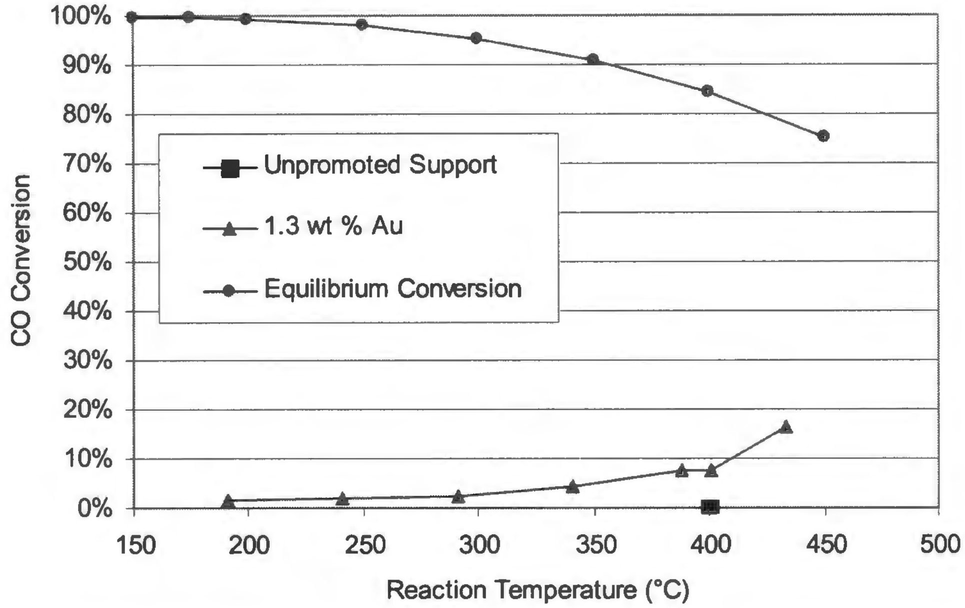

Figure 10.21: Promotion of WGS activity in 3.6 m^2.g^{-1} ZnO by gold

In the case of materials based on the lower surface area commercial ZnO, the support displayed no measurable WGS activity by 400°C, but after deposition-precipitation of gold using MDP2 and calcination for 12 hours in air at 400°C, appreciable catalytic activity was observed for a sample 1.3 wt % in Au operating at the same temperature (figure 10.21; table 10.3).

Table 10.3: Promotion of WGS activity in 3.6 m^2.g^{-1} ZnO by gold

[Au] (wt %)	d_{Au} (nm)	N_2-BET SA (m^2.g^{-1})	Reaction Rate @ ~ 400 °C	
			x 10^{-7} (mol CO).(g Au/ZnO).s^{-1}	x 10^{-8} (mol CO).m^{-2}. s^{-1}
0	n/a	3.6	0	0
1.3	Not measured	3.6	2.0	5.9

Similarly, an enhancement of WGS activity was also observed as a result of the deposition of gold in the case of the higher surface area novel ZnO (figure 10.22; table 10.4).

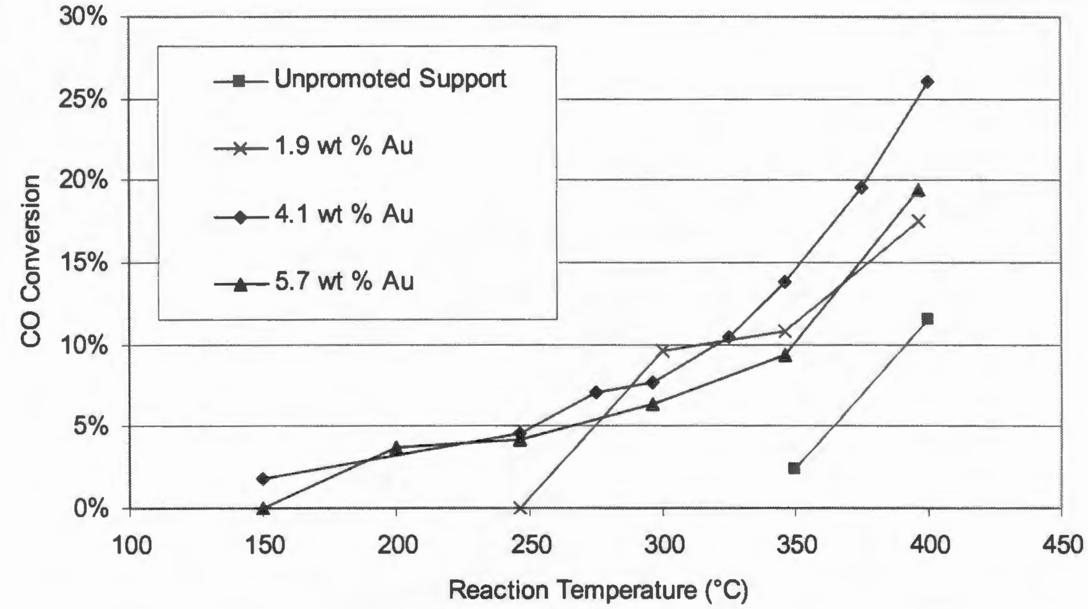

Figure 10.22: Promotion of WGS activity in ~ 30 $m^2.g^{-1}$ surface area Au/ZnO by gold

Table 10.4: WGS activity promotion by Au in ~ 30 $m^2.g^{-1}$ SA ZnO

[Au] (wt %)	d_{Au} (nm)	N_2-BET SA ($m^2.g^{-1}$)	Reaction Rate @ ~ 400 °C X_{CO} < 30%		
			x 10^{-7} (mol CO). (g Au/ZnO)$^{-1}$.s^{-1}	X 10^{-8} (mol CO). ($m^2_{catalyst\ surface\ area}$)$^{-1}$.$s^{-1}$	x 10^{-3} (mol CO). (mol Au)$^{-1}$.s^{-1}
0	n/a	44	3.2	0.73	-
1.9	3.7	30	5.1	1.7	5.2
4.1	4.4	30	7.3	2.4	3.5
5.11	4.6	33	5.10	1.7	2.0

Although the general enhancement of WGS activity when gold is dispersed across the support surface is clear, it's more detailed origin is not. Consider the WGS activity measured at 400°C: of the three Au/ZnO materials prepared at increasing gold loadings on the higher surface area novel ZnO, the intermediate gold loading produced the most active material when the rate of CO conversion is normalised with respect to total catalyst (gold and metal oxide support together) N_2-BET surface area, as well as on a per catalyst mass or catalyst volume basis. However, intrinsic activity (normalisation with respect to total moles of gold) decreases with increasing gold content (figure 10.23), and in fact when WGS activity is quantified in this way, at 400°C (when conversion is below ~ 30 %) the activity can be shown to decrease linearly with gold content (figure 10.24).

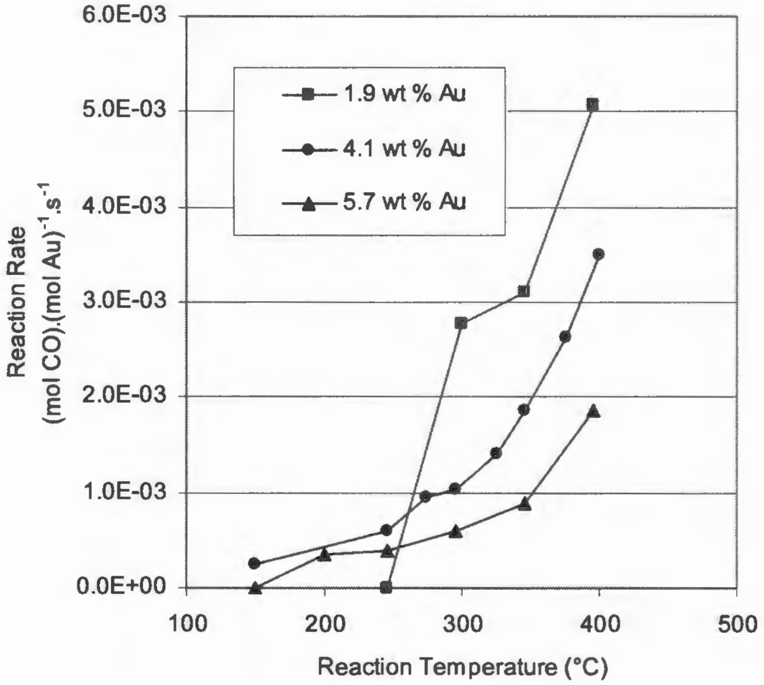

Figure 10.23: Rate of CO conversion per mole gold for ~ 30 $m^2.g^{-1}$ SA Au/ZnO materials

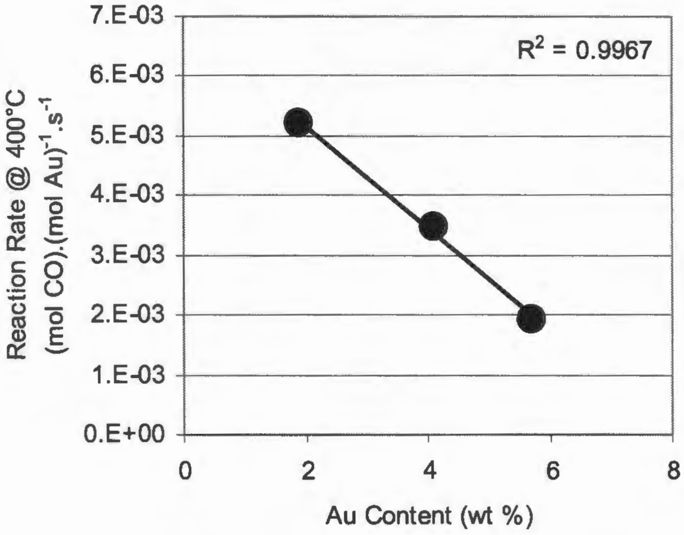

Figure 10.24: CO conversion at 400°C normalised wrt to total molar Au content for Au/ZnO materials on ~ 30 $m^2.g^{-1}$ SA ZnO

A possible explanation for this is that (under the specific reaction conditions) there exists some optimum (support surface) area number density of gold crystallites, and that the material with the lowest gold loading most nearly approaches this value, with the successively more heavily loaded materials moving incrementally further from this value. This hypothesis is predicated on the support playing an active role in the catalysis, and each gold crystallite requiring a certain surrounding area of dedicated support.

Another possible explanation is to assume that the slight increase in average gold crystallite size observed with increasing gold loading for this series is indicative of a genuine increase in the actual mean crystallite size, then the observed trend would be in-line with smaller crystallites being more catalytically active than larger ones, and the number density of these smaller particles decreasing with increasing gold loading.

To determine whether the increase in intrinsic activity with decreasing gold crystallite size suggested could be rationalised as a simple dispersion effect, the rate of CO conversion per exposed Au surface area has been calculated (figure 10.25 - refer §8.4.4 for a detailed explanation of the calculation and its inherent assumptions).

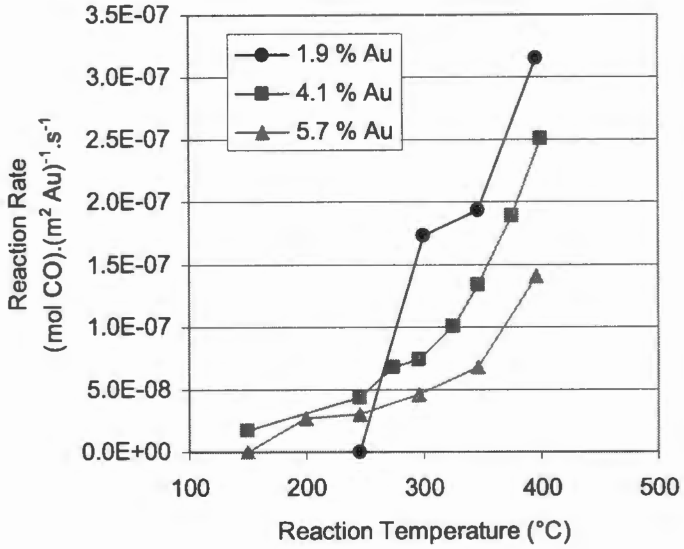

Figure 10.25: Rate of CO conversion per unit exposed Au surface area for Au/MO materials prepared from synthesized ZnO

Consideration of the data after this transformation suggests that the origin of the increased activity is more complicated than a simple dispersion effect, as the normalisation with respect to exposed gold surface area does not result in alignment of the curves, which would occur if the origin of the observed effect was attributable only to the number of active sites increasing with gold dispersion.

Furthermore, comparing the activity of this set of 3 Au/ZnO materials, prepared via deposition and reduction of $Au(OH)_3$ on ZnO, to that of with a material (1.7 wt % in Au) prepared via deposition of $Au(OH)_3$ on the ZnO precursor zinc hydroxycarbonate, followed by simultaneous decomposition of hydrozincite and reduction of $Au(OH)_3$ in a single heat treatment stage, confirms that a gap in understanding exists. The latter preparation appears to yield a far more active material (on all bases of comparison, although most importantly on a rate of CO conversion per mole of gold [figure 10.26]) than the former.

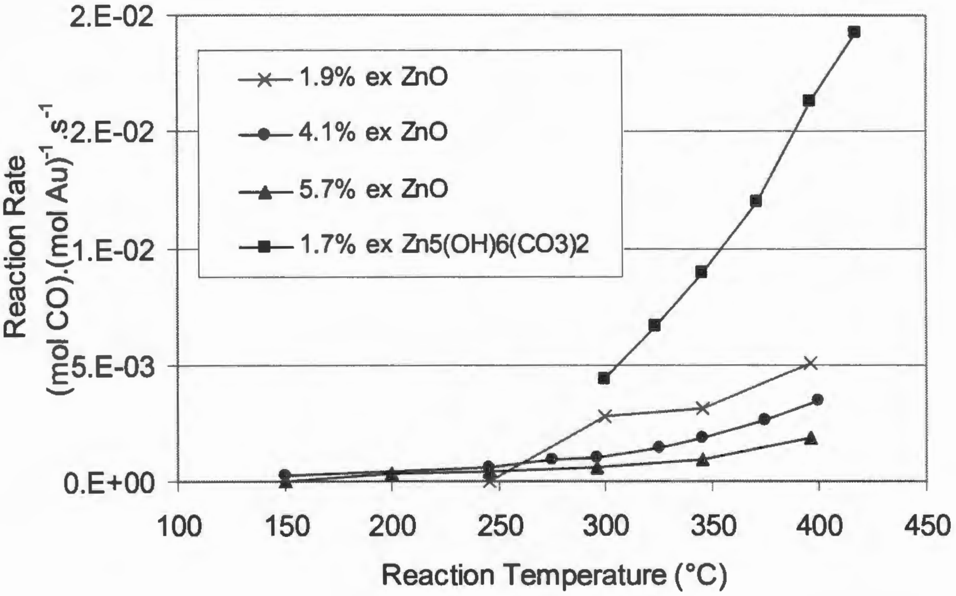

Figure 10.26: Reaction rate in terms of moles of CO converted per mole of gold per second over Au/ZnO materials prepared on synthesized ZnO and hydrozincite

Furthermore, the average gold crystallite size of the material prepared via simultaneous calcination of gold and support precursor is significantly larger (at 5.9 ± 1.7 nm; figure 10.27) than even a material bearing approximately three times as much gold but prepared via sequential calcination (d = 4.6 ± 1.7 nm @ 5.11 wt % Au). This suggests that either the surface properties of the support are different in the two cases, or that it is largely gold crystallites of a size below the detectable limit that are primarily responsible for the observed catalytic activity.

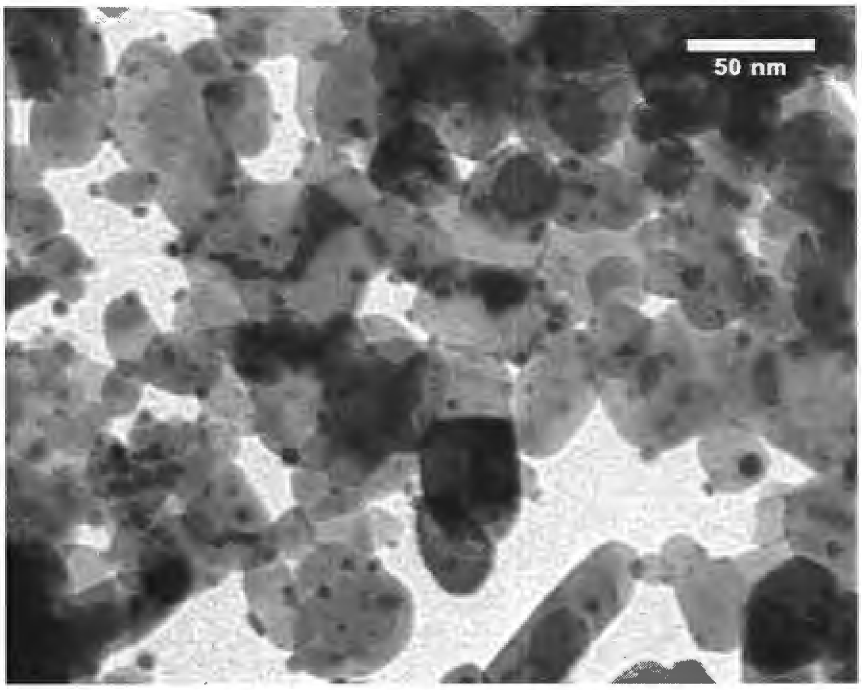

Figure 10.27: Sample TEM image of Au/ZnO prepared from $Au(OH)_3/Zn_5(OH)_6(CO_3)_2$ MDP2, pH 8, 1.53 wt % Au, d = 5.9 ± 1.7 nm

10.2.2 Au/TiO$_2$ WGC Reference and Commercial Cu/ZnO/Al$_2$O$_3$ Materials

Finally, the most active Au/ZnO material synthesized in this work [Au/ZnO from $Au(OH)_3/Zn_5(OH)_6(CO_3)_2$], the Au/$TiO_2$ reference from the World Gold Council and the commercial copper-based Cu/ZnO/Al_2O_3 WGS catalyst are compared.

On a per total catalyst mass basis (figure 10.28), it is evident that the commercial copper-based WGS catalyst is by far and away the most active material, with 1 g of material achieving 50 % CO conversion at 161°C, while the same mass of the Au/TiO_2 and the novel Au/ZnO only achieved the same level of conversion at temperatures of 259°C and 397°C, respectively (table 10.5).

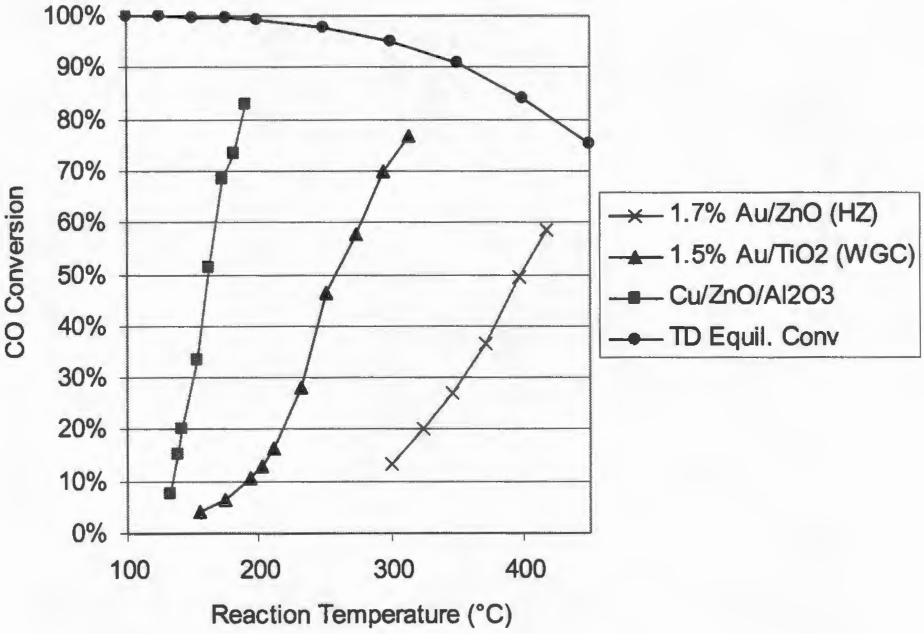

Figure 10.28: WGS activity comparison of $Cu/ZnO/Al_2O_3$, Au/TiO_2 WGC reference, and Au/ZnO from $Au(OH)_3/Zn_5(OH)_6(CO3)_2$ materials on an absolute CO conversion basis

Table 10.5: Temperatures for 50% CO conversion

Ranking	Material	T @ X_{CO} = 50% (°C)
1	$Cu/ZnO/Al_2O_3$	161
2	Au/TiO_2	259
3	Au/ZnO	397

However, when the data is re-interpreted on a per mol of group IB metal (ie Au or Cu) CO conversion basis (figure 10.29), the gold-based materials emerge as apparently far more active. The problem with making this comparison, however, is that the copper-based material is produced via co-precipitation, which results in the majority of the copper being locked-up in the chemically inaccessible interior of the material, whereas in the case of the gold-based materials – all produced via deposition-precipitation of gold solely on the immediately accessible surface of the support – one can safely assume that the vast majority of the gold content as detected by chemical analysis is potentially catalytically active (albeit approximating that the reaction occurs at most only on the total exterior surface of the supported particles).

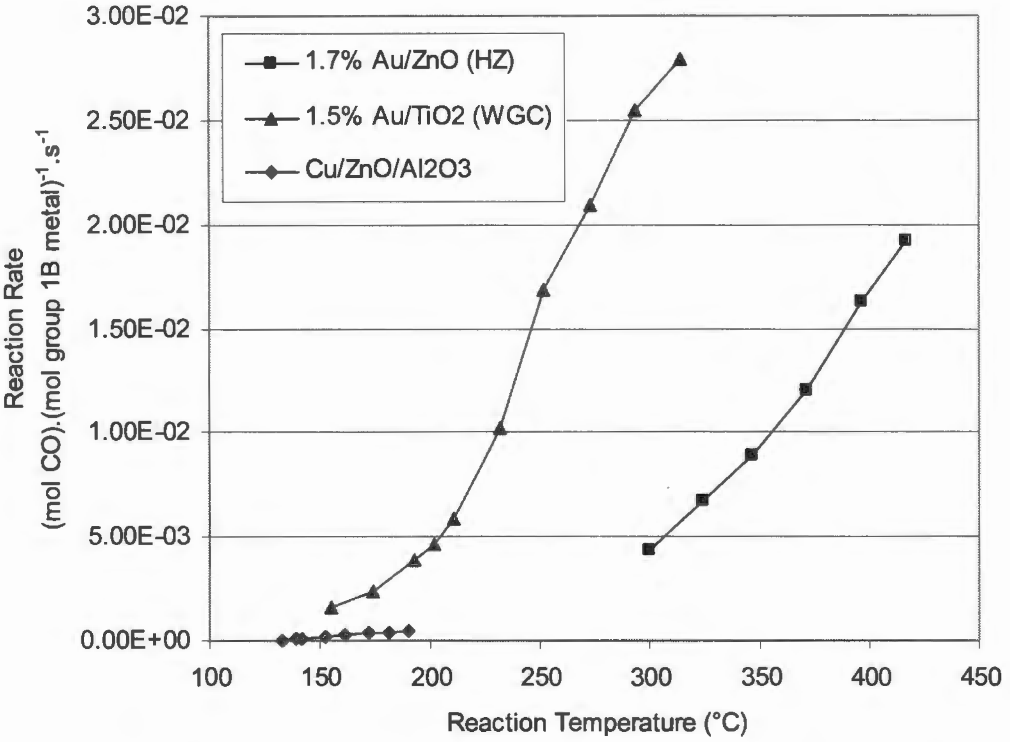

Figure 10.29: WGS activity comparison of
$Cu/ZnO/Al_2O_3$, Au/TiO_2 WGC reference, and Au/ZnO from $Au(OH)_3/Zn_5(OH)_6(CO3)_2$ materials
on the basis of CO conversion per mol of group 1B metal

In sum, these findings are in qualitative agreement with Sakurai *et al.* (1997), who regard Au/TiO_2 as being appreciably more active in terms of TOF than Au/ZnO (refer §3).

11

References

Andreeva, D., Idakiev, V., Tabokova, T. & Andreev, A. 'NOTE: Low-Temperature Water-Gas Shift Reaction over Au/α-Fe_2O_3' *Journal of Catalysis* **158** (1996a) 354-355.

Andreeva, D., Idakiev, V., Tabokova, T., Andreev, A. & Giovanoli, R. 'Low-temperature water-gas shift reaction on Au/α-Fe_2O_3 catalyst' *Applied Catalysis A: General* **134** (1996b) 275-283.

Andreeva, D., Idakiev, V.D., Tabakova, T.T. & Giovanoli, R. 'Low-temperature water-gas shift reaction on Au/TiO_2, A/α-Fe_2O_3 and Au/Co_3O_4 catalysts' *Bulgarian Chemical Communications* **30** (1998) 59-67.

Andreeva, D., Idakiev, V., Tabakova, T., Ilieva, L., Falaras, P., Bourlinos, A. & Travlos, A. 'Low-temperature water-gas shift reaction over Au/CeO_2 catalysts' *Catalysis Today* **72** (2002a) 51-57.

Andreeva, D. 'Low Temperature Water Gas Shift Over Gold Catalysts' *Gold Bulletin* **35** (2002) 82-88.

Atkins, P.W., 1998, Physical Chemistry (6th edition), Oxford University Press, USA.

Bamwenda, G.R., Tsubota, S., Nakamura, T. & Haruta, M. 'The influence of the preparation methods on the catalytic activity of platinum and gold supported on TiO_2 for CO oxidation' Catalysis Letters **44** (1997) 83-87.

Bekker, P & Robb, W. 'Kinetics of hydrolysis of the tetrachloroaurate(III) anion in aqueous perchloric acid' *Inorganic and Nuclear Chemistry Letters* **8** (1972) 849-854.

Boccuzzi, F., Chiorino, A., Manzoli, M., Andreeva, D. & Tabakova, T. 'FTIR Study of the Low-Temperature Water–Gas Shift Reaction on Au/Fe_2O_3 and Au/TiO_2 Catalysts' *Journal of Catalysis* **188** (1999) 176-185.

Bond, G.C & Thompson, D.T 'Catalysis by Gold' *Catalysis Reviews – Science and Engineering* **41** (1999) 319-388.

Bonivardi, A.L. & Baltanas, M.A. 'Preparation of Pd/SiO2 Catalysts for Methanol Synthesis' *Journal of Catalysis* **125** (1990) 243-259.

Budavari, S (editor), 1996, *The Merck Index (12th Edition)*. Merck & Co., USA.

Buehrer, T.F. & Roseveare, W.E. 'The free energy of auric oxide as determined from measurements of the gold-auric oxide electrode' *Journal of the American Chemical Society* **49** (1927) 1989-1991.

Campbell, C.T. 'Ultrathin metal films and particles on oxide surfaces: structural, electronic and chemisorptive properties' *Surface Science Reports* **27** (1997) 1-111.

Cha, D.Y & Parravano, G. 'Surface Reactivity of Supported Gold – I. Oxygen Transfer Between CO and CO_2' *Journal of Catalysis* **18** (1970) 200-211.

Che, M. & Bennet, C.O. 'The Influence of Particle Size on the Catalytic Properties of Supported Metals' in: Eley, D.D., Pines, H. & Weisz, P.B. (Editors) *Advances in Catalysis* **36** (1989) 55-172.

Cotton, A.F. & Wilkinson, G. *Advanced Inorganic Chemistry* (4th edition) 1980, J Wiley & Sons, United Kingdom.

Claus, P., Hofmeister, H. & Mohr, C. 'Identification of Active Sites and Influence of Real Structure of Gold Catalysts in the Selective Hydrogenation of Acrolein to Allyl Alcohol' *Gold Bulletin* **37** (2004) 181-186.

Debeila, M.A., Coville, N.J., Scurrell, M.S. & Hearne, G.R. 'DRIFTS studies of the interaction of nitric oxide and carbon monoxide on Au–TiO2.' *Catalysis Today* **72** (2002) 79–87.

Deng, W., de Jesus, J., Saltsburg, H. & Flytzani-Stephanopoulos, M. 'Low-content gold-ceria catalysts for the water-gas shift and preferential CO oxidation reactions' *Applied Catalysis A: General* **291** (2005) 126-135.

Ebbing, D.D. (ed). *General Chemistry* (4th edition) 1993, Houghton-Mifflin, USA.

Edwards, N., Ellis, S.R., Frost, J.C., Golunski, S.E., van Keulen, A.N.J., Lindewald, N.G. & Reinkingh, J.G. 'On-board hydrogen generation for transport applications: the HotSpot™ methanol processor' *Journal of Power Sources* **71** (1998) 123-128.

Finar, I.L. *Organic Chemistry: Volume One: The Fundamental Principles* 1959, Longmans, Great Britain.

Fu, Q., Saltsburg. H & Flytzani-Stephanopoulos, M. 'Active Non-Metallic Au and Pt Species on Ceria-based Water-Gas Shift Catalysts' *Science* **301** (2003a) 935-938.

Fu, Q., Kudriavtseva, S., Saltsburg, H. & Flytzani-Stephanopoulos, M. 'Gold–ceria catalysts for low-temperature water-gas shift reaction' *Chemical Engineering Journal* **93** (2003b) 41–53.

Gammons, C.H., Yu, Y. & Williams-Jones, A.E. 'The disproportionation of gold(I) chloride complexes at 25 to 200°C' *Geochimica et Cosmochimica Acta* **61** (1997) 1971-1983.

Ghenciu, A.F. 'Review of fuel-processing catalysts for hydrogen production in PEM fuel cell systems' *Current Opinion in Solid State Surface Science* **6** (2002) 389-399.

Haruta, M., Yamada, N., Kobayashi, T. & Iijima, S. 'Gold Catalysts Prepared by Coprecipitation for Low-Temperature Oxidation of Hydrogen and Carbon Monoxide' *Journal of Catalysis* **115** (1989) 301-309.

Haruta, M., Tsubota, S., Kobayashi, T., Kageyama, H., Genet, M.J. & Delmon, B. 'Low-Temperature Oxidation of CO over Gold Supported on TiO_2, α-Fe_2O_3, and Co_3O_4' *Journal of Catalysis* **144** (1993) 175-192.

Haruta, M. 'Size- and support-dependency in the catalysis of gold' *Catalysis Today* **36** (1997) 153-166.

Haruta, M. & Date, M. 'Advances in the catalysis of Au nanoparticles' *Applied Catalysis A: General* **222** (2001) 427-437.

Haruta, M. 'Gold as a Novel Catalyst in the 21st Century: Preparation, Working Mechanism and Applications' *Gold Bulletin* **37** (2004) 27-36.

Hodge, N.A., Kiely, C.J., Whyman, R., Siddiqui, M.R.H., Hutchings, G.J., Pankhurst, Q.A., Wagner, F.E., Rajaram, R.R., Golunski, S.E. 'Microstructural comparison of calcined and uncalcined gold/iron-oxide catalysts for low-temperature CO oxidation' *Catalysis Today* **72** (2002) 133–144.

Ivanova, S., Petit, C. & Pitchon, V. 'Preparation of gold catalysts by exchange on alumina' Laboratoire des Matériaux, Surfaces et Procédés pour la Catalyse, 2003, private communication (available as http://icc2004.catalyse.cnrs.fr/CDROM/P1-334.pdf as at 23-09-03).

Jacobs, G., Chenu, E., Patterson, P.M, Williams, L., Sparks, D., Thomas, G. & David, B.H 'Water-gas shift: comparative screening of metal promoters for metal/ceria systems and role of the metal' *Applied Catalysis A: General* **258** (2004) 203-214.

Kohler, M.A., Lee, J.C., Trimm, D.L., Cant, N.W. & Wainwright, M.S. 'Preparation of Cu/SiO_2 Catalyst by the Ion-Exchange Technique' *Applied Catalysis* **31** (1987a) 309-321.

Kohler, M.A., Curry-Hyde, H.E., Hughes, A.E., Sexton, B.A. & Cant, N.W. 'The Structure of Cu/SiO_2 Catalysts Prepared via Ion-Exchange Technique' *Journal of Catalysis* **108** (1987b) 323-333.

Kirk, R.E & Othmer, D.F., 1995, *Encyclopedia of Chemical Technology (3rd Edition)*, John Wiley & Sons, USA.

Kung, H.H, Kung, M.C & Costello, C.K 'Supported Au catalyst for low temperature CO oxidation' *Journal of Catalysis* **216** (2003) 425-432.

Lee, S-J, Gavriilidis, A., Pankhurst, Q.A., Kyek, A., Wagner, F.E., Wong, P.C.L., Yeung, K.L. 'Effect of Drying Conditions of Au–Mn Co-Precipitates for Low-Temperature CO Oxidation' *Journal of Catalysis* **200** (2001) 298–308.

Li, Y., Flytzani-Stephanopoulos, M. 'Low-temperature water-gas shift over Cu- and Ni-loaded cerium oxide catalysts' *Applied Catalysis B: Environmental* **27** (2000) 179-191.

Mohr, C., Hofmeister, H., Radnik, J. & Claus, P. 'Identification of Active Sites in Gold-Catalysed Hydrogenation of Acrolein' *Journal of the American Chemical Society* **125** (2003) 1905-1911.

Moon, D.J., Skreekumar, K., Lee, S.D., Lee, B.G. & Kim, H.S. 'Studies on gasoline fuel processor systems for fuel-cell powered vehicles application' *Applied Catalysis A: General* **215** (2001) 1-9.

Moosath, S.S 'Studies on Hydrated Ceric Oxide' *Journal of Inorganic and Nuclear Chemistry* **11** (1959) 286-289.

Moulijn, J.A., Makkee, M., van Diepen, A. 2001, *Chemical Process Technology*, Wiley, England.

Muller, O., Newnham, R.E & Roy, R. 'Preliminary study of new crystalline gold oxides' *Journal of Inorganic and Nuclear Chemistry* **31** (1969) 2966-2970.

Munteanu, G., Ilieva, L. & Andreeva, D. 'Kinetic parameters obtained from TPR data for α-Fe_2O_3 and Au/α-Fe_2O_3 systems' *Thermochimica Acta* **291** (1997) 171-177.

Murphy, P.J. & LaGrange, M.S. 'Raman spectroscopy of gold chloro-hydroxy speciation in fluids at ambient temperature and pressure: A re-evaluation of the effects of pH and chloride concentration' *Geochimica et Cosmochimica Acta* **62** (1998) 3515-3526.

Oh, H-S., Yang, J.H., Costello, C.K., Wang, W.M., Bare, S.R., Kung, H.H. & Kung, M.C. 'Selective Catalytic Oxidation of CO: Effect of Chloride on Supported Au Catalysts' *Journal of Catalysis* **210** (2002) 375–386.

Okazawa, T., Kohyama, M. & Kido, Y. 'Electronic properties of Au nano-particles supported on stoichiometric and reduced TiO_2 (110) substrates' *Surface Science* **600** (2006) 4430-4437.

Pan, P. & Wood, S.A 'Gold-chloride complexes in very acidic aqueous solutions and at temperatures 25-300°C: A laser Raman spectroscopic study' *Geochimica et Cosmochimica Acta* **55** (1991) 2365-2371.

Park, E.D. & Lee, J.S 'Effects of Pretreatment Conditions on CO Oxidation over Supported Au Catalysts' *Journal of Catalysis* **186** (1999) 1–11.

Parks, G.A. 'The isoelectric points of solid oxides, solid hydroxides, and aqueous hydroxo complex systems' *Chemical Reviews* **65** (1975) 177-198.

Peck, J.A., Tait, C.D., Swanson, B.I. & Brown, G.E. 'Speciation of aqueous gold(III) chlorides from ultraviolet/visible absorption and Raman/resonance Raman spectroscopies' *Geochimica et Cosmochimica Acta* **55** (1991) 671-676.

Phala, N.S., Klatt, G. & van Steen, E. 'Gold-Catalysed Syngas Conversion: Pathways and Size Effects' *unpublished*.

Phala, N.S., Klatt, G., van Steen, E. , French, S. A., Sokol, A. A., Catlow, C. R. A. 'The Nature of the Oxidation States of Gold on ZnO' *unpublished* (2004).

Rhodes, C., Hutchings, G.J., Ward, A.M. 'Water-gas shift reaction: finding the mechanistic boundary' *Catalysis Today* **23** (1995) 43-58.

Rich, R. & Taube, H. 'The uncatalysed exchange of Cl^- and $AuCl_4^-$' *The Journal of Physical Chemistry* **58** (1954) 1-5.

Roberts, S. 2001, *Performance of Gold Catalysts for Low Temperature Water gas Shift* University of Cape Town Press, RSA.

Roseveare, W.E. & Buehrer, T.F. 'The preparation and analysis of pure auric oxide' *Journal of the American Chemical Society* **49** (1927) 1221-1226.

Sakurai, H., Tsubota, S. & Haruta, M. 'Hydrogenation of CO_2 over gold supported on metal oxides' *Applied Catalysis A: General* **102** (1993) 125-136.

Sakurai, H. & Haruta, M. 'Carbon dioxide and carbon monoxide hydrogenation over gold supported on titanium, iron and zinc oxides' *Applied Catalysis A: General* **127** (1995) 93-105.

Sakurai, H. & Haruta, M. 'Synergism in methanol synthesis from carbon dioxide over gold catalysts supported on metal oxides' *Catalysis Today* **29** (1996) 361-365.

Sakurai, H., Ueda, A., Kobayashi, T. & Haruta, M. 'Low-temperature water-gas shift over gold deposited on TiO_2' *Chemical Communications* (1997) 271-272.

Sharpe, A.G. *Inorganic Chemistry (3rd edition)* 1992, Longman Scientific & Technical, Singapore.

Skibsted, L.H. & Bjerrum, J. 'Studies on Gold Complexes. I. Robustness, Stability and Acid Dissociation of the Tetrammine(III) Ion' *Acta Chemica Scandinavica A* **28** (1974) 740-746.

Smith, G. & Reverson, L. 'The Adsorption of Complex Ammonium Ions by Silica Gel' *Journal of the American Chemical Society* **52** (1930) 2584-2585.

Song, C. 'Fuel processing for low temperature and high temperature fuel cells Challenges, and opportunities for sustainable development in the 21st century' *Catalysis Today* **221** (2001) 17-49.

Sze, C., Gulari, E. & Demczyk, B.G. 'Structure of coprecipitated gold-iron oxide catalyst materials' *Materials Letters* **36** (1998) 11-16.

Tabakova, T., Idakiev, V., Andreeva, D. & Mitov, I. 'Influence of the microscopic properties of the support on the catalytic activity of Au/ZnO, Au/ZrO_2, Au/Fe_2O_3, Au/Fe_2O_3-ZnO, Au/Fe_2O_3-ZrO_2 catalysts for the WGS reaction' *Applied Catalysis A: General* **202** (2000) 91-97.

Thompson, D. 'New Advanced in Gold Catalysis Part II' *Gold Bulletin* **32** (1999) 12-19.

Tsai, H., Hu, E., Perng, K., Chen, M., Wu, J-C & Chang, Y-S 'Instability of gold oxide Au_2O_3' *Surface Science* **537** (2003) L447-L450.

Tsubota, S., Haruta, M., Kobayashi, T., Ueda, A. & Nakahara, in: Poncelet, G., Jacobs, P.A, Grange, P. & Delmon, B. (Editors), '*Preparation of Catalysts VI*', Elsevier, Amsterdam, 1995, 695-704.

Twigg, M.V. (Editor), 1989, *Catalyst Handbook*, Wolfe Publishing, England.

Urban, P.M., Funke, A., Müller, J.T., Himmen, M. & Docter, A. 'Catalytic processes in solid polymer electrolyte fuel cell systems' *Applied Catalysis A: General* **221** (2001) 459-470.

Valden, M., Lai, X., Goodman, D. W. 'Onset of Catalytic Activity of Gold Clusters on Titania with the Appearance of Nonmetallic Properties' *Science* **281** (1998) 1647-1650.

Wang, G.Y., Zhang, W.X., Lian, H.L., Jiang, D.Z. & Wu, T.H. ‘Effect of calcination temperatures and precipitant on the catalytic performance of Au/ZnO catalysts for CO oxidation at ambient temperature and in humid circumstances’ *Applied Catalysis A: General* **239** (2003) 1–10.

Appendix Gold Deposition Process Data

12

12.1 Canonical Deposition-Precipitation Method of Tsubota *et al.* (1995)

12.1.1 DP - pH Series – 3.6 $m^2.g^{-1}$ ZnO

Method: DP

Support: 3.6 $m^2.g^{-1}$ commercial ZnO from SaarChem

Series: pH

Table 12.1: Process Summary - DP - pH Series – 3.6 $m^2.g^{-1}$ ZnO

Ageing pH	Au Content of Au/ZnO (wt %)	Extent of Support Dissolution (%)	Au Mass Balance		
			Catalyst (%)	Filtrate (%)	Balance (%)
5	7.75	52.43	87.3	9.5	3.2
6	3.95	1.83	88.2	5.0	6.8
7	2.86	1.53	63.3	13.9	22.8
8	1.48	0.01	32.7	67.4	- 0.1
9	0.55	1.25	12.0	87.4	0.6

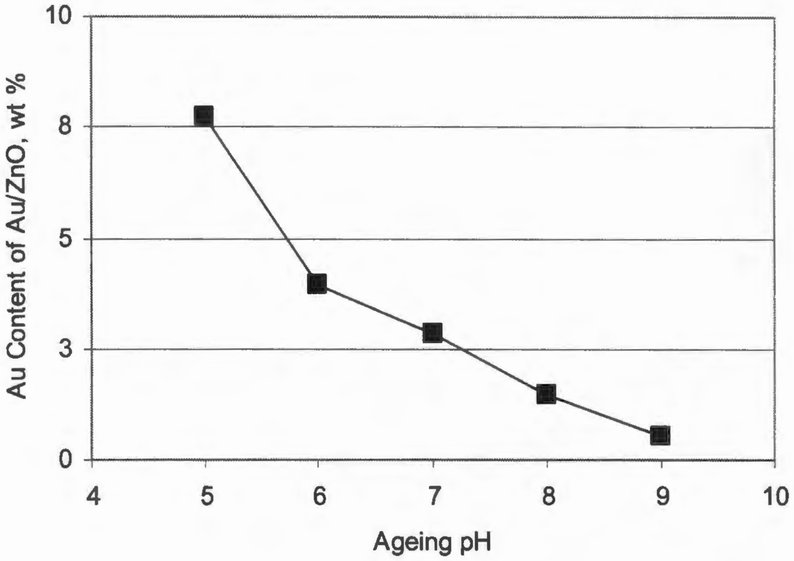

Figure 12.1: Au weight content of Au/ZnO as a function of pH (DP - pH Series – 3.6 $m^2.g^{-1}$ ZnO)

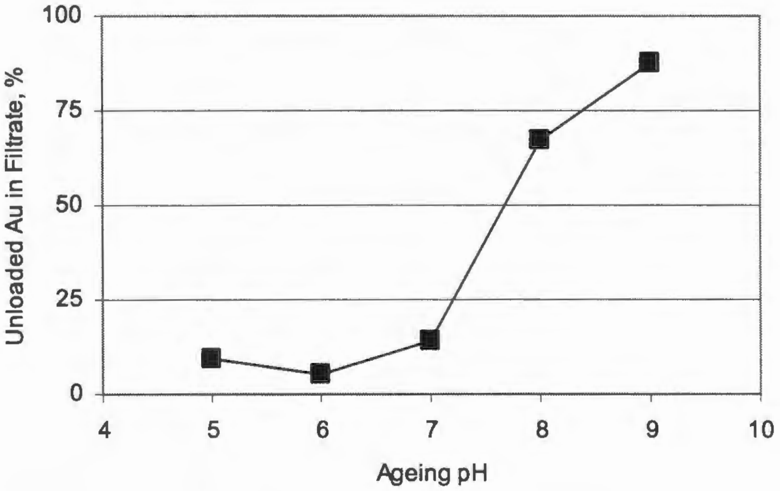

Figure 12.2: Unloaded Au in filtrate as a function of pH (DP - pH Series – 3.6 $m^2.g^{-1}$ ZnO)

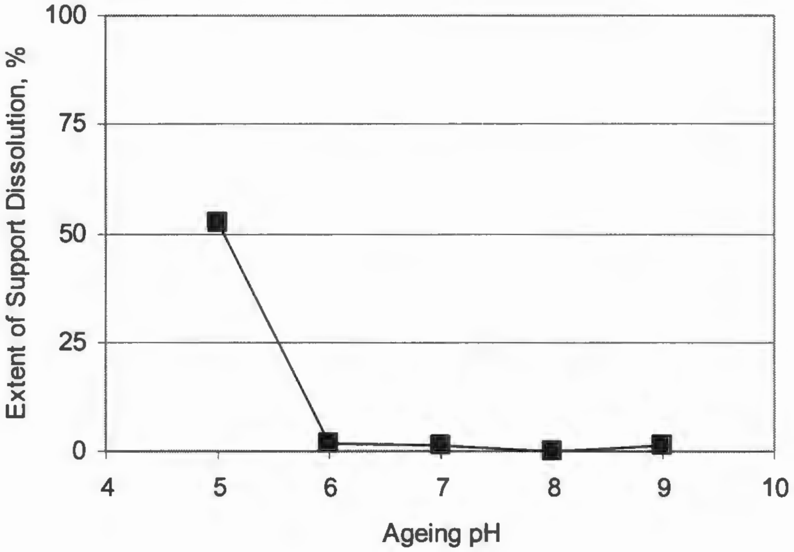

Figure 12.3: Extent of ZnO support dissolution as a function of pH
(DP - pH Series – 3.6 $m^2.g^{-1}$ ZnO)

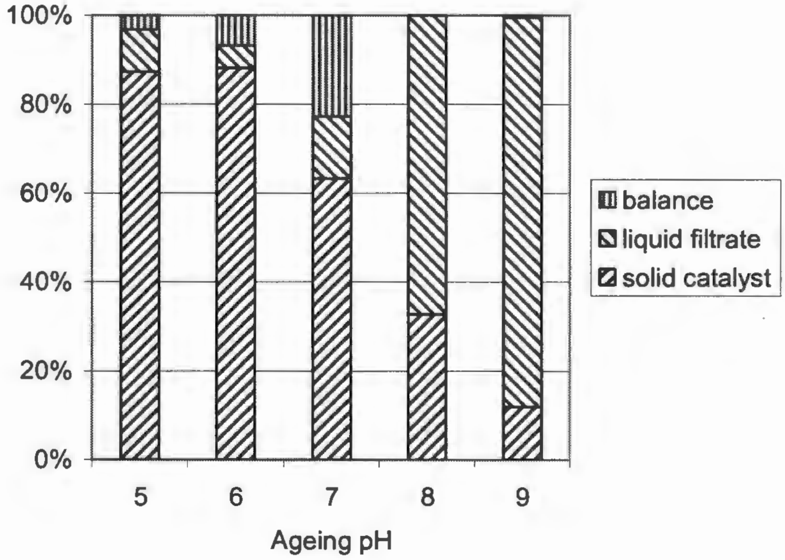

Figure 12.4: Au mass balances
(DP - pH Series – 3.6 $m^2.g^{-1}$ ZnO)

12.2 Modified method of *Fu et al.* (2006)

12.2.1 Constant Ageing pH – MDP1

12.2.1.1 MDP1 - pH Series – 3.6 $m^2.g^{-1}$ ZnO

Method: MDP1

Support: 3.6 $m^2.g^{-1}$ commercial ZnO from SaarChem

Series: pH

Table 12.2: Process Summary – MDP1 - pH Series – 3.6 $m^2.g^{-1}$ ZnO

Ageing pH	Au Content of Au/ZnO (wt %)	Extent of Support Dissolution (%)	Au Mass Balance		
			Catalyst (%)	Filtrate (%)	Balance (%)
6	0.08	5.6	3.8	86.6	9.5
7	0.99	0.9	50.2	25.9	23.9
8	1.15	0.4	58.5	18.3	23.2
8.9	0.68	2.1	33.8	56.4	9.9
9	0.71	2.0	36.2	57.9	5.9

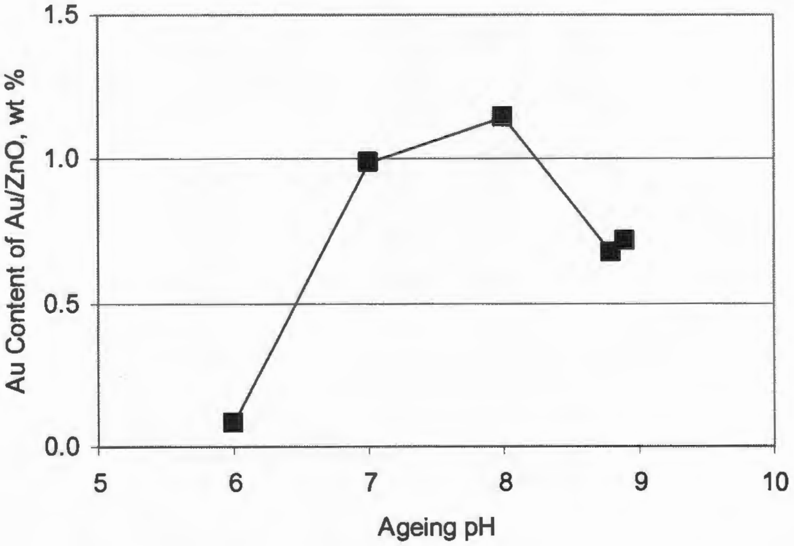

Figure 12.5: Au Content of Au/ZnO as a function of pH
(MDP1 - pH Series – 3.6 $m^2.g^{-1}$ ZnO)

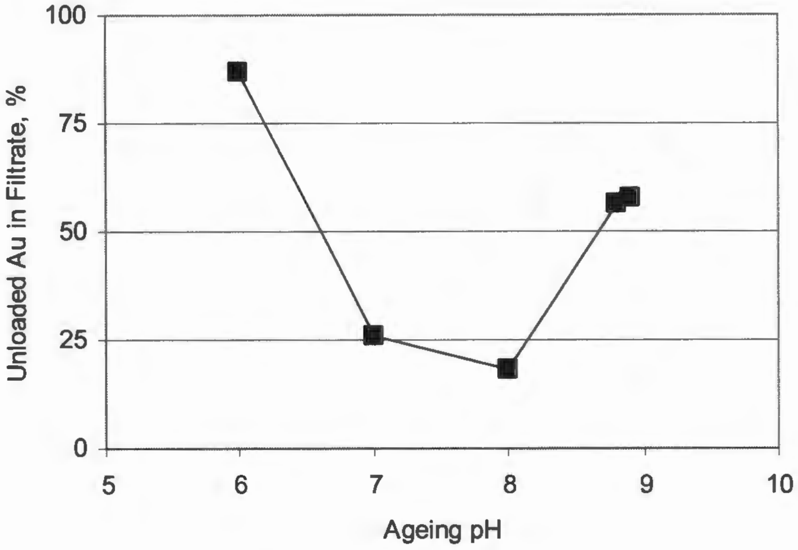

Figure 12.6: Unloaded Au in filtrate as a function of pH
(MDP1 - pH Series – 3.6 $m^2.g^{-1}$ ZnO)

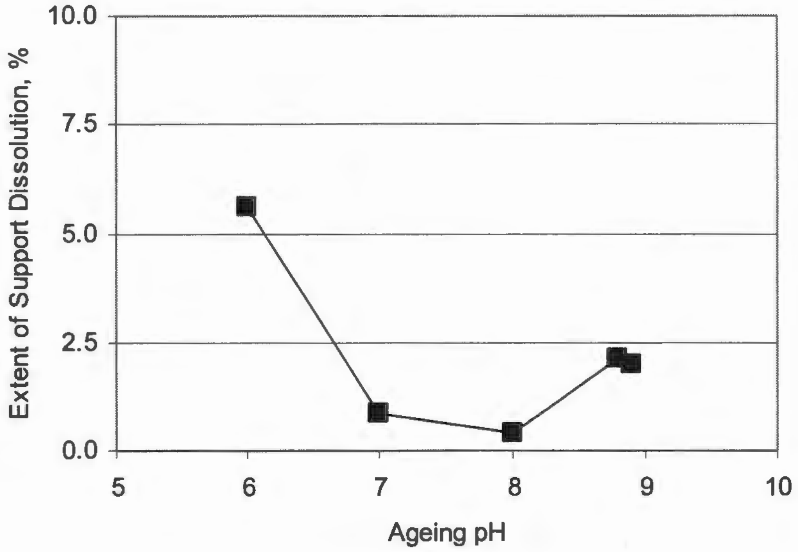

Figure 12.7: Extent of ZnO support dissolution as a function of pH
(MDP1 - pH Series – 3.6 $m^2.g^{-1}$ ZnO)

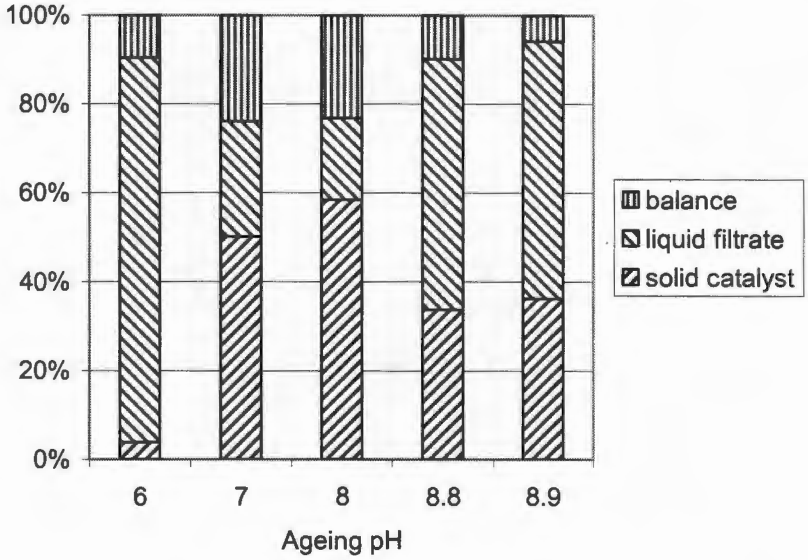

Figure 12.8: Au mass balances
(MDP1 - pH Series – 3.6 $m^2.g^{-1}$ ZnO)

12.2.1.2 MDP1 - Loading Series - 3.6 $m^2.g^{-1}$ ZnO

Method: MDP1

Support: 3.6 $m^2.g^{-1}$ synthetic ZnO from SaarChem

Series: Loading at pH 8

Table 12.3: Process Summary – MDP1 - Loading Series – 3.6 $m^2.g^{-1}$ ZnO

Intended Au Content (wt %)	Au Content Of Au/ZnO (wt %)	Extent of Support Dissolution (%)	Au Mass Balance		
			Catalyst (%)	Filtrate (%)	Balance (%)
0.9	0.66	0.14	69.3	15.9	14.8
1.9	1.18	0.48	62.7	18.3	19.0
2.8	1.60	1.28	56.2	23.8	20.0
3.7	2.07	2.20	54.4	23.1	22.4

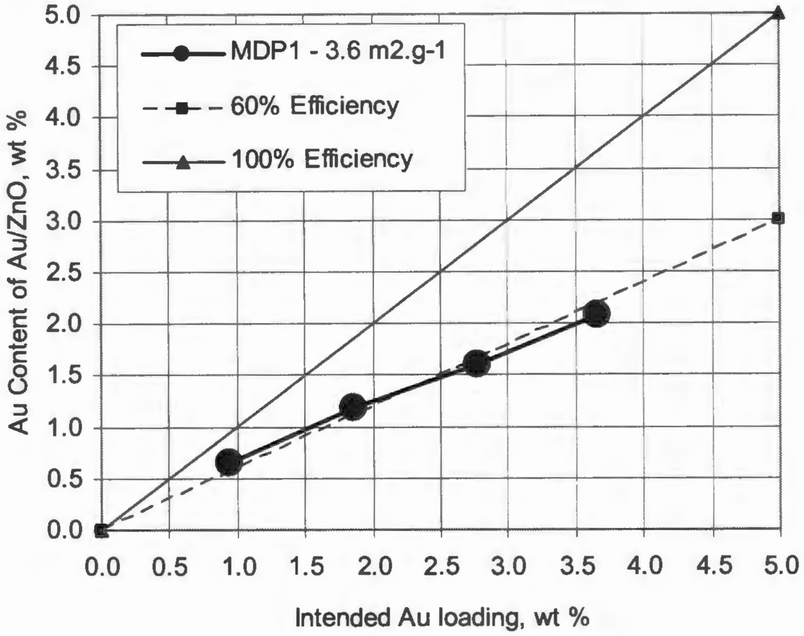

Figure 12.9: Au content of Au/ZnO as a function of intended loading (MDP1 - Loading Series - 3.6 $m^2.g^{-1}$ ZnO)

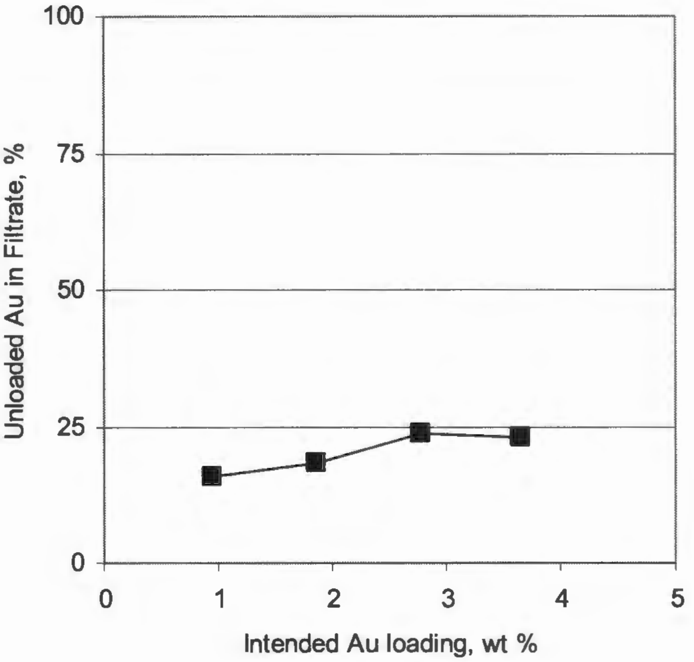

Figure 12.10: Unloaded Au in filtrate as a function of intended loading (MDP1 - Loading Series - 3.6 $m^2.g^{-1}$ ZnO)

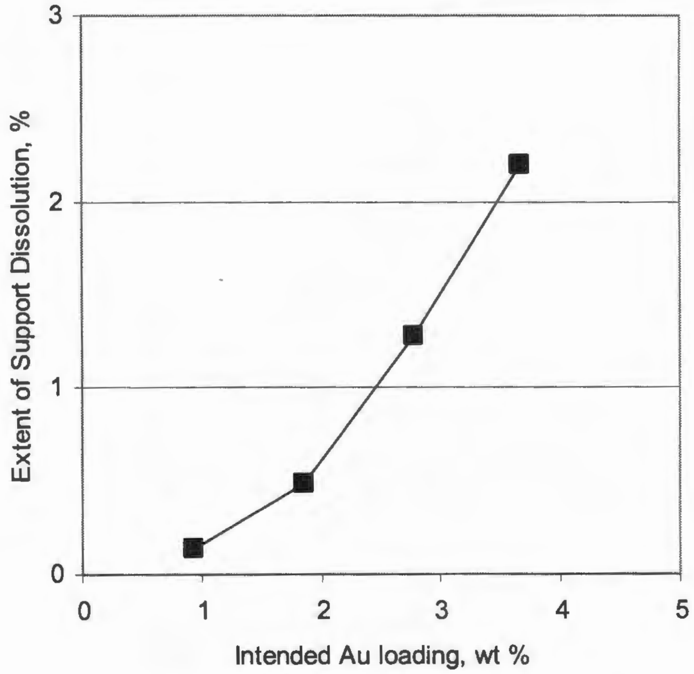

Figure 12.11: Extent of support dissolution as a function of intended loading (MDP1 - Loading Series - 3.6 m^2.g^{-1} ZnO)

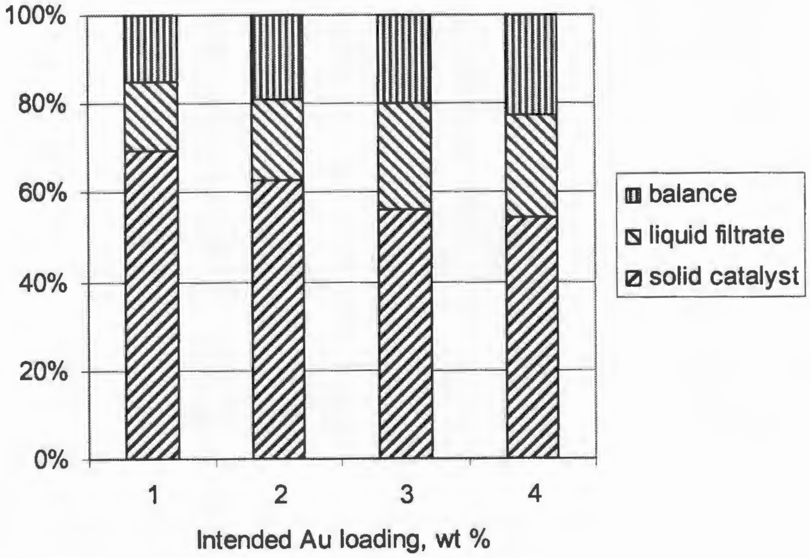

Figure 12.12: Au mass balances
(MDP1 - Loading Series - 3.6 m^2.g^{-1} ZnO)

12.2.1.3 MDP1 - Loading Series ~ 30 $m^2.g^{-1}$ ZnO

Method: MDP1

Support: ~ 30 $m^2.g^{-1}$ synthesized ZnO

Series: Loading at pH 8

Table 12.4: Process Summary – MDP1 - Loading Series ~ 30 $m^2.g^{-1}$ ZnO

Intended Au Content (wt %)	Au Content Of Au/ZnO (wt %)	Extent of Support Dissolution (%)	Au Mass Balance		
			Catalyst (%)	Filtrate (%)	Balance (%)
0.9	0.66	0.14	69.3	15.9	14.8
1.9	1.18	0.48	62.7	18.3	19.0
2.8	1.60	1.28	56.2	23.8	20.0
3.7	2.07	2.20	54.4	23.1	22.4

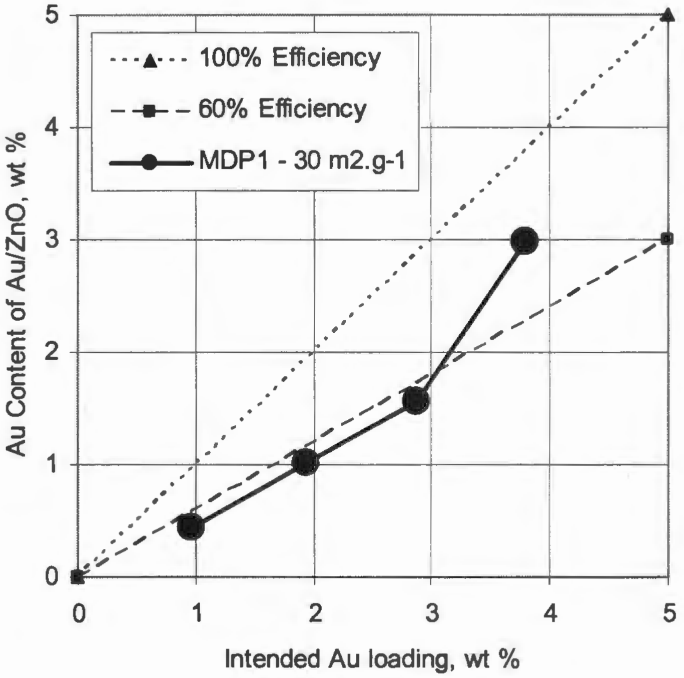

Figure 12.13: Gold content of Au/ZnO as a function of intended loading (MDP1 - Loading Series ~ 30 $m^2.g^{-1}$ ZnO)

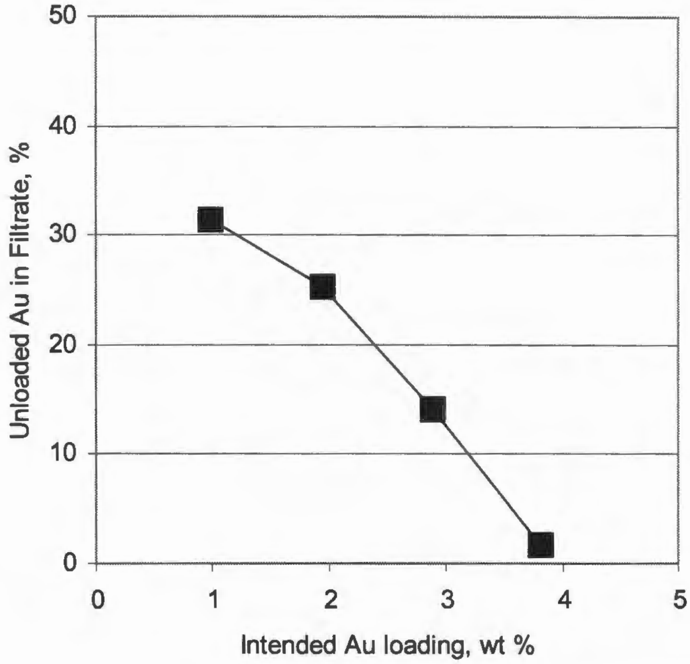

Figure 12.14: Unloaded gold in filtrate as a function of intended loading (MDP1 - Loading Series ~ 30 m^2.g^{-1} ZnO)

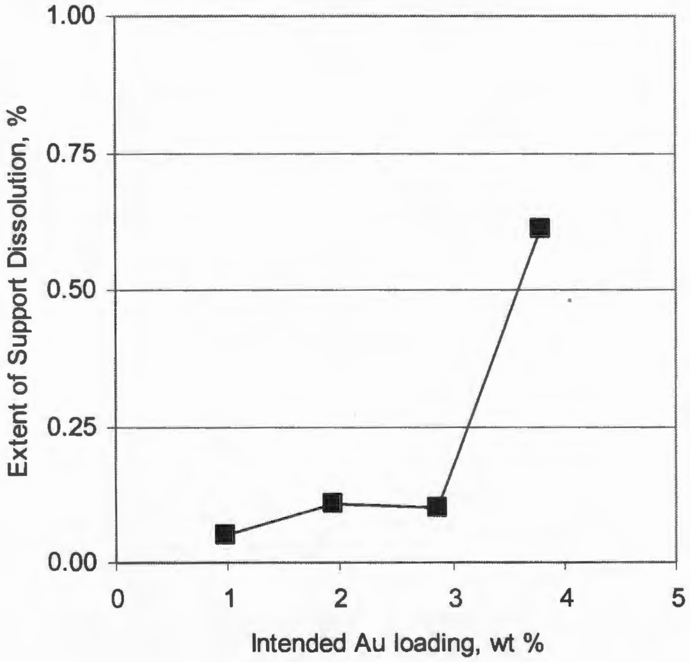

Figure 12.15: Extent of support dissolution as a function of intended loading (MDP1 - Loading Series ~ 30 m^2.g^{-1} ZnO)

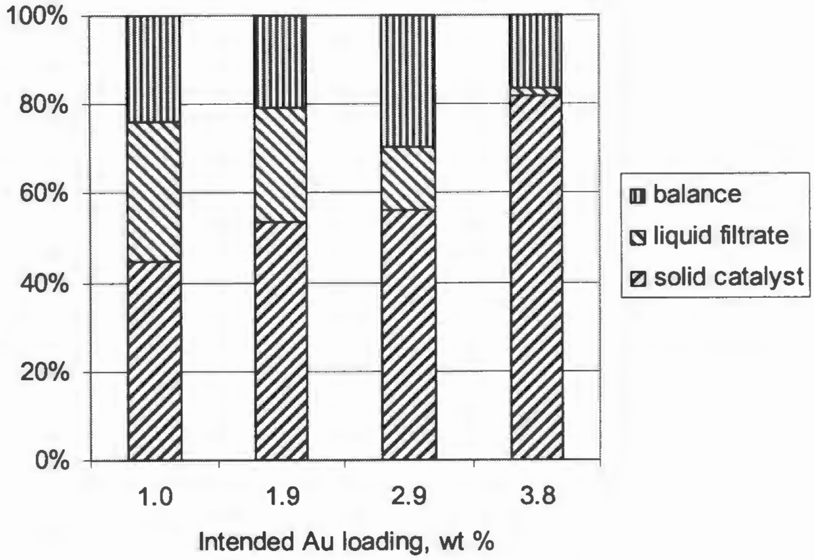

Figure 12.16: Au mass balances
(MDP1 - Loading Series ~ 30 $m^2.g^{-1}$ ZnO)

12.2.2 Uncontrolled Ageing pH – MDP2

12.2.2.1 MDP2 – Loading Series ~ 30 $m^2.g^{-1}$ ZnO

Method: MDP2

Support: ~ 30 $m^2.g^{-1}$ commercial ZnO from SaarChem

Series: Loading at pH 8

Table 12.5: Process Summary – MDP2 - Loading Series ~ 30 $m^2.g^{-1}$ ZnO

Intended Au Content (wt %)	Au Content Of Au/ZnO (wt %)	Extent of Support Dissolution (%)	Au Mass Balance		
			Catalyst (%)	Filtrate (%)	Balance (%)
2.0	1.94	2.6	94.5	6.1	- 0.6
4.0	3.80	5.4	102	3.2	-5.2
6.0	5.59	7.7	94.5	11.2	-5.7

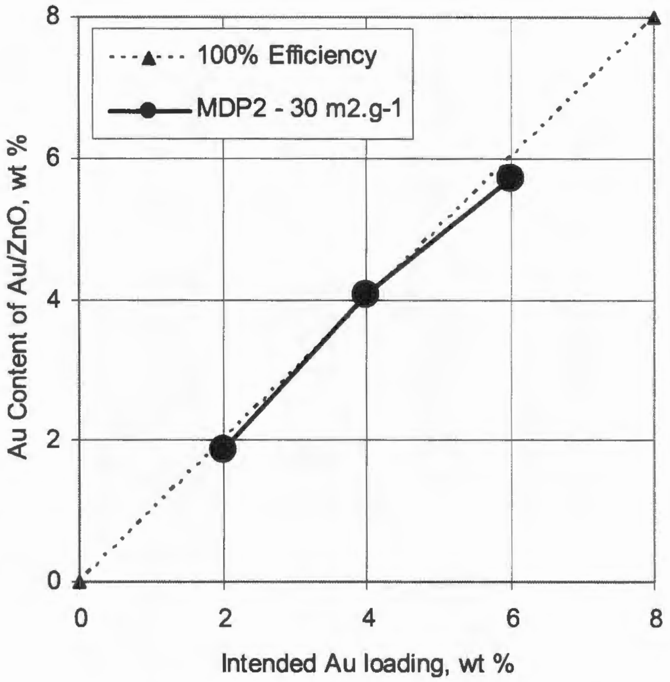

Figure 12.17: Au content of Au/ZnO as a function of intended loading (MDP2 – Loading Series ~ 30 $m^2.g^{-1}$ ZnO)

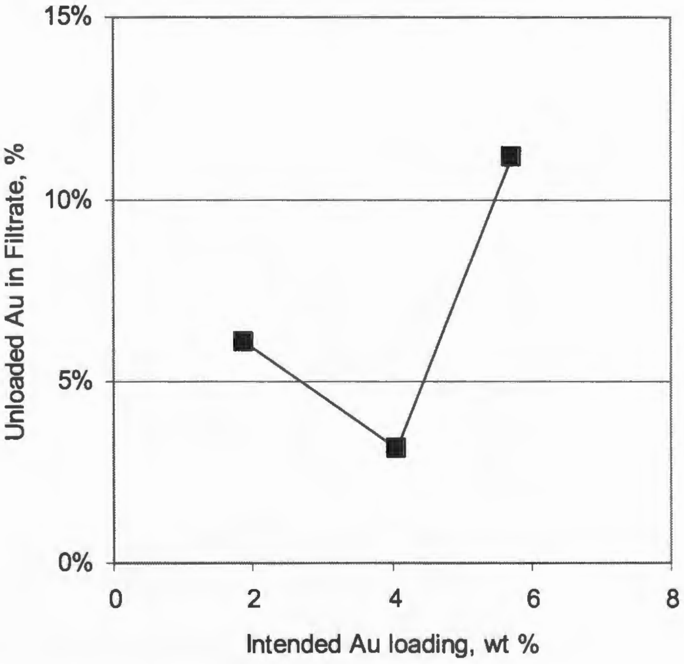

Figure 12.18: Unloaded Au in filtrate as a function of intended loading (MDP2 – Loading Series ~ 30 $m^2.g^{-1}$ ZnO)

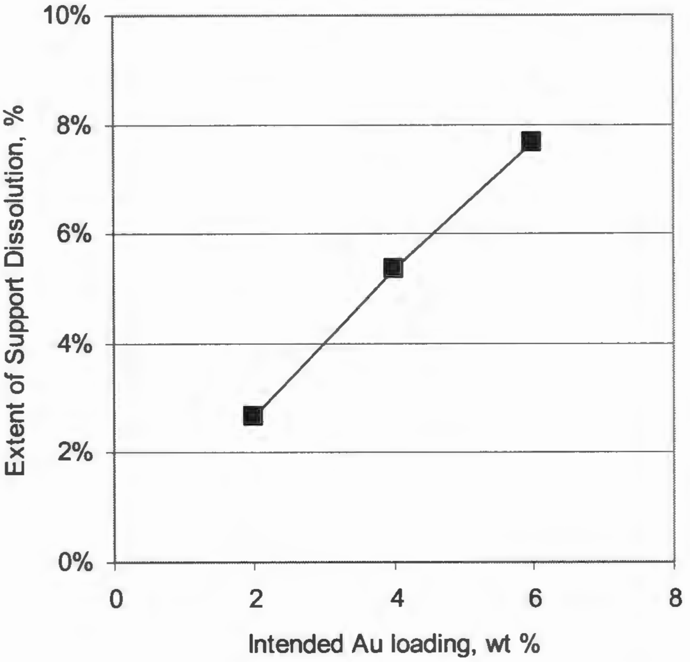

Figure 12.19: Extent of support dissolution as a function of intended loading (MDP2 – Loading Series ~ 30 $m^2.g^{-1}$ ZnO)

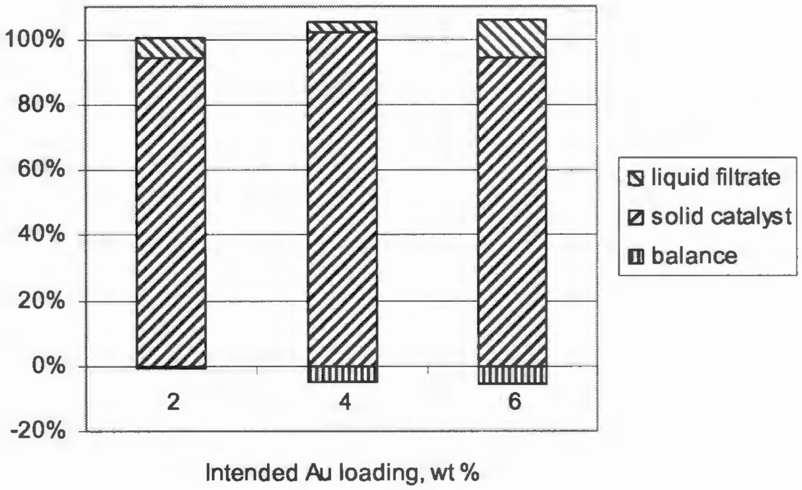

Figure 12.20: Au mass balances (MDP2 – Loading Series ~ 30 $m^2.g^{-1}$ ZnO)

Appendix
Gold Crystallite Size Data

13

13.1 Canonical Deposition-Precipitation Method of Tsubota *et al.* (1995)

13.1.1 DP - pH Series – 3.6 $m^2.g^{-1}$ ZnO

Method: DP
Support: 3.6 $m^2.g^{-1}$ commercial ZnO from SaarChem
Series: pH

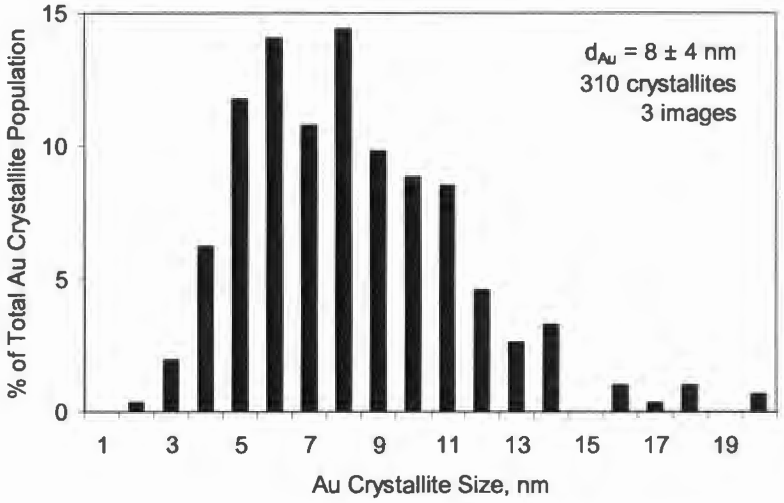

Figure 13.1: Au Crystallite Size Population Distribution
pH 5, 7.8 % Au/ZnO
(DP, 3.6 $m^2.g^{-1}$ ZnO, pH Series)

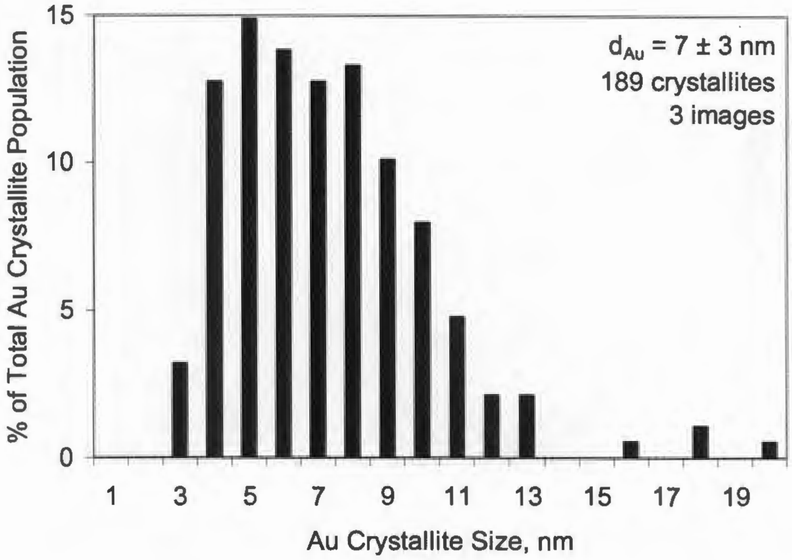

Figure 13.2: Au Crystallite Size Population Distribution
pH 7, 2.9 % Au/ZnO
(DP, 3.6 $m^2.g^{-1}$ ZnO, pH Series)

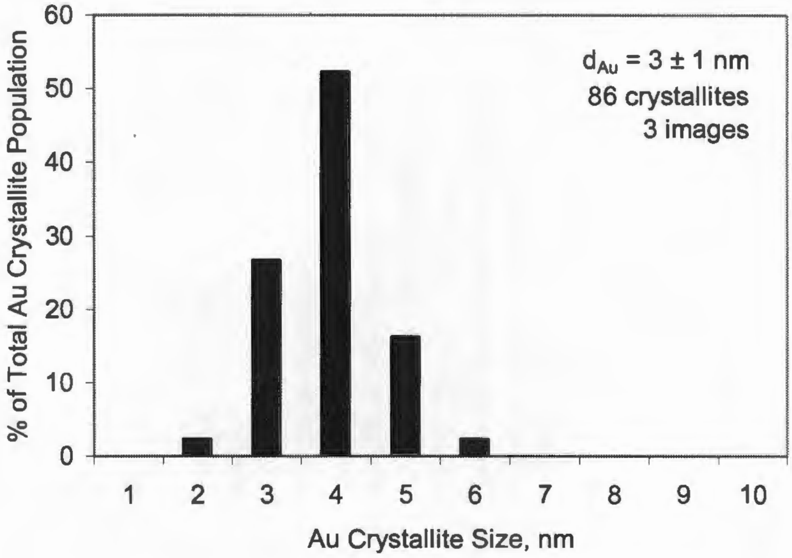

Figure 13.3: Au Crystallite Size Population Distribution
pH 8, 1.5 % Au/ZnO
(DP, 3.6 $m^2.g^{-1}$ ZnO, pH Series)

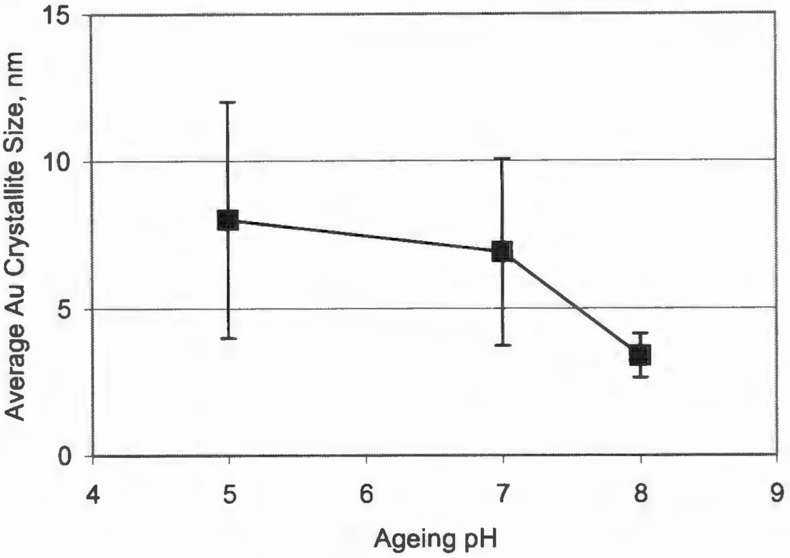

Figure 13.4: Average Au Crystallite Size as a Function of Ageing pH (DP, 3.6 $m^2.g^{-1}$ ZnO, pH Series)

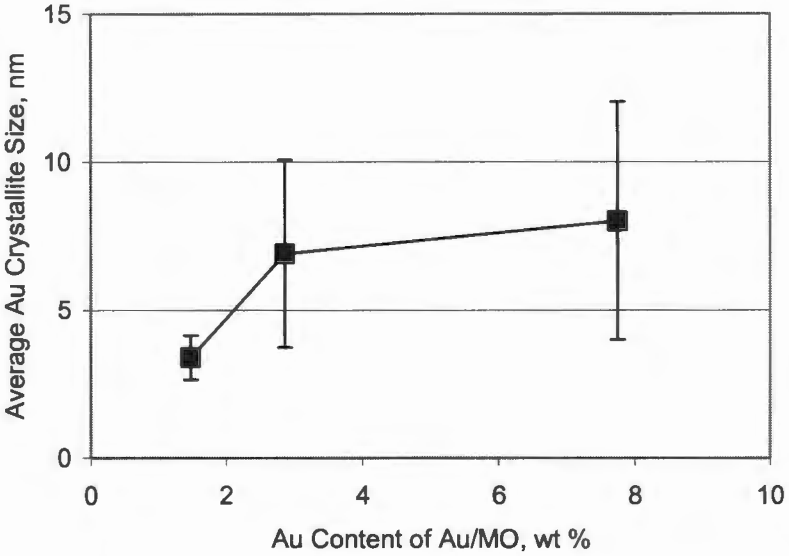

Figure 13.5: Average Au Crystallite Size as a Function of Au Content of Au/ZnO (DP, 3.6 $m^2.g^{-1}$ ZnO, pH Series)

13.2 Modified method of *Fu et al.* (2006)

13.2.1 Constant Ageing pH – MDP1

13.2.1.1 MDP1 - pH Series – 3.6 $m^2.g^{-1}$ ZnO

Method: MDP1

Support: 3.6 $m^2.g^{-1}$ commercial ZnO from SaarChem

Series: pH

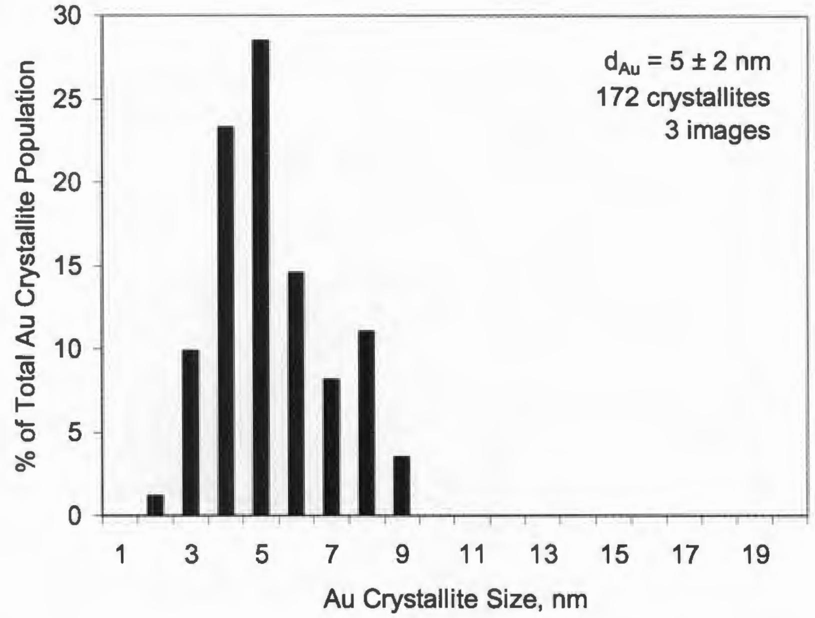

Figure 13.6: Au Crystallite Size Population Distribution
pH 8, 1.2 % Au/ZnO
(MDP1, 3.6 $m^2.g^{-1}$ ZnO, pH Series)

13.2.1.2 MDP1 - Loading Series - 3.6 $m^2.g^{-1}$ ZnO

Method: MDP1

Support: 3.6 $m^2.g^{-1}$ synthetic ZnO from SaarChem

Series: Loading at pH 8

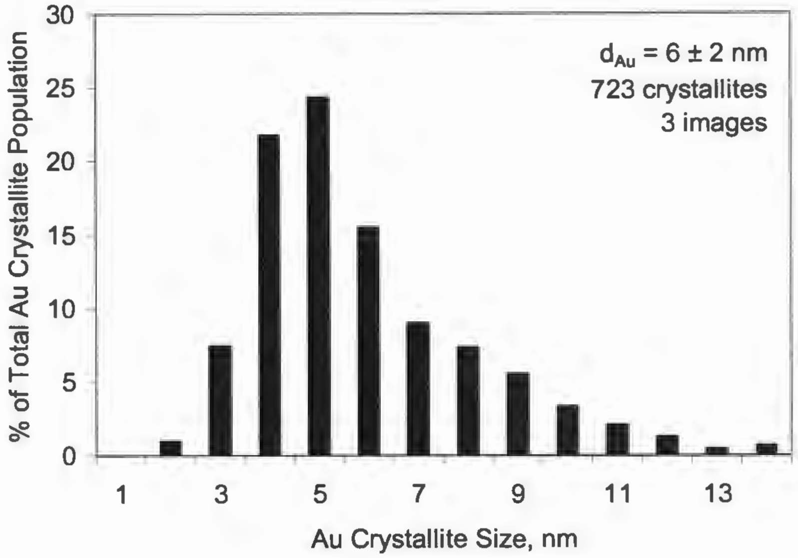

Figure 13.7: Au Crystallite Size Population Distribution
1.2 % Au/ZnO
(MDP1, 3.6 $m^2.g^{-1}$ ZnO, Loading Series)

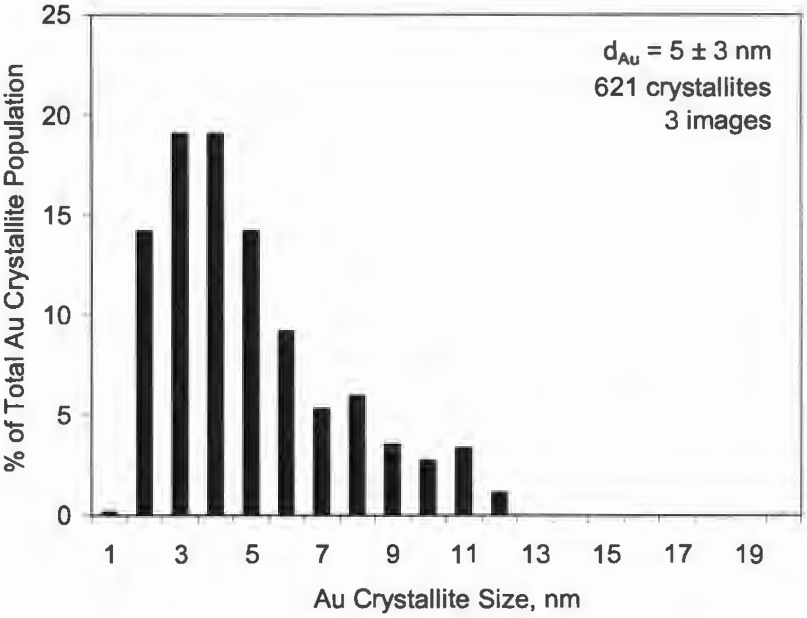

Figure 13.8: Au Crystallite Size Population Distribution
2.1 % Au/ZnO
(MDP1, 3.6 $m^2.g^{-1}$ ZnO, Loading Series)

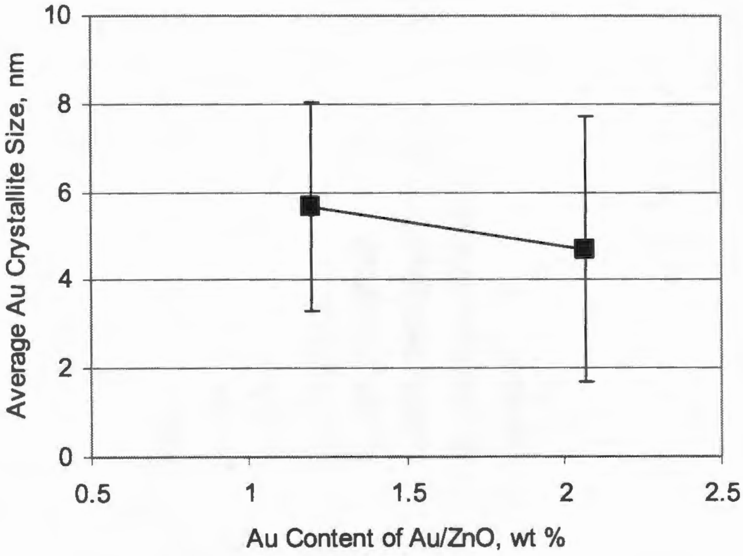

Figure 13.9: Average Au Crystallite Size as a Function of Au Content of Au/ZnO (MDP1, 3.6 $m^2.g^{-1}$ ZnO, Loading Series)

13.2.2 Constant Ageing pH – MDP1

13.2.2.1 MDP2 – Loading series ~ 30 $m^2.g^{-1}$ ZnO

Method: MDP2

Support: ~ 30 $m^2.g^{-1}$ commercial ZnO from SaarChem

Series: Loading at pH 8

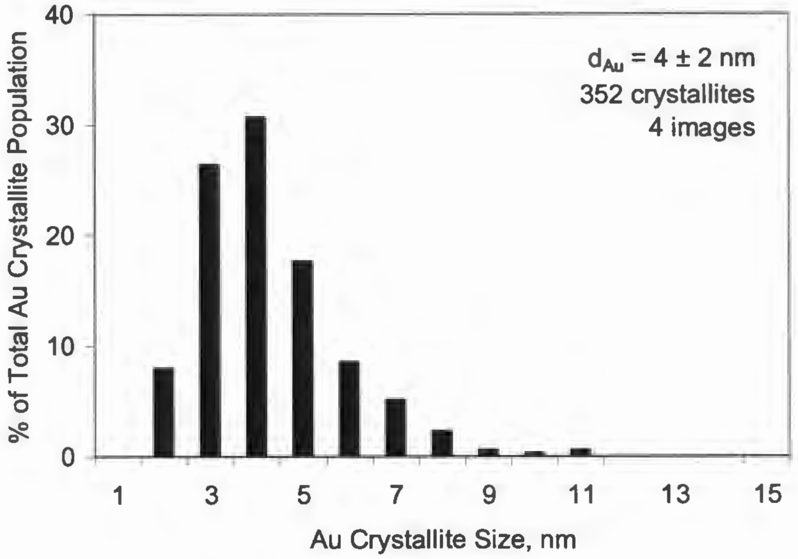

Figure 13.10: Au Crystallite Size Population Distribution
1.9 % Au/ZnO
(MDP2, ~ 30 $m^2.g^{-1}$ ZnO, Loading Series)

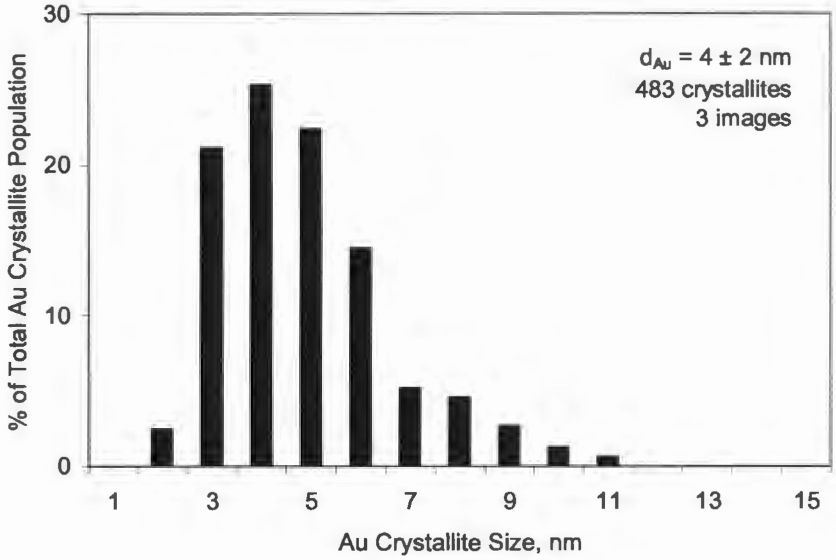

Figure 13.11: Au Crystallite Size Population Distribution
4.0 % Au/ZnO
(MDP2, ~ 30 $m^2.g^{-1}$ ZnO, Loading Series)

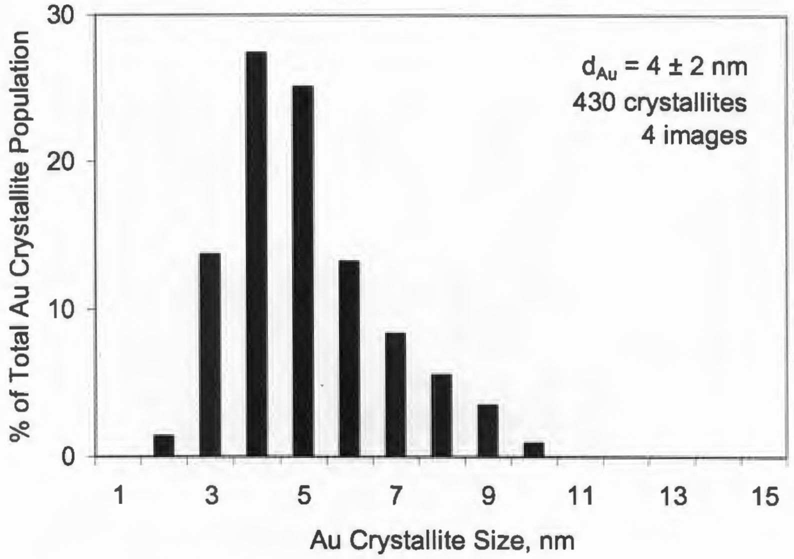

Figure 13.12: Au Crystallite Size Population Distribution
5.7 % Au/ZnO
(MDP2, ~ 30 $m^2.g^{-1}$ ZnO, Loading Series)

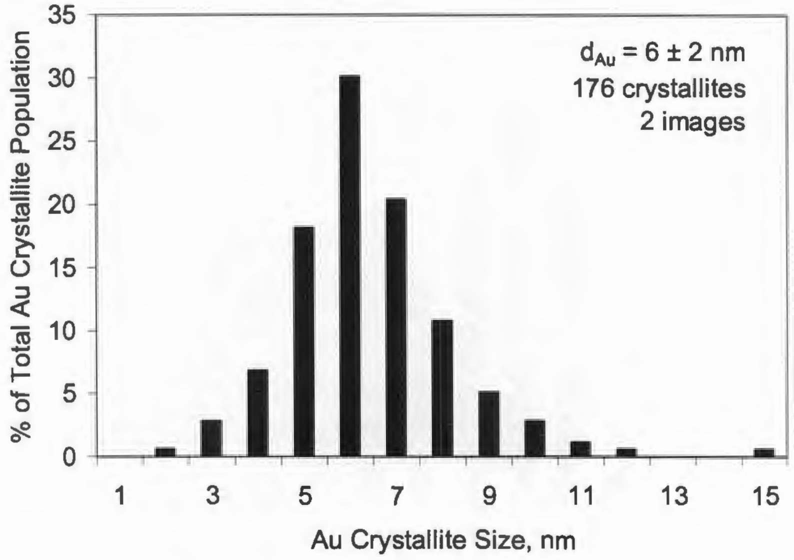

Figure 13.13: Au Crystallite Size Population Distribution
Au/ZnO from $Au(OH)_3/Zn_5(OH)_6(CO_3)_2$
(MDP2, ~ 30 $m^2.g^{-1}$ ZnO, Test Material)

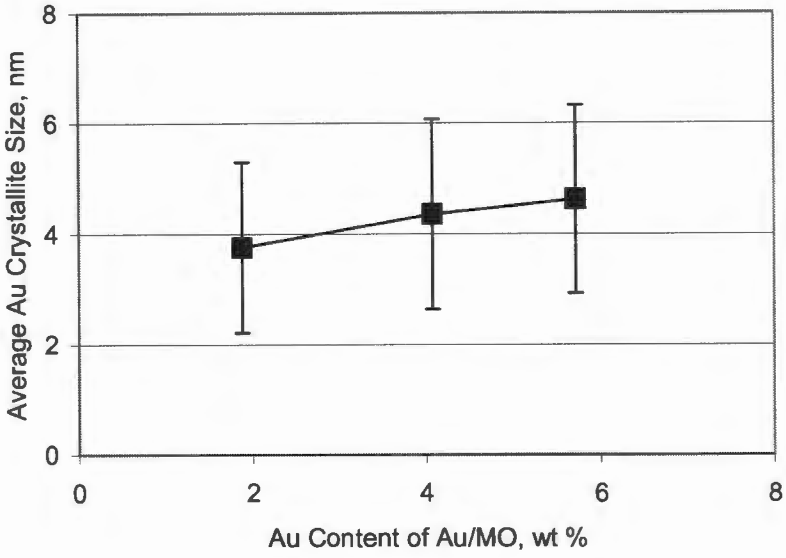

Figure 13.14: Average Au Crystallite Size as a Function of Au Content of Au/MO (MDP2, ~ 30 $m^2.g^{-1}$ ZnO, Loading Series)

13.3 Summarised Gold Crystallite Data

Table 13.1: Summarised gold crystallite size data

Method	Support	Source	Type of Series	pH	[Au] *wt %*	d_{avg} *nm*	σ *nm*	n	No of Images
DP	ZnO	SAARChem	pH	5	7.8	8	4	30	3
				7	2.9	7	3	310	3
				8	1.5	3	1	86	3
MDP1			-	8	1.2	5	2	172	3
			Loading	8	1.2	6	2	723	3
				8	2.1	5	3	621	3
MDP2		Synthetic	Loading	8	1.9	4	2	352	4
				8	4.1	4	2	483	3
				8	5.7	4	2	430	4
		Hydrozincite	-	8	1.7	6	2	176	2

Appendix
Tabulated WGS Activity Data

14

Table 14.1 CO Conversion

Group IB Metal	-		Au		Au		Au		Au		Au		Au		Au	
[Me] (wt %)	0.0		1.3		0.0		1.9		4.1		5.7		1.7		1.5	
Support MO	ZnO		ZnO		ZnO		ZnO		ZnO		ZnO		ZnO		TiO2	
BET SA (m2.g-1)	4		4		44		30		30		33		33		52	
Source	Comm.		Comm.		Comm.		Synth.		Synth.		Synth.		ex HZ		WGC.	
d_{Au} (nm)							3.8		4.4		4.6		5.9		3.8	
TAVG / °C	T / °C	r	T / °C	r	T / °C	r	T / °C	r	T / °C	r	T / °C	r	T / °C	r	T / °C	r
144									150	3.46E-08	150	0.00E+00				
139																
142																
154															155	1.97E-07
162																
173															174	3.00E-07
181																
191			191	4.08E-08											193	4.77E-07
201											200	5.40E-08			202	5.81E-07
211															211	7.35E-07
232															232	1.27E-06
241			241	5.28E-08												
246							246	0.00E+00	246	8.74E-08	246	6.08E-08				
252															252	2.10E-06
274									275	1.37E-07					273	2.61E-06
291			291	7.23E-08												
296									296	1.48E-07	296	9.17E-08			294	3.16E-06
300							300	3.46E-07					300	8.42E-07		
314															314	3.47E-06
325									325	2.01E-07			324	1.29E-06		
341			341	1.20E-07												
346							346	3.87E-07	346	2.67E-07	346	1.36E-07	346	1.72E-06		
350																
371													371	2.31E-06		
375									375	3.77E-07						
388			388	2.10E-07												
396							396	6.30E-07			396	2.81E-07	396	3.14E-06		
400			401	2.07E-07					400	5.03E-07						
417													417	3.71E-06		
433			433	4.61E-07												

Table 14.2 Temperature of 20 % Conversion

Group IB Metal	-		Au		Au		Au		Au		Au		Au		Au		Cu	
[Me] (wt %)	-		1.28		-		1.90		4.10		5.70		1.67		1.51		33.6	
Support MO	ZnO		ZnO		ZnO		ZnO		ZnO		ZnO		ZnO		TiO_2		ZnO/Al_2O_3	
BET SA ($m^2.g^{-1}$)	3.6		3.6		44.3		30		30		33		33		52			
Source	SAARCHem		SAARCHem		Synthetic		Synthetic		Synthetic		Synthetic		ex Hydrozincite		WGC Ref. Material		Sudchemie C18-7	
T_{AVG} / °C	T / °C	X_{CO}	T / °C	X_{CO}	T / °C	X_{CO}	T / °C	XCO	T / °C	XCO	T / °C	X_{CO}	T / °C	X_{CO}	T / °C	X_{CO}	T / °C	X_{CO}
1			401	7%	350	2%	346	11%	375	20%	346	9%			211	16%		
2			433	17%	400	12%	396	18%	400	26%	396	19%			232	28%		
	400	0%	445.2598437	20%			414.1619	20%			398.960751	20%	324	20%	217.6045	20%	142	20%
SLOPE	-		0.002846174		0.001819		0.001355		0.0025994		0.00201186							
INT	-		-1.067287044		-0.61251		-0.36104		-0.7791295		-0.6026528							
400	400		400		400		400		400		400							
X@T=200C	0%		7%		12%		18%		26%		20%							
(mol CO).s-1	0		1.99E-07		3.21E-07		5.05E-07		7.27E-07		5.64E-07							
(mol CO).m-2.s-1	0		5.52E-08		7.25E-09		1.68E-08		2.42E-08		1.71E-08							
mAu (g)			1.28E-02				1.90E-02		4.10E-02		5.70E-02							
n Au (mol)			6.51E-05				9.66E-05		2.08E-04		2.90E-04							
(mol CO).(mol Au)-1.s-1			3.05E-03				5.22E-03		3.49E-03		1.95E-03							

Table 14.3 Reaction rate i.t.o (mol CO).(g Catalyst)$^{-1}$.s^{-1}

Group IB Metal [Me] (wt %) Support MO BET SA (m2.g-1) Source	- - ZnO 4 Comm.		Au 1 ZnO 4 Comm.		Au - ZnO 44 Comm.		Au 2 ZnO 30 Synth.		Au 4 ZnO 30 Synth.		Au 6 ZnO 33 Synth.		Au 2 ZnO 33 ex HZ		Au 2 TiO2 52 WGC. Reference		Cu 34 ZnO/Al2O3 0 C18-7	
TAVG / °C	T / °C	r	T / °C	r	T / °C	r	T / °C	r	T / °C	r	T / °C	r	T / °C	r	T / °C	r	T / °C	r
144									150	5.00E-08	150	0.00E+00					133	2.13E-07
139																	139	4.28E-07
142																	142	5.61E-07
154															155	1.21E-07	153	9.29E-07
162																	162	1.43E-06
173															174	1.85E-07	172	1.91E-06
181																	181	2.04E-06
191			191	4.08E-08											193	2.95E-07	190	2.31E-06
201											200	1.04E-07			202	3.59E-07		
211															211	4.54E-07		
232															232	7.85E-07		
241			241	5.28E-08														
246							246	0.00E+00	246	1.27E-07	246	1.17E-07						
252															252	1.29E-06		
274									275	1.98E-07					273	1.61E-06		
291			291	7.23E-08														
296									296	2.14E-07	296	1.76E-07			294	1.95E-06		
300							300	2.69E-07					300	3.70E-07				
314															314	2.14E-06		
325									325	2.91E-07			324	5.67E-07				
341			341	1.20E-07														
346							346	3.00E-07	346	3.87E-07	346	2.61E-07	346	7.58E-07				
350					350	6.75E-08												
371													371	1.02E-06				
375									375	5.46E-07								
388			388	2.10E-07														
396							396	4.89E-07			396	5.41E-07	396	1.38E-06				
400	400	0.00E+00	401	2.07E-07	400	3.21E-07			400	7.27E-07								
417													417	1.63E-06				
433			433	4.61E-07														

Table 14.4 Reaction rate i.t.o (mol CO).(m^2 Catalyst BET surface area)$^{-1}$.s^{-1}

Group IB Metal [Me] (wt %) Support MO BET SA (m2.g-1) Source	- - ZnO 4 Comm.		Au 1 ZnO 4 Comm.		Au - ZnO 44 Comm.		Au 2 ZnO 30 Synth.		Au 4 ZnO 30 Synth.		Au 6 ZnO 33 Synth.		Au 2 ZnO 33 ex HZ		Au 2 TiO2 52 WGC. Reference		Cu 34 ZnO/Al2O3 not measured C18-7	
TAVG / °C	T / °C	r	T / °C	r	T / °C	r	T / °C	r	T / °C	r	T / °C	r	T / °C	r	T / °C	r	T / °C	r
144									150	1.67E-09	150	0.00E+00					133	na
139																	139	na
142																	142	na
154															155	2.34E-09	153	na
162																	162	na
173															174	3.56E-09	172	na
181																	181	na
191			191	1.13E-08											193	5.66E-09	190	na
201											200	3.15E-09			202	6.89E-09		
211															211	8.73E-09		
232															232	1.51E-08		
241			241	1.47E-08														
246							246	0.00E+00	246	4.22E-09	246	3.54E-09						
252															252	2.49E-08		
274									275	6.59E-09					273	3.09E-08		
291			291	2.01E-08														
296									296	7.14E-09	296	5.35E-09			294	3.75E-08		
300							300	8.96E-09					300	1.12E-08				
314															314	4.12E-08		
325									325	9.72E-09			324	1.72E-08				
341			341	3.34E-08														
346							346	1.00E-08	346	1.29E-08	346	7.90E-09	346	2.30E-08				
350					350	1.52E-09												
371													371	3.08E-08				
375									375	1.82E-08								
388			388	5.84E-08														
396							396	1.63E-08			396	1.64E-08	396	4.18E-08				
400	400	0.00E+00	401	5.74E-08	400	7.25E-09			400	2.42E-08								
417													417	4.95E-08				
433			433	1.28E-07														

Table 14.5 Reaction rate i.t.o (mol CO).(g Au)$^{-1}$.s^{-1}

Group IB Metal	-		Au		Au		Au		Au		Au		Au		Au	
[Me] (wt %)	-		1		-		2		4		6		2		2	
Support MO	ZnO		ZnO		ZnO		ZnO		ZnO		ZnO		ZnO		TiO2	
BET SA (m2.g-1)	4		4		44		30		30		33		33		52	
Source	Comm.		Comm.		Comm.		Synth.		Synth.		Synth.		ex HZ		WGC. Reference	
TAVG / °C	T / °C	r	T / °C	r	T / °C	r	T / °C	r	T / °C	r	T / °C	r	T / °C	r	T / °C	r
144									150	1.22E-06	150	0.00E+00				
139																
142																
154															155	8.04E-06
162																
173															174	1.23E-05
181																
191			191	3.19E-06											193	1.95E-05
201											200	1.82E-06			202	2.37E-05
211															211	3.01E-05
232															232	5.20E-05
241			241	4.13E-06												
246							246	0.00E+00	246	3.09E-06	246	2.05E-06				
252															252	8.57E-05
274									275	4.82E-06					273	1.07E-04
291			291	5.65E-06												
296									296	5.22E-06	296	3.10E-06			294	1.29E-04
300							300	1.41E-05					300	2.22E-05		
314															314	1.42E-04
325									325	7.11E-06			324	3.40E-05		
341			341	9.39E-06												
346							346	1.58E-05	346	9.43E-06	346	4.57E-06	346	4.54E-05		
350					350	0.00E+00										
371													371	6.09E-05		
375									375	1.33E-05						
388			388	1.64E-05												
396							396	2.58E-05			396	9.50E-06	396	8.27E-05		
400	400	0.00E+00	401	1.61E-05	400	0.00E+00			400	1.77E-05						
417													417	9.77E-05		
433			433	3.60E-05												

Table 14.6 Reaction rate i.t.o (mol CO).(mol Au)$^{-1}$.s^{-1}

Group IB Metal [Me] (wt %) Support MO BET SA (m2.g-1) Source	- 0 ZnO 4 Comm.		Au 1 ZnO 4 Comm.		- 0 ZnO 44 Comm.		Au 2 ZnO 30 Synth.		Au 4 ZnO 30 Synth.		Au 6 ZnO 33 Synth.		Au 2 ZnO 33 ex HZ		Au 2 TiO2 52 WGC. Reference		Cu 34 ZnO/Al2O3 0 C18-7	
TAVG / °C	T / °C	r	T / °C	r	T / °C	r	T / °C	r	T / °C	r	T / °C	r	T / °C	r	T / °C	r	T / °C	r
144									150	2.40E-04	150	0.00E+00					133	4.02E-05
139																	139	8.10E-05
142																	142	1.06E-04
154															155	1.58E-03	153	1.76E-04
162																	162	2.71E-04
173															174	2.41E-03	172	3.62E-04
181																	181	3.86E-04
191			191	6.26E-04											193	3.84E-03	190	4.38E-04
201											200	3.59E-04			202	4.67E-03		
211															211	5.91E-03		
232															232	1.02E-02		
241			241	8.12E-04														
246							246	0.00E+00	246	6.07E-04	246	4.03E-04						
252															252	1.68E-02		
274									275	9.49E-04					273	2.10E-02		
291			291	1.11E-03														
296									296	1.03E-03	296	6.09E-04			294	2.54E-02		
300							300	2.78E-03					300	4.36E-03				
314															314	2.79E-02		
325									325	1.40E-03			324	6.68E-03				
341			341	1.85E-03														
346							346	3.11E-03	346	1.85E-03	346	9.00E-04	346	8.93E-03				
350					350	0.00E+00												
371													371	1.20E-02				
375									375	2.62E-03								
388			388	3.23E-03														
396							396	5.07E-03			396	1.87E-03	396	1.63E-02				
400	400	0.00E+00	401	3.17E-03	400	0.00E+00			400	3.49E-03								
417													417	1.92E-02				
433			433	7.08E-03														

Table 14.7 Reaction rate i.t.o (mol CO).(m^2 exposed Au surface area)$^{-1}$.s^{-1}

Group IB Metal	-		Au		Au		Au		Au		Au		Au		Au	
[Me] (wt %)	0.0		1.3		0.0		1.9		4.1		5.7		1.7		1.5	
Support MO	ZnO		ZnO		ZnO		ZnO		ZnO		ZnO		ZnO		TiO2	
BET SA (m2.g-1)	4		4		44		30		30		33		33		52	
Source	Comm.		Comm.		Comm.		Synth.		Synth.		Synth.		ex HZ		WGC.	
d_{Au} (nm)							3.8		4.4		4.6		5.9		3.8	
TAVG	T	r	T	r	T	r	T	r	T	r	T	r	T	r	T	r
/°C	/°C		/°C		/°C		/°C		/°C		/°C		/°C		/°C	
144									150	1.73E-08	150	0.00E+00				
139																
142																
154															155	9.84E-08
162																
173															174	1.50E-07
181																
191			191	2.04E-08											193	2.39E-07
201											200	2.70E-08			202	2.91E-07
211															211	3.68E-07
232															232	6.36E-07
241			241	2.64E-08												
246							246	0.00E+00	246	4.37E-08	246	3.04E-08				
252															252	1.05E-06
274									275	6.83E-08					273	1.30E-06
291			291	3.62E-08												
296									296	7.40E-08	296	4.59E-08			294	1.58E-06
300							300	1.73E-07					300	4.21E-07		
314															314	1.73E-06
325									325	1.01E-07			324	6.45E-07		
341			341	6.01E-08												
346							346	1.93E-07	346	1.34E-07	346	6.78E-08	346	8.62E-07		
350																
371													371	1.16E-06		
375									375	1.89E-07						
388			388	1.05E-07												
396							396	3.15E-07			396	1.41E-07	396	1.57E-06		
400			401	1.03E-07					400	2.51E-07						
417													417	1.86E-06		
433			433	2.30E-07												